

Characterization of Surface and Interface Nanostructures by means of Specular and Diffuse X-ray Scattering

vorgelegt von
Diplom-Physiker
Anton Haase
geboren in Berlin

Von der Fakultät II - Mathematik und Naturwissenschaften
der Technischen Universität Berlin
zur Erlangung des akademischen Grades
Doktor der Naturwissenschaften
Dr. rer. nat.

genehmigte Dissertation

Promotionsausschuss:

Vorsitzender: Prof. Dr. Mister Unbekannt
Gutachter: Prof. Dr. Stefan Eisebitt
Gutachter: Prof. Dr. Mathias Richter
Gutachterin: Dr. Saša Bajt

Tag der wissenschaftlichen Aussprache:

Berlin 2017

Abstract

English

Zusammenfassung

Deutsch

Contents

1 Theoretical Description of EUV and X-ray Scattering	1
1.1 EUV and X-ray Radiation	1
1.2 Interaction of EUV and X-ray Radiation With Matter	2
1.2.1 Elastic Scattering	5
1.2.2 Absorption and Fluorescence	7
1.3 Specular Reflection from Surfaces and Interfaces in Layered Systems	8
1.4 Diffuse Scattering in Layered Systems	11
1.5 Grazing-incidence X-ray Fluorescence	18
2 Experimental Setup and Sample Systems	23
2.1 Synchrotron Radiation	23
2.2 The Instrumentation for the EUV Spectral Range	27
2.2.1 The EUV Beamlines at BESSYII and MLS	27
2.2.2 The Experimental Endstations at the EUVR and SX700 Beamlines	29
2.3 Grazing-incidence X-ray Fluorescence at the FCM Beamline	32
2.4 Sample systems	33
2.4.1 Choice of the Chemical Species and Multilayer Design	34
2.4.2 Multilayer Deposition by Magnetron Sputtering	35
3 Characterization of the Multilayer Structure for Different Systems	37
3.1 Reconstruction Based on Specular EUV reflectance	38
3.1.1 Multilayer Model and Particle Swarm Optimization	39
3.1.2 The Problem of Model Uniqueness and Maximum Likelihood Estimation	43
3.2 Molybdenum Thickness Variation in Mo/Si/C Multilayers	47
3.2.1 Sample systems and experimental procedure	47
3.2.2 Combined Analysis of X-ray and EUV reflectance	50
3.2.3 Optimization results	54
3.3 Analysis of Cr/Sc Multilayers with Sub-nanometer Layer Thickness	56
3.3.1 Reconstruction with a discrete layer model approach	57

Contents

3.3.2	Extending The Model to Graded Interfaces and Interdiffusion	61
3.3.3	Addition of Complementary Experimental Methods	65
3.3.4	Reconstruction and Maximum Likelihood Evaluation	68
References	75	

List of Figures

1.1	Illustration of <i>X-ray fluorescence</i> for an atom.	7
1.2	Illustration of <i>Snell's law</i> .	8
1.3	Field amplitudes in the exact solution for a multilayer system.	10
1.4	Scattering geometry and definition of the scattering vector.	11
1.5	Illustration of the four scattering processes of the DWBA.	15
1.6	Calculation scheme for the x-ray fluorescence	20
1.7	X-ray standing wave fluorescence principle.	21
2.1	Theoretical synchrotron radiation radiant power spectra	24
2.2	Schematic overview of BESSY II.	25
2.3	Schematic overview of the MLS	26
2.4	Radiant power of the SX700 beamline.	27
2.5	Schematic setup of the SX700 beamline.	28
2.6	Schematic optics of the SX700 and EUVR beamlines.	30
2.7	The BigRef.	31
2.8	The EUV ellipso-scatterometer.	31
2.9	FCM beamline scheme.	32
2.10	The GIXRF chamber.	33
2.11	Refractive indices of Cr and Sc in the water window.	34
2.12	Refractive indices of Mo and Si in the wavelength range from 12.4 nm to 14.0 nm.	35
2.13	Schematic setup for magnetron sputtering.	36
2.14	Mo/Si multilayer sample.	36
3.1	Spectrally resolved reflectance data of the Mo/B ₄ C/Si/C multilayer sample. The irradiation was conducted under a fixed angle of incidence $\alpha_i = 15.0^\circ$. The measurement uncertainty is within the line thickness of the plot.	38
3.2	Model of the multilayer stack including the substrate and the capping layers. The periodic part is enclosed between the dashed lines with four layers in each period repeated $N = 64$ times. The capping period does not include an interdiffusion layer but has a natural SiO ₂ layer.	40
3.3	Theoretical reflectance curve based on the optimal model parameters obtained from the particle swarm optimization.	42
3.4	Parameter influence.	43

List of Figures

3.5 Results of the maximum likelihood estimation obtained via the Markov-chain Monte Carlo (MCMC) procedure. a) Two dimensional projection of the likelihood distribution for the parameter pair d_{Si} and d_{Mo} . The projection was obtained by marginalizing over all other parameters of the model. The black contours indicate the areas for one and two standard deviations (one and two sigma contours). The blue lines in all three sub-figures indicate the best parameter set found with the particle swarm optimization (PSO) method. b) One dimensional projection of the likelihood distribution for the silicon layer thickness d_{Si} . The solid black line marks the center position (50% percentile) of the distribution. The dotted lines are the limits of one standard deviation. c) The one dimensional distribution similarly to b) for the molybdenum layer thickness.	45
3.6 In analogy to Fig. 3.5b and 3.5c the one dimensional projections of the likelihood distribution estimation for the Mo/B ₄ C/Si/C sample are shown for the remaining parameters of the model with the PSO result, the center value and one standard deviation.	46
3.7 a) Reflectivity curves for the unpolished samples across the wavelength at a fixed angle of incidence of $\alpha_i = 15^\circ$ from the surface normal. The nine samples differ by the nominal Mo layer thickness indicated at the bottom axis. b) Reflectivity curves of the ten polished samples measured under the same conditions as for the first sample set.	48
3.8 X-ray reflectivity (XRR) data for all unpolished and polished samples shown in dependence on the nominal molybdenum layer thickness $d_{\text{Mo}}^{\text{nom}}$. In each of the subfigures a) and b) the XRR measurements for the sample with smallest and largest $d_{\text{Mo}}^{\text{nom}}$ are shown on the bottom and the top of the subfigure, respectively. In between, the XRR curves are illustrated in as a color map plot.	49
3.9 Model of the multilayer stack including the substrate and the capping layers. The periodic part is enclosed between the dashed lines with four layers in each period repeated 49 times. The capping period does not include an interdiffusion layer but has a natural SiO ₂ layer and a carbon-like layer accounting for contamination on the top surface.	50
3.10 Combined analysis	52
3.11 Two-dimensional likelihood distribution indicating the correlation of silicon and carbon layer thickness. The distribution was obtained by marginalizing over all remaining parameters of the model. The blue lines indicate the fit obtained through the two-step MCMC optimization procedure (see main text).	53
3.12 Experimental data in comparison with the theoretical curves calculated with the model parameters obtained from the combined analysis of extreme ultraviolet (EUV) and XRR data. The data shown here was measured on the unpolished sample with nominal molybdenum thickness of $d_{\text{Mo}}^{\text{nom}} = 3.05 \text{ nm}$.54	

3.13 a) Fitted Mo thickness values for both sample sets resulting from the MCMC analysis (see text). The nominal Mo layer thickness is shown in comparison in good agreement with the obtained thicknesses. b) Fitted total period thickness D for both sample sets. For both sample sets, clear jumps can be observed at approx. $d_{\text{Mo}}^{\text{nom}} = 2.00 \text{ nm}$ and $d_{\text{Mo}}^{\text{nom}} = 2.38 \text{ nm}$, respectively, which is attributed to the crystallization threshold (see text). The marked (circle) samples were measured and analyzed with respect to the diffuse scattering.	55
3.14 Peak reflectance values for each sample obtained from the EUV measurements for the unpolished sample set (a) and the polished sample set (b). The maximum theoretical reflectance is shown in both subfigures for a perfect (no roughness or interdiffusion) layer system with the same specifications as the samples.	56
3.15 Model of the multilayer stack including the substrate and the capping layers. The periodic part is enclosed between the dashed lines with four layers in each period repeated $N = 64$ times. The capping period does not include an interdiffusion layer but has a natural SiO_2 layer.	57
3.16 EUV and XRR	58
3.17 Fitted experimental EUV reflectance curves across the wavelength of the radiation impinging at $\alpha_i = 1.5^\circ$ from normal, based on the binary model. The green curve shows the maximum possible reflectance assuming a perfect multilayer system without roughness or interdiffusion.	60
3.18 a) Measured EUV reflectivity curve for and near-normal angle of incidence of $\alpha_i = 1.5^\circ$ together with calculated curve of the PSO-based binary model reconstruction. b) Measured and calculated XRR curves for the same sample and model parameters at grazing angles of incidence using radiation at the Cu-K_α wavelength. A clear mismatch of the theoretical curve and the measured data can be observed for the second Bragg peak between $\alpha_i^{\text{GI}} = 5.0^\circ$ and $\alpha_i^{\text{GI}} = 6.0^\circ$	60
3.19 Binary and gradual Cr/Sc multilayer models.	62
3.20 Numerical uncertainty	63
3.21 Comparison of the reconstructions of both models for the EUV and XRR data. a) Measured EUV reflectivity curve for and near-normal angle of incidence of $\alpha_i = 1.5^\circ$ together with calculated curve of the PSO-based binary model reconstruction. b) Measured and calculated XRR curves for the same sample and model parameters at grazing angles of incidence using radiation at the Cu-K_α wavelength. A clear mismatch of the theoretical curve and the measured data can be observed for the second Bragg peak between $\alpha_i^{\text{GI}} = 5.0^\circ$ and $\alpha_i^{\text{GI}} = 6.0^\circ$. c) Measured EUV reflectivity curve for and near-normal angle of incidence of $\alpha_i = 1.5^\circ$ together with calculated curve of the PSO-based gradual model reconstruction. d) Measured and calculated XRR curves for the same sample and model parameters at grazing angles of incidence using radiation at the Cu-K_α wavelength.	64
3.22 REUV	66
3.23 XRF	67
3.24 All relevant data	68
3.25 Measured and calculated reflectance and intensity curves for the optimized parameters with the combined analysis of all experiments as listed in Table ??.	69

List of Figures

3.26 Cornerplot	71
3.27 Visual representation of the total confidence intervals for each of the parameters with respect to each of the individual experiments as well as the combined analysis.	72
3.28 Real part of the index of refraction n based on the results of the optimized parameters listed in Table 3.11 for the combined analysis for a selected wavelength. The gradual interface model is shown in direct comparison to the binary model optimized for the EUV reflectance curve over three full periods. The resulting strong asymmetry in the width of the interface regions is clearly visible (see text). The gray and white shaded areas indicate the Cr and Sc layers, respectively, for the binary model.	73
3.29 CrSc eta rho correlation	74

List of Tables

2.1	Beamline parameters of the two EUV beamlines extreme ultraviolet beamline (EUVR) and sx700 in comparison.	29
3.1	Multilayer parametrization and parameter limits	40
3.2	Results for the ptimized parameters based on the PSO of the EUV reflectivity for the Mo/B ₄ C/Si/C sample.	42
3.3	MCMC results obtained by the analysis of the EUV reflectivity for the Mo/B ₄ C/Si/C sample. The center values (50% percentile) together with confidence intervals (c.i.) of one and two standard deviations are shown.	46
3.4	List of nominal molybdenum layer thicknesses in the two sample sets. Both sets were fabricated with a equidistant increase in thickness from 1.70 nm to 3.05 nm with 9 unpolished and 10 polished samples.	47
3.5	Parametrization of the Mo/Si/C multilayer samples with varying molybdenum layer thicknesses.	51
3.6	List of nominal molybdenum layer thicknesses in the two sample sets. Both sets were fabricated with a equidistant increase in thickness from 1.70 nm to 3.05 nm with 9 unpolished and 10 polished samples.	54
3.7	Parametrization of the Cr/Sc binary multilayer model.	58
3.8	PSO fit results for the discrete layer Cr/Sc multilayer model. The bulk multilayer parameters were obtained by exclusively applying the PSO method to the EUV data. The capping layer parameters were deducted from the XRR data excluding the Bragg peaks in a combined analysis. . .	59
3.9	Multilayer parametrization and parameter limits	63
3.10	Optimized model parameters obtained by PSO analysis	69
3.11	Optimized model parameters with confidence intervals derived from MCMC validation for each individual experiment and the combined analysis	70

Abbreviations

BESSY II electron storage ring for synchrotron radiation.

CCD charge coupled device.

DWBA distorted-wave Born approximation.

EUV extreme ultraviolet.

EUVR extreme ultraviolet beamline.

FCM four crystal monochromator.

FEL free-electron laser.

GIXRF grazing incidence X-ray fluorescence.

HZB Helmholtz-Zentrum Berlin.

LINAC linear accelerator.

MCMC Markov-chain Monte Carlo.

MLS metrology light source.

PSD power spectral density.

PSO particle swarm optimization.

PTB Physikalisch-Technische Bundesanstalt.

r.m.s. root mean square.

REUV resonant extreme ultraviolet reflectivity.

SASE self-amplified spontaneous emission.

SSD silicon drift detector.

SX700 soft x-ray beamline.

Abbreviations

TXRF total reflection x-ray fluorescence.

XRF X-ray fluorescence.

XRR X-ray reflectivity.

XSW X-ray standing wave.

Symbols

α_f	scattering angle defined from the surface normal.
α_i	angle of incidence defined from the surface normal.
c	speed of light in vacuum $c = 1/\sqrt{\epsilon_0 \mu_0}$.
e	elementary charge.
$\epsilon(\omega)$	dielectric function $\epsilon(\omega) = \epsilon_1(\omega) + i\epsilon_2(\omega)$.
ϵ_0	vacuum permittivity or electric constant.
h	Planck's constant, $h = 4.135667662(25) \times 10^{-15}$ eV s.
\vec{k}	wave vector; the wave number is $ \vec{k} = k_0 = 2\pi/\lambda$.
k_0	modulus of the wave vector in vacuum (wave number) $k_0 = \omega/c = 2\pi/\lambda$.
λ	wavelength.
m_0	electron rest mass.
μ_0	vacuum permeability or magnetic constant.
n	complex index of refraction, $n = \delta + i\beta$.
ω	frequency.
\vec{q}	scattering vector / reciprocal space vector, $\vec{q} = (q_x, q_y, q_z)^T$.
r_e	classical electron radius $r_e = e^2/4\pi\epsilon_0 mc^2 = 2.82 \times 10^{-5}$.
$\rho_e(\vec{r})$	electron density at position \vec{r} .
$\frac{d\sigma}{d\Omega}$	differential scattering cross section.
θ_f	azimuthal scattering angle (out-of-plane scattering angle).

1

Theoretical Description of EUV and X-ray Scattering

This chapter summarizes the aspects of the interactions of electromagnetic radiation with matter, relevant for this investigation. Since this thesis specifically covers the interaction of EUV and X-ray radiation with multilayer systems, in particular the basic principles of specular reflection and transmission through a stack of layers are given. Then, the diffuse scattering theory for multilayer systems is derived based on the well established distorted-wave Born approximation (DWBA). Finally, the generation of fluorescence radiation and its exploitation for the analysis of multilayer compositions is described.

1.1 EUV and X-ray Radiation

EUV and x-ray radiation is electromagnetic radiation, which only differs by its wavelength. The different names for these parts of the electromagnetic spectrum are mostly of historic origin. However, differences in energy and, thus, reflectance, transmission and absorption properties in matter still justify this differentiation today from a technical perspective. For the sake of consistency within this thesis and the lack of a unique definition of the terms used in literature, we shall define EUV radiation as electromagnetic radiation within the spectral range from 1 nm to 100 nm vacuum wavelength (corresponding to photon energies of approximately 12.4 eV to 1240 eV). Consequently, the radiation with the wavelengths below 1.0 nm (photon energies above 1.24 keV) shall be called x-rays. In both cases the theoretical description is identical and is thus presented here independent of this naming convention.

The entirety of electrostatic fields and electromagnetic radiation is described by Maxwell's equations. In vacuum they are defined as

$$\begin{aligned}\nabla \cdot \vec{E} &= 0, & \nabla \cdot \vec{B} &= 0, \\ \nabla \times \vec{E} &= -\frac{\partial \vec{B}}{\partial t}, & \nabla \times \vec{B} &= \mu_0 \epsilon_0 \frac{\partial \vec{E}}{\partial t},\end{aligned}$$

with the electric constant ϵ_0 and the magnetic constant μ_0 and the electric field \vec{E} and the magnetic field \vec{B} . By taking the curl of these equations and using the identity $\nabla \times (\nabla \times \vec{X}) = \nabla(\nabla \cdot \vec{X}) - \Delta \vec{X}$ and the Laplacian $\Delta = \nabla^2$ for an arbitrary vector field \vec{X} the Maxwell equations yield

$$\Delta \vec{E} - \frac{1}{c^2} \frac{\partial^2 \vec{E}}{\partial t^2} = 0, \quad \Delta \vec{B} - \frac{1}{c^2} \frac{\partial^2 \vec{B}}{\partial t^2} = 0, \quad (1.1)$$

with $c = 1/\sqrt{\mu_0 \epsilon_0}$, the speed of light in vacuum.

All scattering processes and charge densities in this thesis are considered to be time-independent. The wave equations Eq. (1.1) can thus be further simplified by separating the explicit time dependence of the fields as

$$\vec{E}(\vec{r}, t) = \vec{E}(\vec{r}) e^{i\omega t}, \quad \vec{B}(\vec{r}, t) = \vec{B}(\vec{r}) e^{i\omega t}, \quad (1.2)$$

where \vec{r} is a vector to a point in space. The time-independent wave equations then read

$$(\Delta + k_0^2) \vec{E} = 0, \quad (\Delta + k_0^2) \vec{B} = 0, \quad (1.3)$$

where $k_0 = \omega/c = 2\pi/\lambda$, i.e. the absolute value of the vacuum wave vector. A very important and often applied solution to this wave equation is the monochromatic plane wave. Hence, for Eq. (1.3) we obtain

$$E(\vec{r}, t) = E_0 e^{i\omega t - i\vec{k} \cdot \vec{r}}, \quad B(\vec{r}, t) = B_0 e^{i\omega t - i\vec{k} \cdot \vec{r}}, \quad (1.4)$$

where E_0 and B_0 are the initial electric and magnetic field amplitudes, respectively, and $|\vec{k}| = k_0$ [15].

1.2 Interaction of EUV and X-ray Radiation With Matter

The wave equations Eq. (1.3) still hold for the propagation of radiation inside an isotropic*, homogeneous medium in slightly modified form. The Maxwell equations contain the electric permittivity and magnetic permeability, which are different for electric and magnetic fields inside a medium compared to the respective quantities in vacuum (electric and magnetic constants). The equations inside a medium are therefore obtained by replacing $\epsilon_0 \rightarrow \epsilon = \epsilon_r \epsilon_0$ and $\mu_0 \rightarrow \mu = \mu_r \mu_0$,

$$\nabla \times \vec{E} = - \frac{\partial \vec{B}}{\partial t}, \quad \nabla \times \vec{B} = \mu_r \mu_0 \epsilon_r \epsilon_0 \frac{\partial \vec{E}}{\partial t}, \quad (1.5)$$

where ϵ_r is the relative electric permittivity and μ_r is the relative magnetic permeability. These quantities are defined through the electric displacement field $\vec{D} = \epsilon \vec{E}$, which remains unchanged at the interface of vacuum and matter, and the magnetic field relation $\vec{B} = \mu \vec{H}$ (for para- and diamagnetic materials with a magnetization parallel to the field lines). In case of electromagnetic waves in the EUV and x-ray spectral range, the latter does not differ significantly from one and is often approximated by $\mu_r \approx 1$ [8]. The electric permittivity, however, can take significantly different values inside matter than in vacuum. An electric field entering a medium causes a polarization field \vec{P} of that matter depending on the respective polarizability. The displacement field is given as $\vec{D} = \vec{E} + \vec{P}$

* The general case including anisotropic materials can also be described with the wave equation. In that case the scalar coefficients for isotropic materials become tensors.

and remains constant at the interface as mentioned above. Hence, the relative electric permittivity is directly related to the susceptibility $\chi = \epsilon_r - 1$, which is defined as the proportionality in the relation of the dielectric polarization density and the electric field

$$\vec{P} = \epsilon_0 \chi \vec{E}, \quad (1.6)$$

and thus a measure for the polarizability of a material with respect to an electric field.

In terms of the derivation of the wave equations, the electric permittivity and magnetic permeability enter in the speed of light $c = 1/\sqrt{\epsilon_r \epsilon_0 \mu_r \mu_0}$ (for ϵ_r and μ_r being real numbers), which is different inside a medium than in vacuum. Also, the changes in polarization of matter under a changing electric field will not be instantaneous but occur with a delay depending on the material. Thus, the electric permittivity will in general be a function of the frequency ω (or equivalently a function of the photon energy), i.e. $\epsilon = \epsilon(\omega)$, also known as dielectric function. In turn, while being a constant in vacuum with respect to the energy, the speed of light becomes energy dependent once the wave enters the medium [8]. This *dispersion* has consequently also an effect on the value of the wave number k inside the medium in comparison to the vacuum equations in Eq. (1.3), which yields

$$k = \frac{1}{\sqrt{\mu_r \epsilon_r}} k_0 = n k_0, \quad (1.7)$$

where n is the index of refraction taking into account the changes of the wave vector \vec{k} of an electromagnetic field at the interface of vacuum and matter. The delay in polarization response of the material due to electromagnetic waves can be described by a complex valued dielectric function $\epsilon(\omega) = \epsilon_1(\omega) + i\epsilon_2(\omega)$, which accounts for the phase difference due in the polarization density with respect to the electric field and dissipative effects in the matter. In consequence the wave number k and the index of refraction n become complex quantities, with the imaginary part describing the absorption of the electromagnetic radiation during the propagation.

The index of refraction can then be written as,

$$n = 1 - \delta - i\beta, \quad (1.8)$$

where its real part δ accounts for the deviation from the vacuum index of refraction and its imaginary part β for the absorption. The origin of the values of these two parts is strongly dependent on the material and the spectral range of the electromagnetic radiation. Later, we will quickly summarize this dependence for the interaction of matter with EUV and x-ray radiation due to the atomic electronic structure in condensed matter.

Interaction processes

The continuum description above describes the propagation of x-rays and EUV radiation through vacuum and matter in a macroscopic picture. Based on the aforementioned refractive index, the reflective, refractive and dissipative processes at interfaces and in homogeneous materials will be treated for the special case of multilayer systems. However, it is necessary to also give a more general description on the interaction of a photon with the atoms, and more importantly the electrons, of a medium to describe the origin of the fluorescence processes, which are not covered by the continuum description above.

When a photon hits an atom or molecule with its electrons three* very important

* Other processes, e.g. magnetic scattering, can occur as well. However, we limit the description here to the relevant aspects for this work.

THEORETICAL DESCRIPTION OF EUV AND X-RAY SCATTERING

processes can occur, that need to be distinguished.

Elastic Scattering The photon interacts with the matter in an energy conserving way.

We distinguish two limiting cases of a free and a bound electron as scatterers. In the first case, the photon may be scattered out of its original direction by interaction with a single free electron retaining its wavelength (and equivalently its energy). This process is also known as *Thomson scattering*. More generally however, instead of interacting with free electrons, it might encounter a bound electron of an atom forming a dipole with the positive charge of the atom core. In the latter example, the interactions due to the bound nature of the electron have to be considered and affect the scattering process. This scattering by a bound electron is called *Rayleigh scattering* or dipole scattering, which is highly photon energy dependent in its scattering cross section. Both scattering processes can be described within the wave description of the impinging radiation.

Inelastic Scattering Inelastic scattering refers to the case where the photon exchanges a portion of its energy with the system it interacts with resulting in a loss of photon energy and, thus, increased wavelength for the scattered photon. As an example, we shall consider the case of high-energy x-ray photons colliding with free electrons. In that case the total momentum of the system (photon and electron) needs to be taken in to account. A portion of the momentum of the photon (depending on the scattering direction) is transferred to the electron making it recoil. This process is known as *Compton scattering* and it is the result of the particle-wave-duality of electromagnetic radiation. The momentum transfer and thus the change in wavelength depend on the rest mass of the electron. In the low-energy limit, this process becomes negligibly small resulting in simple elastic Thomson scattering.

Absorption The third possibility is that the photon is absorbed by ejecting a bound core shell electron from the atom leaving a vacancy. This is known as *photoelectric effect*. It requires a photon energy exceeding the binding energy of the electron for allowing it to be ejected from the atom. The vacancy on the inner shells is filled by relaxation of electrons from energetically higher core shell states leading to the emission of radiation of lower energy than the initial photon energy. This is called *x-ray fluorescence*, where the emitted photons energy is specific for the element of the atom due to the specific binding energies in the core shell for each element. Another process competing with the emission of fluorescence radiation is the *Auger effect*. Here, instead of emitting the energy of the core shell relaxation as fluorescence radiation, it is transmitted to second electron, which is in turn ejected with reduced energy compared to the photon of the competing x-ray fluorescence process.

1.2.1 Elastic Scattering

Angular resolved scattering of an incoming plane wave is described by the *differential scattering cross section*, defined as

$$\left(\frac{d\sigma}{d\Omega}\right)(\theta, \varphi) = \frac{I_s(\theta, \varphi)}{\Phi_0 \Delta\Omega}, \quad (1.9)$$

where I_s is the scattered intensity into the solid angle $\Delta\Omega$ and Φ_0 is the total flux of incoming photons of the primary wave per unit area. The differential cross section generally has an angular dependence with respect to the position of the observer (detector), the distribution of the scattering matter and the direction of the incoming beam. Here, θ and φ are angular coordinates in a coordinate system with its origin at the scattering center. Due to this proportionality, the goal of calculating the scattering intensity is achieved by determining the differential cross section for the scattering problem at hand. As an example we shall briefly demonstrate the differential cross section of scattering from a single free electron and extend that description to scattering from an arbitrary electron density $\rho_e(\vec{r})$ of free and bound electrons.

Thomson scattering from single free electrons

The scattering cross section in case of a single free electron is given by

$$\left(\frac{d\sigma}{d\Omega}\right)(\theta, \varphi) = \left(\frac{e^2}{4\pi\epsilon_0 mc^2}\right)^2 |\vec{e}_i \cdot \vec{e}_s|^2 = r_e^2 |\vec{e}_i \cdot \vec{e}_s|^2, \quad (1.10)$$

where e is the electron charge and the unit vectors \vec{e}_i and \vec{e}_s describe the direction of the electric field vector before and after the scattering process, respectively. The differential cross section in the case of *Thomson scattering* is proportional to the square of the classical electron radius $r_e = e^2/4\pi\epsilon_0 mc^2$. Depending on the polarization properties of the impinging radiation, the scalar product of the two unit vectors yields

$$|\vec{e}_i \cdot \vec{e}_s|^2 = \begin{cases} 1 & \text{electric field perpendicular to scattering plane} \\ \cos^2(\Delta\Psi) & \text{electric field parallel to scattering plane} \\ \frac{1}{2}(1 + \cos^2(\Delta\Psi)) & \text{unpolarized radiation} \end{cases}, \quad (1.11)$$

where $\Delta\Psi(\theta, \varphi)$ is the total angle between the incoming beam and the scatter direction [2] and lies in the scattering plane spanned by the propagation direction of the incoming and scattered waves.

Rayleigh scattering from bound electrons and Born approximation

In general, the scattering from a single free electron will not be an accurate description for most scattering problems of EUV and x-ray radiation impinging on matter. Instead electrons are bound in an atom or molecule (or in the band structure of a solid) and the radiation is scattered by an electron density associated with the distribution of electrons bound in an atom. The bound nature of the electrons also influences the scattering cross section as we shall summarize here. The result is that the differential cross section obtained for Thomson scattering has to be modified by the *form factor* $f(\vec{q})$ defined through,

$$\left(\frac{d\sigma}{d\Omega}\right)(\theta, \varphi) = r_e^2 |f(\vec{q})|^2 |\vec{e}_i \cdot \vec{e}_s|^2, \quad (1.12)$$

THEORETICAL DESCRIPTION OF EUV AND X-RAY SCATTERING

where $\vec{q} = \vec{k}_f - \vec{k}_i$ the *wavevector transfer* or *scattering vector*. Let us first consider the case of a free electron cloud. A plane wave impinging on a distributed charge distribution will be scattered from all positions of that distribution. The observer located far away from the scatterer detects a superposition of this radiation scattered at each position within the charge density. The individual scattered waves have a path difference from the scatter center to the detector resulting in a phase difference. The form factor, which we shall denote $f^0(\vec{q})$, is then given by

$$f^0(\vec{q}) = \int \rho_e(\vec{r}) e^{-i\vec{q}\cdot\vec{r}} d\vec{r}. \quad (1.13)$$

The exponential function in Eq. (1.13) accounts for the aforementioned phase difference between different scattering centers in the spatial electron distribution [23]. The scattering from a free electron cloud is thus characterized by the Fourier transform of the electron density spatial distribution. In the limiting case of a singular isolated electron (described by a delta function for the electron density), the scattering cross section will just yield the Thomson scattering formula in Eq. (1.10). It is important to note here, that the form factor found in Eq. (1.13) is only valid if the scattering is weak compared to the primary incident wave. For solving the corresponding wave equation one approximates the incoming field at all positions \vec{r} of the electron density with the initial primary wave neglecting any scattered contributions from other positions \vec{r}' . This is called the *Born approximation*. It implicitly corresponds to considering only one single scattering event per incident photon. Multiple scattering processes are not included in this description (kinematic scattering). Later, we will generalize this approximation to more complex, exactly solvable scattering problems instead of considering only the kinematic processes.

The differential cross section in Eq. (1.12) with the form factor $f^0(\vec{q})$ is only valid for free electrons. In case of bound electrons in a atom, molecule or solid, electronic resonances exist which affect the scattering. For EUV and x-ray radiation dipole scattering on light elements, the core shell energy levels are close to the energy of the impinging radiation. In that case the electron response will no longer be that of a free or quasi free electron but influenced due to the fact that it is tightly bound. This effect is called *dispersion* and results in two additional wavelength dependent dispersion factors in the atomic form factor [2, 23], which is now a complex quantity including absorption effects described as

$$f(\vec{q}, \lambda) = f^0(\vec{q}) + f'(\lambda) + i f''(\lambda). \quad (1.14)$$

The *atomic scattering factors* $f'(\lambda)$ and $f''(\lambda)$ are strongly dependent on the element of the atoms involved in the scattering process. The first factor $f'(\lambda)$ accounts for the modified response of an electron close to an electronic resonance, often described in analogy to a driven harmonic oscillator close to its eigenfrequency. The second factor $f''(\lambda)$ describes dissipative processes into the atomic system. It is associated with the absorption of radiation in matter. In fact, both factors, while being related through the so called *Kramers-Kronig relation*, define the complex index of refraction (expressed here for a single element) of the continuum theory introduced above at the beginning of Sec. 1.2 through

$$n = 1 - \delta - i\beta = 1 - \frac{r_e}{2\pi} \lambda^2 n_a f(0, \lambda), \quad (1.15)$$

where n_a is the number of atoms per unit volume [75].

1.2.2 Absorption and Fluorescence

Absorption of electromagnetic radiation, more specifically X-ray radiation, in matter is the third main interaction process mentioned here. In that case, the incoming photon transfers all its energy to an electron leaving it in a energetically excited state. If the energy of the incoming photon is sufficient to excite the electron into the continuum above the binding energy, that electron is ejected from the atom leaving a vacancy at one of the core shells and, thus, leaving the atom in an exited state. The relaxation of electrons in energetically higher shells into the vacancy causes the release of energy. This can happen through two competing processes known as *X-ray fluorescence* and the *Auger effect*. The general principle of X-ray fluorescence is illustrated in Fig. 1.1.

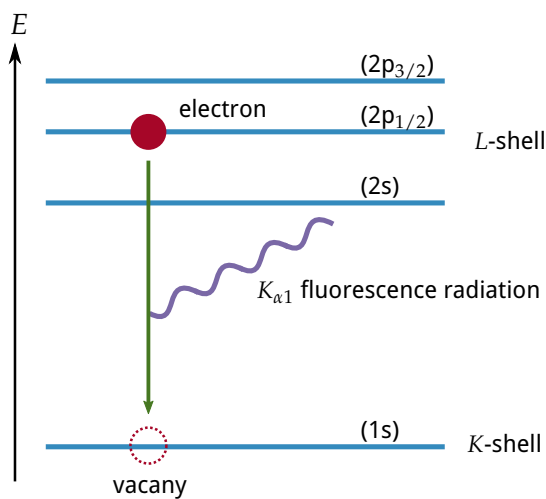


Figure 1.1 | Illustration of *X-ray fluorescence* for an atom. As an example, the relaxation of an *L*-shell electron into the *K*-shell vacancy is shown. That leads to the emission of characteristic $K_{\alpha 1}$ fluorescence radiation at three different energies according to the dipole transition selection rules. The electron configuration of the two shells is given in brackets of the respective energy level (figure not to scale).

Each material exhibits a steady decrease of the interaction cross section when irradiated with radiation of increasing photon energy known as normal dispersion. However, at certain material dependent energies, sharp increases can be observed, also referred to as resonances or ranges of anomalous dispersion. Those jumps correspond to the *K*, *L* and *M* absorption edges of the core shell electrons leading to photoionization of that particular atom creating the above mentioned vacancy. Since the electronic structure of the core shell is specific to a particular element, the emitted fluorescence radiation is characteristic for the material in the sample. That fact is exploited in the X-ray fluorescence (XRF) analysis, where the amount of a specific chemical element inside of matter can be determined by measuring the spectral distribution of the fluorescence radiation.

Finally, instead of emitting fluorescence radiation the energy of the relaxation process into the vacancy can be transferred radiation less to a secondary electron with lower binding energy than the primary, excited electron. In that case, given sufficient energy, the secondary electron can also be ejected with a overall reduced kinetic energy compared to the primary electron. This is the Auger process. In principle, since the binding energy of the secondary electron is specific for the chemical element, Auger electron spectroscopy also offers the possibility for material analysis. However, a limitation is the small median travel distance of electrons in matter making this technique highly surface sensitive and thus unpractical for the analysis of buried material.

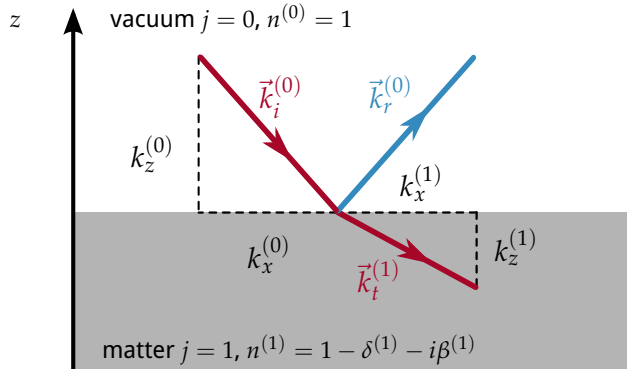
The two processes of fluorescence and Auger emission compete. For elements with low atomic number Z , the Auger process dominates while almost no fluorescence is present.

With increasing atomic number the ratio reverses resulting in a higher fluorescence yield than Auger electron yield for high Z elements and inner shells.

1.3 Specular Reflection from Surfaces and Interfaces in Layered Systems

As mentioned above in the beginning of Sec. 1.2 the reflection and transmission of EUV and x-ray radiation will be treated here with a continuum approach based on the index of refraction. Before we treat specular reflectance and transmittance in multilayer systems, let's recapitulate reflection and transmission through a single surface. Fig. 1.2 gives the necessary definitions for radiation passing through an abrupt interface. The coordinate system was chosen such that the surface is perpendicular to the z-direction and $z = 0$ is at the surface. The refraction process in that case is entirely governed by *Snell's law* known

Figure 1.2 | Illustration of Snell's law. The parallel component of the wave vector $k_x^{(0)} = k_x^{(1)} = k_x$ remains unchanged when the radiation enters the medium. The perpendicular component changes according to the index of refraction (see main text).



from classical optics [15]. Since all measurements in this thesis were conducted with highly linearly polarized light, we give the description of the refraction processes only for the specific conditions found in our experiments. In our case, the electric field vector oscillates perpendicular to the *scattering plane* defined by the incoming wave vector \vec{k}_i and the surface normal. This geometry is referred to as *s-polarization*. For the opposite case of an electric field vector oscillating parallel to the aforementioned scattering plane, known as *p-polarization*, modified forms of the corresponding equations apply not mentioned here.

Considering the interface of vacuum and material, the condition of continuity of both the electric field amplitude and its derivative need to be fulfilled [15, 32]. From that follows that the parallel component of the wave vector $k_x^{(j)} \equiv k_x \forall j$ does not change at the interface. With the solutions of the wave equation for propagation in homogeneous media in the beginning of Sec. 1.2, Snell's law can be expressed in terms of the wave vector by

$$k_z^{(j)} = \sqrt{\left(n^{(j)}k_0\right)^2 - k_x^2} \quad , \text{ with } k_x = \sin(\alpha_i)k_0, \quad (1.16)$$

and the angle of incidence α_i defined from the surface normal (cf. Fig. 1.4) and $n^{(j)}$ is the complex index of refraction of layer j .

Together with the relation in Eq. 1.7 this yields a relation for the perpendicular component of the wave vector and of the electric field amplitudes in vacuum (layer

$j = 0$) and the medium (layer $j = 1$) through the *Fresnel coefficients* of reflection $r^{(0)}$ and transmission $t^{(0)}$ via

$$\begin{pmatrix} E_t^{(1)} \\ E_r^{(0)} \end{pmatrix} = \begin{pmatrix} t^{(0)} E_0 \\ r^{(0)} E_0 \end{pmatrix}, \quad (1.17)$$

where E_0 is the field amplitude of the incident field with wave vector $\vec{k}_i^{(0)}$, $E_t^{(1)}$ is the transmitted field amplitude in layer $j = 1$ with wave vector $\vec{k}^{(1)}$ and $E_r^{(0)}$ is the reflected field amplitude with wave vector $\vec{k}_r^{(0)}$. For the transmission and reflection at any two interfaces j and $j + 1$ the Fresnel coefficients in s-polarization read

$$r^{(j)} = \frac{k_z^{(j)} - k_z^{(j+1)}}{k_z^{(j)} + k_z^{(j+1)}}, \quad (1.18)$$

$$t^{(j)} = \frac{2k_z^{(j)}}{k_z^{(j)} + k_z^{(j+1)}}. \quad (1.19)$$

For the sake of completeness, we shall also give the corresponding Fresnel coefficients in case of p-polarized light impinging on the surface [15],

$$r_p^{(j)} = \frac{k_z^{(j+1)} - (n^{(j+1)} / n^{(j)})^2 k_z^{(j)}}{k_z^{(j+1)} + (n^{(j+1)} / n^{(j)})^2 k_z^{(j)}}, \quad (1.20)$$

$$t_p^{(j)} = \frac{2k_z^{(j)}}{(n^{(j+1)} / n^{(j)}) k_z^{(j)} + (n^{(j)} / n^{(j+1)}) k_z^{(j+1)}}. \quad (1.21)$$

Matrix algorithm for multilayer systems

In this part we extend the calculation above to a system of multiple layers on top of a substrate which is assumed to be infinite. This provides the exact fully dynamic solution of the wave equation for an ideal multilayer system with abrupt interfaces. Thus, all reflections and transmissions at all interfaces are considered, including multiple events. The EUV and X-ray fields were calculated based on the well-established matrix algorithm which is an extension of the above Fresnel coefficient method [15, 54]. The field inside each layer j is described similarly to Eq. (1.17) by their reflected and transmitted field components as

$$E^{(j)}(\vec{r}) = e^{i\vec{k}_{\parallel} \cdot \vec{r}_{\parallel}} (E_t^{(j)}(z) + E_r^{(j)}(z)), \quad (1.22)$$

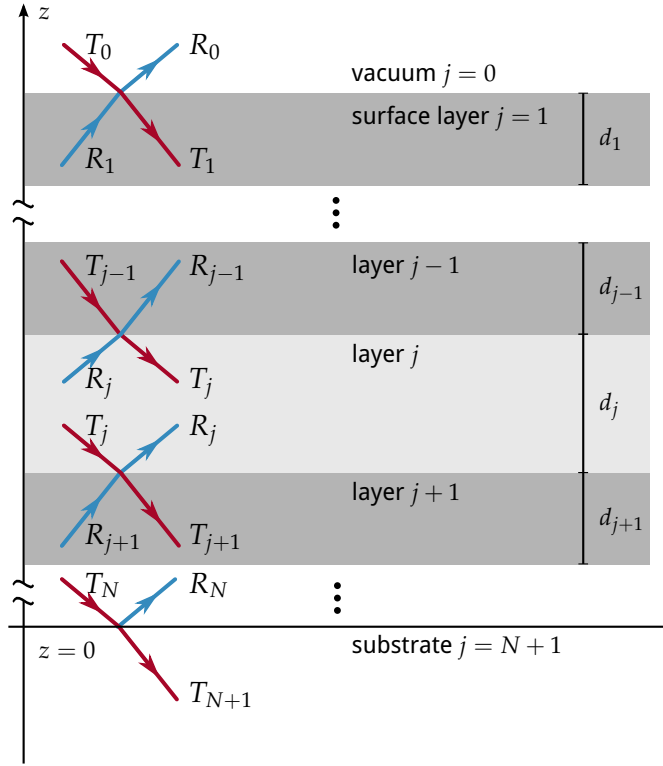
where \vec{k}_{\parallel} is the wave vector component parallel to the interfaces (in the two-dimensional geometry of Fig. 1.2 above was $\vec{k}_{\parallel} = \vec{k}_x$) and \vec{r}_{\parallel} is the position perpendicular to the z-direction. The two field components are further described by the transmitted and reflected field amplitudes T_j and R_j as

$$E_t^{(j)}(z) = T_j e^{ik_z^{(j)} z}, \quad (1.23)$$

$$E_r^{(j)}(z) = R_j e^{-ik_z^{(j)} z}, \quad (1.24)$$

where $E_t^{(j)}(z)$ describes the field component propagating towards the substrate and $E_r^{(j)}(z)$ is the reflected field component in each layer propagating towards the vacuum.

Figure 1.3 | Illustration of the field amplitudes in the exact analytical solution of field propagation through a multilayer stack. The vertical coordinate z is defined to be zero at the substrate interface. The field amplitude of the incident field in the vacuum T_0 is known. Inside the infinite substrate no reflected field amplitude exists, i.e. $R_{N+1} = 0$. The layer thicknesses are denoted d_j for the j th layer.



The field amplitudes and layer thicknesses are illustrated in Fig. 1.3. The components of two adjacent layers are connected by the propagation matrix M_j

$$M_j = \frac{1}{t^{(j)}} \begin{pmatrix} 1 & r^{(j)} \\ r^{(j)} & 1 \end{pmatrix} \begin{pmatrix} e^{-ik_z^{(j+1)}d_{j+1}} & 1 \\ 1 & e^{ik_z^{(j+1)}d_{j+1}} \end{pmatrix}, \quad (1.25)$$

through the relation

$$\begin{pmatrix} E_t^{(j)} \\ E_r^{(j)} \end{pmatrix} = M_j \begin{pmatrix} E_t^{(j+1)} \\ E_r^{(j+1)} \end{pmatrix}. \quad (1.26)$$

The field propagation matrix in Eq. (1.25) includes the Fresnel coefficients from Eq. (1.20) and Eq. (1.19) accounting for the reflection and transmission process at the interface. In between two interfaces a homogeneous layer was assumed so that the field is only propagated by the phase factor $e^{\pm ik_z^{(j)}d_j}$ along the z -direction and the layer thickness d_j . The system of equations in Eq. (1.26) becomes solvable by replicated application of the field propagation matrix to relate the *known* incident field amplitude E_0 , the total reflected field amplitude in the vacuum E_R and the transmitted field in the substrate E_T . Since there can not be a reflected field inside the substrate the system of equations Eq. (1.26) reads

$$\begin{pmatrix} E_0 \\ E_R \end{pmatrix} = \prod_j M_j \begin{pmatrix} E_T \\ 0 \end{pmatrix}, \quad (1.27)$$

with two unknowns E_R and E_T which can be calculated based on this relation. Thereby all field amplitudes at each interface can be obtained. The total reflectance R and transmittance T can then be calculated as the quotient of the (known) incoming field E_0

with the reflected E_R and transmitted field E_T , respectively, as

$$\begin{aligned} R &= |E_R/E_0|^2, \\ T &= |E_T/E_0|^2. \end{aligned} \quad (1.28)$$

Accounting for roughness and interdiffusion

The calculation above yields an exact solution of the problem of reflecting and transmitting EUV or x-ray radiation from and through a generic multilayer. However, in a realistic sample the interfaces will not be perfectly flat and abrupt. Instead the two materials could mix or the interfaces could be rough. Both effects lead to a diminished reflectance of each interface and thus reduce the reflected field amplitudes which changes their interference behavior. These two processes of roughness and interdiffusion can be treated within the framework of the matrix algorithm presented above by using modified Fresnel coefficients. A detailed calculation for arbitrarily rough interface profiles along the z-direction can be found in [79], for example.

For our calculations we assume a Gaussian distribution function of the roughness and interdiffusion. The general expression found in [79] for the modified Fresnel coefficients then yields the result of Nérot and Croce [21, 58]. The Gaussian distribution function corresponds to the assumption of the interdiffusion and roughness profile to be of error-function like shape, which leads to the modified Fresnel coefficients

$$\begin{aligned} \tilde{r}^{(j)} &= r^{(j)} \exp(-2k_z^{(j)} k_z^{(j+1)} \sigma_j^2), \\ \tilde{t}^{(j)} &= t^{(j)} \exp((k_z^{(j)} - k_z^{(j+1)})^2 \sigma_j^2 / 2), \end{aligned} \quad (1.29)$$

where $r^{(j)}$ and $t^{(j)}$ are the unmodified Fresnel coefficients for an ideal multilayer system at each interface j from Eq. (1.20) and Eq. (1.19). The parameter σ_j is the *mean square roughness* or *interdiffusion*, respectively at the j th interface.

1.4 Diffuse Scattering in Layered Systems

For the characterization of a scattering process in general, but here in particular from surfaces or interfaces, it is necessary to define the coordinate system of the momentum transfer. The scattering process from a single surface in reflection geometry is depicted in Fig. 1.4. The incoming beam irradiating the sample under the angle of incidence α_i is described by the wave vector \vec{k}_i . The direction of this vector is the propagation direction

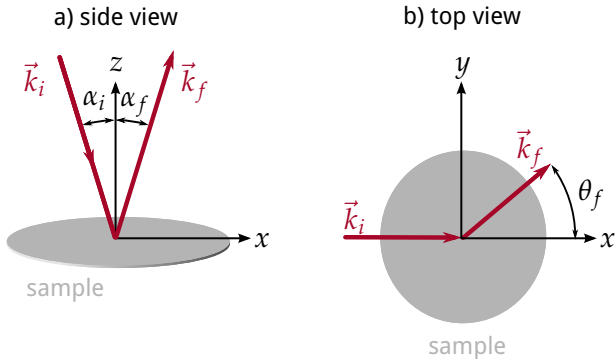


Figure 1.4 | Scattering geometry for the definition of the scattering vector \vec{q} .

of the incident radiation, where its absolute value is the wavenumber $k = |\vec{k}_i| = \frac{2\pi}{\lambda}$. A detector positioned at a different angle, typically called scattering angle α_f , detects the scattered radiation. The outgoing or scattered beam is described by the wavevector \vec{k}_f with direction towards the detector, again in accordance with the propagation direction of the radiation. In case of an elastic, i.e. energy conserving, scattering process its absolute value is the wavenumber of the incoming beam $|\vec{k}_f| = |\vec{k}_i| = k_0$. This general scattering process is characterized by its momentum transfer vector

$$\vec{q} = \vec{k}_f - \vec{k}_i, \quad (1.30)$$

also known as scattering vector. From this definition the components of this three dimensional vector can be expressed by the involved angles and wavelengths as

$$\begin{aligned} q_x &= k(\cos \theta_f \sin \alpha_f - \sin \alpha_i), \\ q_y &= k(\sin \theta_f \sin \alpha_f), \\ q_z &= k(\cos \alpha_f + \cos \alpha_i). \end{aligned} \quad (1.31)$$

The momentum transfer vector is a characteristic quantity for scattering processes. Its three components in Eq. (1.31) span the so called reciprocal space.

Modified wave equation and the distorted-wave Born approximation

Diffuse scattering in the special case of layered systems is the result of imperfections of surfaces or interfaces, which otherwise show only specular (coherent) reflectance. In Sec. 1.2.1 we have elaborated the elastic scattering of EUV and X-ray radiation on an electron density. An important assumption for the results obtained, the Born approximation, is that the scattering is weak with respect to the incoming primary wave. The scattering process thus only considers the primary wave, typically a plane wave, and not the total wave field including the scattered radiation in the theoretical description of the process. This is equivalent to the assumption of a single scattering event ignoring multiple scattering, also known as kinematic scattering. In the context of layered systems, diffuse scattering is described within the framework of perturbation theory with a similar approach.

The existence of a multilayer structure is different from scattering on a simpler system, e.g. an isolated electron cloud. The wave field at the interfaces significantly differs from that of a plane wave due to multiple reflection and transmission processes occurring in a multilayer system. This alternation of the wave field can no longer be considered weak and the Born approximation fails. Instead, the theoretical description of the diffuse EUV scattering from multilayers is based on the DWBA [41, 42], widely used in the analysis of hard X-ray scattering. The DWBA is an extension of the above mentioned Born approximation in which the interfacial roughness is considered to be a small deviation from the ideal multilayer system. In general, the wave equation for a multilayer system is

$$(\Delta + k_0^2)E(\vec{r}) = V(\vec{r})E(\vec{r}), \quad (1.32)$$

with the potential $V(\vec{r}) = k_0(1 - n^2(\vec{r}))$ [60] describing the different materials inside the layer system through their index of refraction n . The DWBA is based on the principle that part of this potential leads to a wave equation which can be solved analytically, while a small disturbance to that potential remains to be treated as perturbation. In case of a multilayer the exact solution of a system with ideal interfaces can indeed be found and

is given in Sec. 1.3. The potential can be separated into a strong part $V_{\text{id}}(\vec{r})$ for which an analytical solution exists and a small perturbation $V_r(\vec{r})$ describing the interfacial roughness as deviation from the ideal layer system, i.e. $V(\vec{r}) = V_{\text{id}}(\vec{r}) + V_r(\vec{r})$. In analogy to the Born approximation, the scattering process is then evaluated considering the wave fields obtained from the solution with the ideal potential $V_{\text{id}}(\vec{r})$ only and calculating a first iteration. Thus, the analytic solution of the multilayer wave equation (“distorted wave”) in the DWBA takes the place of the plane wave in the Born approximation. In that way, the scattering from the perturbations are still considered kinematically (single scattering approximation), however, the incoming distorted waves are exact solutions of the transmittance and reflectance at all layers of the multilayer system.

The distorted-wave Born approximation scattering cross section

The detailed derivation of the diffuse (incoherent) differential scattering cross section for rough multilayer systems can be found in Pietsch, Holý and Baumbach [60] and the corresponding publications [41, 69], as well as in de Boer [13] and Mikulík [54]. Here, we give a summarized version illustrating the application to near-normal incidence scattering and the corresponding approximations leading to the determination of a roughness power spectral density (PSD) for the interfaces in a multilayer system.

The derivation of the diffuse scattering cross section is done by applying the mathematical tools from the quantum mechanical formalism for perturbation theory. There, the transition probability from one state into another is described as the expectance value of the transition matrix. In case of the scattering problem at a multilayer this translates to considering the incoming wave field, given by the exact solution of the wave equation for a multilayer system and calculating the expectance value for scattering into a scattered state arriving at the detector. The latter is generally unknown. However, the reciprocity theorem [46, 50] of classical electrodynamics states that an unknown field at a detector generated by a known dipole source, i.e. the incident field induced dipole at a perturbation of an interface causing the emission of scattered radiation, can be replaced by the time-inverted known field caused by a single dipole source at the detector position (“detector beam”) [22, 41, 69]. The latter is just the time-inverted solution of the same wave equation of the ideal multilayer as for the regular solution. We thus consider two independent solutions of the wave equation (1.32) with $V(\vec{r}) = V_{\text{id}}(\vec{r})$ and express them in Dirac notation [27] as $|E_{\text{id}}^{(1)}\rangle$ and $|E_{\text{id}}^{(2)}\rangle$, where the superscript (1) denotes the regular solution obtained via the matrix algorithm in Sec. 1.3 and the index (2) indicates the time-inverted solution for the scattering angle α_f of the detector position with respect to the surface.* According to Eq. (1.22), Eq. (1.23) and Eq. (1.24) the two solutions can be expressed in terms of the reflected and transmitted field amplitudes as

$$|E_{\text{id}}^{(1)}\rangle = e^{i\vec{k}_{\parallel,(1)} \cdot \vec{r}_{\parallel}} (T_j^{(1)} e^{ik_z^{(j)} z} + R_j^{(1)} e^{-ik_z^{(j)} z}), \quad (1.33)$$

$$|E_{\text{id}}^{(2)}\rangle = (\langle E_{\text{id}}^{(2)} |)^* = e^{-i\vec{k}_{\parallel,(2)} \cdot \vec{r}_{\parallel}} (T_j^{(2)*} e^{-ik_z^{(j)} z} + R_j^{(2)*} e^{ik_z^{(j)} z}). \quad (1.34)$$

These solutions are the basis for the calculation of the differential scattering cross section, which is given by the covariance of the matrix element of the perturbation potential [60]

* In regard to the matrix algorithm in Sec. 1.3 the solution for the time-inverted “detector beam” is obtained by replacing the vacuum wave vector component k_x in Eq. (1.16) with the corresponding component for the scattering angle α_f instead of the angle of incidence α_i .

as

$$\left(\frac{d\sigma}{d\Omega} \right)_{\text{DWBA}} = \text{Cov}(\langle E_{\text{id}}^{(2)} | V_r | E_{\text{id}}^{(1)} \rangle). \quad (1.35)$$

The explicit expression for the covariance can be calculated based on Eq. (1.33) and Eq. (1.34) and yields the full DWBA differential scattering cross section for the diffuse (incoherent) scattering considering all transmitted and reflected fields, i.e. all first order dynamic effects, as

$$\begin{aligned} \left(\frac{d\sigma}{d\Omega} \right)_{\text{DWBA}} = & \frac{A\pi^2}{\lambda^4} \sum_{j=1}^N \sum_{i=1}^N (n_j^2 - n_{j+1}^2)^* (n_i^2 - n_{i+1}^2) \left((T_j^{(1)} + R_j^{(1)})^* (T_j^{(2)} + R_j^{(2)})^* \right. \\ & \times \left. (T_i^{(1)} + R_i^{(1)}) (T_i^{(2)} + R_i^{(2)}) \right) S_{ij}(\vec{q}_{||}; q_z^{(j)}, q_z^{(i)}), \end{aligned} \quad (1.36)$$

where A is the illuminated sample area and $S_{ij}(\vec{q}_{||}; q_z^{(j)}, q_z^{(i)})$ includes the effect of the perturbation potential $V_r(\vec{r})$. For the multilayer system this perturbation is roughness at the interfaces, which can be correlated vertically throughout the stack, as well as in-plane of a single interface. A detailed derivation of the explicit form of that form factor is given in the following paragraph.

In the case of small reflectivity amplitudes, dynamic multiple reflections are often neglected and the dominant term in the decomposition is diffuse scattering of the transmitted fields at the roughness of each interface. The so-called semi-kinematic approximation [69] yields an explicit expression for Eq. (1.35) with

$$\begin{aligned} \left(\frac{d\sigma}{d\Omega} \right)_{\text{semi-kinematic}} = & \frac{A\pi^2}{\lambda^4} \sum_{j=1}^N \sum_{i=1}^N \left((n_j^2 - n_{j+1}^2)^* (n_i^2 - n_{i+1}^2) \right. \\ & \times \left. T_j^{(1)*} T_j^{(2)*} T_i^{(1)} T_i^{(2)} S_{ij}(\vec{q}_{||}; q_z^{(j)}, q_z^{(i)}) \right). \end{aligned} \quad (1.37)$$

The semi-kinematic approximation is similar to the conventional Born approximation, except that it considers the exact transmitted field amplitudes at a certain interface instead of a plane wave. The comparison of this expression with the full first-order DWBA term in Eq. (1.36) is useful to evaluate the contribution of dynamic effects to the scattering cross section and consequently the measured diffuse scattering distribution.

An illustration of the four scattering processes included in the full first-order DWBA is shown in Fig. 1.5 at the example of the interface of layer j and $j+1$ in the multilayer system.

Calculation of the roughness power spectral density

The effect of the perturbation potential is contained within the factor $S_{ij}(\vec{q}_{||}; q_z^{(j)}, q_z^{(i)})$ in Eq. (1.36) and Eq. (1.37). For a multilayer system this perturbation is interfacial roughness as a deviation from the ideal multilayer with sharp and perfectly flat interfaces. The influence of the interfacial roughness on the diffuse scattering intensity described by the explicit form [12, 13]

$$\begin{aligned} S_{ij}(\vec{q}_{||}; q_z^{(j)}, q_z^{(i)}) = & \frac{\exp \left[-((q_z^{(j)*})^2 \sigma_j^2 + (q_z^{(i)})^2 \sigma_i^2)/2 \right]}{q_z^{(j)*} q_z^{(i)}} \\ & \times \int d^2 \vec{X} \left(\exp[q_z^{(j)*} q_z^{(i)} C_{ij}(\vec{X})] - 1 \right) \exp(i \vec{q}_{||} \cdot \vec{X}), \end{aligned} \quad (1.38)$$

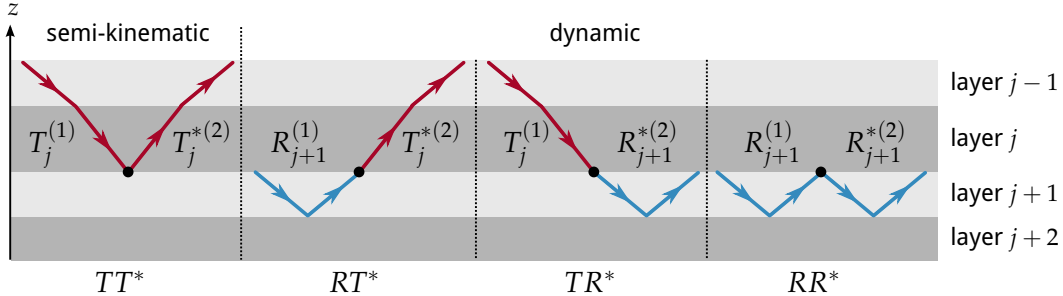


Figure 1.5 | Illustration of the four scattering processes of the DWBA^a. The TT^* process on the left is purely kinematic in nature and equivalent to the Born approximation. The three other processes RT^* , TR^* and RR^* are purely dynamic and not described by kinematic theory. It should be noted here, that the illustration shows a simplified picture. The reflection and transmission amplitudes in the respective layers contain all reflections and transmission of all preceding and following interfaces. They represent the full field in the respective interface with all components propagating towards the vacuum (R , T^*) and the substrate (T , R^*).

^a Figure similar to Pietsch, Holý and Baumbach [60].

where $q_z^{(i)}$ is the z -component of the scattering vector \vec{q} at the i th interface, $\vec{X} = \vec{x} - \vec{x}'$ is the lateral distance vector and $C_{ij}(\vec{x} - \vec{x}') = \langle h_i(\vec{x})h_j(\vec{x}') \rangle$ is the height correlation function of the interface profiles $h_i(\vec{x})$ of the interfaces i and j , respectively. The factor σ_j is the root mean square (r.m.s.) roughness of the j th interface.

We consider the situation, where the roughness is small in relation to the scattering vector. This assumption is valid especially for high-quality multilayer systems as the mirrors considered in the framework of this thesis. This is the so-called small roughness approximation. In that case, the product of roughness and the z -component of the scattering vector is small, i.e. $q_z^{(j)*}\sigma_j \ll 1$. We therefore can approximate the first part of Eq. (1.38) by

$$\frac{\exp \left[-((q_z^{(j)*})^2\sigma_j^2 + (q_z^{(i)})^2\sigma_i^2)/2 \right]}{q_z^{(j)*} q_z^{(i)}} \approx \frac{1}{q_z^{(j)*} q_z^{(i)}} \quad (1.39)$$

and Taylor expand the integrand as $\exp[q_z^{(j)*}q_z^{(i)}C_{ij}(\vec{X})] - 1 \approx q_z^{(j)*}q_z^{(i)}C_{ij}(\vec{X})$. With these approximations Eq. (1.38) reduces to

$$S_{ij}(\vec{q}_\parallel) \approx \int d^2\vec{X} C_{ij}(\vec{X}) \exp(i\vec{q}_\parallel \cdot \vec{X}). \quad (1.40)$$

$S_{ij}(\vec{q}_\parallel)$ is, thus, the Fourier transform of the correlation function $C_{ij}(\vec{X})$. Assuming identical growth for the individual layers, i.e. a material independent propagation of roughness along the z -direction, $S_{ij}(\vec{q}_\parallel)$ can be expressed in terms of the lateral PSD $C_i(\vec{q}_\parallel)$ and a vertical replication factor $c_{ij}^\perp(\vec{q}_\parallel)$ [72],

$$S_{ij}(\vec{q}_\parallel) = c_{ij}^\perp(\vec{q}_\parallel) C_{\max(i,j)}(\vec{q}_\parallel). \quad (1.41)$$

PSD functions based on different models of lateral interface roughness correlation have been proposed, e.g. by Sinha et al. [69]. We follow the approach by de Boehr et al. [10, 12] for fractal interface roughness, where the lateral correlation function of the i th interface is given by

$$\tilde{C}_i(\vec{X}) = P_i \xi_\parallel^{H_i} |\vec{X}|^{H_i} K_{H_i}(|\vec{X}|/\xi_\parallel). \quad (1.42)$$

THEORETICAL DESCRIPTION OF EUV AND X-RAY SCATTERING

H_i is the Hurst factor providing a measure for the jaggedness of the interface [69], K_{H_i} are the modified Bessel functions of the order H_i , ξ_{\parallel} is a lateral correlation length and

$$P_i = \frac{\sigma_i^2}{\xi_{\parallel}^{H_i-1} 2^{H_i-1} \Gamma(1+H_i)/H_i}. \quad (1.43)$$

The multilayer mirror samples investigated within this thesis are highly-reflective samples fabricated with state of the art deposition processes. We therefore expect a highly periodic and highly-stable vertical replication of roughness. While a distinction of the roughness at the individual interfaces is theoretically possible, the experimental method always irradiates all interfaces simultaneously. Thus, reconstructing the parameters describing roughness of all interfaces individually is not possible due to the indistinguishability of the contribution of separate interfaces. Such a model would be ill-defined based on the scattering data recorded. Instead, our goal is to determine a single average power spectral density. We thus assume identical roughness properties for all interfaces in our model. Hence $\sigma_j = \sigma$, $H_j = H$ and $C_{\max(i,j)}(\vec{q}_{\parallel}) = C(\vec{q}_{\parallel})$. The PSD is given by the Fourier transform of Eq. (1.42) with respect to q_x , which yields the closed analytic form

$$C(\vec{q}_{\parallel}) = \frac{4\pi H \sigma^2 \xi_{\parallel}^2}{(1 + |\vec{q}_{\parallel}|^2 \xi_{\parallel}^2)^{1+H}}. \quad (1.44)$$

Vertical correlation of roughness

The high degree of thickness stability for well-defined multilayers as is necessary for high-performance mirrors implies a high degree of vertical correlation of individual interfaces roughness throughout the stack. In order to derive the replication factor in Eq. (1.41), we follow Stearns et al. [73]. In this model, the evolution of the surface roughness $w(x, y)$ during the growth of a single layer is described by the Langevin equation. In its Fourier transformed form,

$$\frac{\partial w(f)}{\partial t} = -4\pi^2 v f^2 w(f) + \frac{\partial \eta(f)}{\partial t}, \quad (1.45)$$

where v is a diffusion-like parameter, $\eta(f)$ is random noise normalized to the layer thickness and $w(f)$ describes the roughness evolution in dependence of the spatial frequency f . The roughness evolution during the growth of a single layer of a specific material can then be evaluated by discretizing Eq. (1.45) for the successive deposition of material of thickness δd

$$w_i(f) = c_{\perp}(f; \delta d) w_{i-1}(f) + \eta(f), \quad (1.46)$$

where $c_{\perp}(f; \delta d)$ is the replication factor of roughness for a single deposition. In the limit of repeated infinitesimal depositions until the full n th layer of thickness d_n is grown, $c_{\perp}(f, d_n)$ can be evaluated to be [72]

$$\begin{aligned} c_{\perp}(f, d_n) &= \exp(-4\pi^2 f^2 v d_n) \\ &= \exp(-|\vec{q}_{\parallel}|^2 v d_n), \end{aligned} \quad (1.47)$$

with $|\vec{q}_{\parallel}|^2 = 4\pi^2 f^2$. Assuming identical diffusion-like behavior v for all materials of a multilayer and defining $\xi_{\perp}(\vec{q}_{\parallel}) = 1/(v|\vec{q}_{\parallel}|^2)$, the replication factor in Eq. (1.41) is given

by

$$c_{ij}^\perp(\vec{q}_\parallel) = \exp\left(-\sum_{n=\min(i,j)}^{\max(i,j)-1} d_n / \xi_\perp(\vec{q}_\parallel)\right). \quad (1.48)$$

Here, $\xi_\perp(\vec{q}_\parallel)$ can be interpreted as a spatial frequency dependent vertical correlation length, describing the distance perpendicular to the stack until the replication factor decreased to $1/e$.

Off-axis vertical roughness correlation

Gullikson et al. [34] observed that the direction of the vertical replication of roughness can be tilted with respect to the surface normal. Including this effect in the differential cross section, requires a coordinate transformation in reciprocal space to account for the tilt angle β according to

$$\bar{q}_z = q_z - \hat{e} \cdot \vec{q}_\parallel \tan \beta, \quad (1.49)$$

where \hat{e} is a unit vector in direction of the roughness replication. Since the vertical scattering vector components enter the calculations through the Fresnel coefficients in Eq. (1.20) and Eq. (1.19), an additional factor appears in the calculation of Eq. (1.41) through substitution by

$$\overline{S_{ij}}(q_x) = \exp\left(-i\hat{e} \cdot \vec{q}_\parallel \tan \beta(z_i - z_j)\right) S_{ij}(q_x), \quad (1.50)$$

where z_i is the z -position of the i th interface.

Full DWBA expression for near-normal incidence scattering

Taking together all the above findings and inserting them into Eq. (1.36), the full explicit expression for the DWBA scattering cross section on high-quality multilayer systems is given by

$$\begin{aligned} \left(\frac{d\sigma}{d\Omega}\right)_{\text{DWBA}} = & \left[\frac{A\pi^2}{\lambda^4} \sum_{j=1}^N \sum_{i=1}^N (n_j^2 - n_{j+1}^2)^* (n_i^2 - n_{i+1}^2)^* ((T_j^{(1)} + R_j^{(1)})^* (T_j^{(2)} + R_j^{(2)})^* \right. \\ & \times (T_i^{(1)} + R_i^{(1)}) (T_i^{(2)} + R_i^{(2)}) \Big) \exp\left(-iq_x \tan \beta(z_i - z_j)\right) c_\perp^{ij} \Big] C(q_x). \end{aligned} \quad (1.51)$$

Since all experiments in this thesis have been conducted in co-planar geometry, i.e. for in-plane scattering measurements with a vanishing azimuthal angle θ_f in Fig. 1.4, the parallel component of the scattering vector \vec{q} is given by its q_x component only, i.e. $\vec{q}_\parallel \equiv q_x$, by choice of the coordinate system for the reciprocal space. We define the x , y and z components of the reciprocal space vector in Eq. (1.31) to be parallel to the respectively labeled real space vectors in Fig. 1.4. The angle β is thus determined based on that scattering direction only and dependent on the direction from which the sample is irradiated. The replication factor c_\perp^{ij} and the PSD then read

$$c_\perp^{ij}(q_x) = \exp\left(-\sum_{n=\min(i,j)}^{\max(i,j)-1} \frac{d_n q_x^2}{\xi_\perp}\right), \quad (1.52)$$

where the definition $\xi_{\perp} = 1/v$ holds and

$$C(q_x) = \frac{4\pi H \sigma^2 \xi_{\parallel}^2}{(1 + q_x^2 \xi_{\parallel}^2)^{1+H}}, \quad (1.53)$$

in the explicit expression of Eq. (1.51).

In addition it should be noted here, that Eq. (1.51) separates the contribution to the scattering distribution of the multilayer and vertical correlation (in square brackets) on the one hand and the in-planar roughness represented through the PSD $C(q_x)$ on the other hand.

1.5 Grazing-incidence X-ray Fluorescence

X-ray fluorescence analysis is an established method to characterize the chemical composition of materials through the irradiation of samples with x-rays. It is based on the emission of characteristic fluorescence radiation, as elaborated on in Sec. 1.2.2. By irradiating an unknown sample with photons of sufficiently high energy, those photons are absorbed leaving the characteristic vacancies in the K , L and M core shells. The following recombination processes causes the emission of fluorescence radiation, which can be detected outside the sample. A quantitative analysis was developed by Sherman [67] and refined by others [20, 63, 68]. The *Sherman equation* links the emitted and measured characteristic fluorescence radiation to the material concentration of a specific chemical species via fundamental parameters and the measurement characteristics (experimental parameters) [64]. The quantitative analysis requires a detailed knowledge of the fundamental parameters as well as all experimental parameters and only considers absorption according to the Beer-Lambert law [2]. This is a very elaborate procedure. However, for the purpose of analyzing special distribution of different materials in periodic multilayer structures irradiated under grazing incidence, a relative analysis of the measured fluorescence yield already delivers valuable spatial information on the distribution of chemical species.

Here, we therefore focus on the treatment of fluorescence emission by periodic multilayer systems, which posses a Bragg resonance, i.e. a pair of angle of incidence and photon energy which cause constructive interference at the interfaces. The requirement to excite the Bragg resonance thus intrinsically connects the angle of irradiation with the wavelength of the radiation, in our case this requires grazing angles of incidence. Before entering the details, let us review the aspects of generation of fluorescence radiation. The appearance of fluorescence radiation is linked with the electromagnetic field intensity of the impinging radiation for each infinitesimal volume element inside the sample through a proportionality

$$I_{\text{XRF}} = C \int |E(\vec{r})|^2 \rho(\vec{r}) d^3r, \quad (1.54)$$

where C is a constant, $|E(\vec{r})|^2$ is the field intensity and, here, $\rho(\vec{r})$ is the relative density at the position \vec{r} of the chemical species of which the characteristic fluorescence radiation intensity is measured. This expression is an approximation, since it ignores any self-absorption effects that may occur during the propagation of the fluorescence radiation through the material before reaching the detector. However, for strongly periodic systems

as we shall discuss in this chapter, and a relative comparison of the intensities the effect of self-absorption does not change and can be omitted.

In case of laterally infinitely extended and invariant multilayer systems, i.e. for samples which are larger than any impinging beam and have the same layer stacking for all these points, the field intensity $|E(\vec{r})|^2$ only varies with the vertical coordinate z and thus reduces to $|E(\vec{r})|^2 = |E(z)|^2$ for a given angle of incidence and photon energy [11]. If the layer stacking is known, that intensity can be calculated with the matrix formalism elaborated on in Sec. 1.3. The intensity of the fluorescence radiation from those systems simplifies Eq. (1.54) to

$$I_{\text{XRF}} = \tilde{C} \int_0^D |E(z)|^2 \rho(z) dz, \quad (1.55)$$

where D is the total thickness of all layers of the stack and $E(z) = E_t^{(i)}(z) + E_r^{(i)}(z)$ is given by Eq. (1.23) and Eq. (1.24) for the respective layer i depending on the coordinate z . We define d_i as the thickness of each layer i , and thus $D = \sum_i d_i$. This formula is only valid if the fluorescence radiation is not emitted by the substrate on which the multilayer stack was deposited, since in that case the wave intensity inside the substrate has to be considered as well.

The integral in Eq. (1.55) has to be evaluated for all points z inside each layer i . The matrix algorithm as outlined in Sec. 1.3 yields only the field amplitudes at the interfaces of two materials of the stack. To numerically evaluate the integral we thus discretize the multilayer stack by subdividing the whole stack and thereby each layer into equidistant sublayers with a sufficient number of samples*. Fig. 1.6(a) shows an exemplary Cr/Sc multilayer system with the relative Sc density ρ_{Sc} in each layer. In order to numerically calculate the integral in Eq. (1.55), the system was divided into sublayers of thickness d_i and bottom interface positions z_i as described above and illustrated in Fig. 1.6(b). The integral thus turns into a discrete sum as

$$I_{\text{XRF}} = \tilde{C} \sum_i^M |E(z_i)|^2 \rho(z_i) d_i, \quad (1.56)$$

where M is the total number of sublayers of the whole stack.

In case of a theoretical multilayer system with perfectly sharp interfaces and no interdiffusion, the relative density of ρ_{Sc} in the given example will be binary, i.e. either $\rho_{\text{Sc}} = 1.0$ in the Sc (sub-)layers or $\rho_{\text{Sc}} = 0.0$ in the Cr layers. That, however, does not reflect a realistic situation, where interdiffusion of interface imperfections could lead to a mixture of the two materials in the sublayers. The third example in part (c) of Fig. 1.6 refers to a more realistic case, where the two materials interdiffuse with asymmetric interface regions. There, the relative Sc density ρ_{Sc} varies gradually from the highest value a to its lower value b . In general, a and b will not attain the values 1.0 and 0.0, respectively, as in the cases (a) and (b). That is, because the possibility exists that the two materials interdiffuse so strong, that no region with pure Sc or pure Cr remains.

* The necessary number of samples for a given system can be determined heuristically by evaluating the calculated fluorescence signal for an increasing number of sublayers until the numerical change of the result saturates.

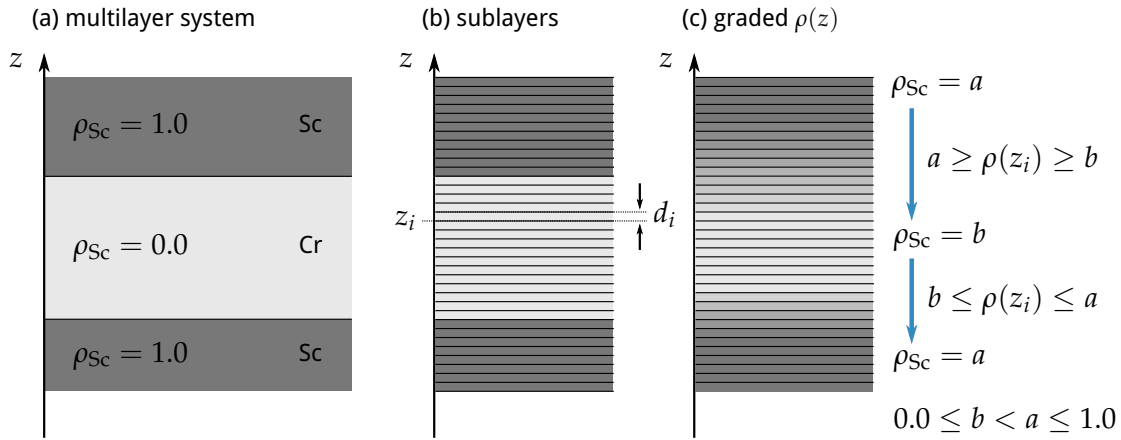


Figure 1.6 | Multilayer scheme to illustrate the method of calculating the x-ray fluorescence yield by the example of Sc in a Cr/Sc multilayer. The multilayer system (a) is split into multiple equidistant sub-layers (b) to obtain the field intensity at discrete points inside the Sc and Cr layers by applying the matrix algorithm in Sec. 1.3. The relative density of Sc ρ_{Sc} is multiplied by the respective intensity inside each sublayer. In case of a more realistic intermixed system, the intensity is calculated similarly to (b) for discrete equidistant sub-layers. However, they differ by their relative Sc density, which is now generally different for each layer (c).

The x-ray standing wave analysis of periodic multilayer systems

The section above covers the case of general multilayer systems. Here, we now shall consider the special case of strongly periodic layers [26, 31], such as multilayer mirror systems for the examples given in Fig. 1.6(a,b) and 1.6(c). For the exemplary calculation, first we choose the layer thicknesses to be $d_{Sc} = 0.6$ nm and $d_{Cr} = 0.7$ nm periodically replicated $N = 400$ times with perfectly sharp interfaces, i.e. the case (a) and (b) of Fig. 1.6, we obtain a one-dimensional artificial Bragg crystal. Radiation of 6.25 keV is well above the K -absorption edges of both materials and thus causes the emission of the K -line fluorescence radiation. For grazing angles of incidence between $\alpha_i^{GI} = 3.7^\circ$ and $\alpha_i^{GI} = 3.9^\circ$ and for this photon energy the reflected field amplitudes at each interface interfere constructively causing the appearance of the first order Bragg peak of the periodic layer structure. The corresponding calculation employing the matrix method from Sec. 1.3 is shown in Fig. 1.7(a).

The constructive interference in the Bragg condition, in addition to resulting in a high reflectance, causes the formation of a X-ray standing wave inside the layers. The corresponding intensity distribution in the top first few layer pairs for the example given here is shown in Fig. 1.7(c). The standing wave intensity shifts through the individual layers thereby selectively exciting fluorescence radiation in the respective chemical species while changing the angle of incidence across the Bragg peak. Thus, this yields a method for chemically selective composition analysis with spatial resolution in the sub-nanometer regime called X-ray standing wave (XSW) analysis. The response curves of the respective relative fluorescence radiation intensity across the Bragg peak for both materials is shown in Fig. 1.7(b). In this example, the fluorescence radiation was calculated according to the discrete sum in Eq. (1.56) with a sublayer setup as indicated in Fig. 1.6(b) and 30 sublayers per layer pair in each period.

We extended the example above to the case of imperfect layer stacks with interdiffusion and strongly asymmetric interface region thickness. The corresponding calculation is then calculated according to the scheme given in Fig. 1.6(c) and is added for comparison

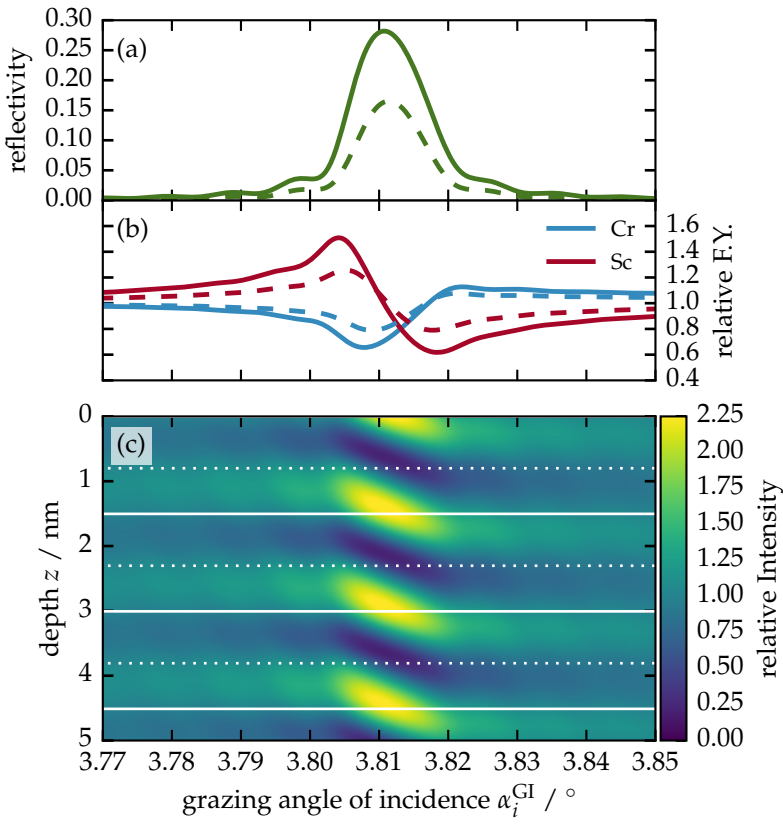


Figure 1.7 | Illustration of the grazing incidence X-ray standing wave fluorescence analysis. The exemplary system shown is a bilayer multilayer mirror of Cr and Sc irradiated with a 6.25 keV photon beam at grazing angles. Changing the grazing angle of incidence α_i^{GI} across the first Bragg peak (a) causes a standing wave inside the multilayer (total intensity in first top layers shown in (c)) and cause a relative fluorescence yield for the two different materials as shown in (b). The dotted lines in (a) and (b) indicate the case of interdiffusion and strongly asymmetric interface regions for comparison.

to the reflectance and fluorescence yield curves in Fig. 1.7(a) and 1.7(b) as dotted lines. The diminished contrast causes a decrease in the peak reflectance of that multilayer system as well as changes in the fluorescence yield.

2

Experimental Setup and Sample Systems

2.1 Synchrotron Radiation

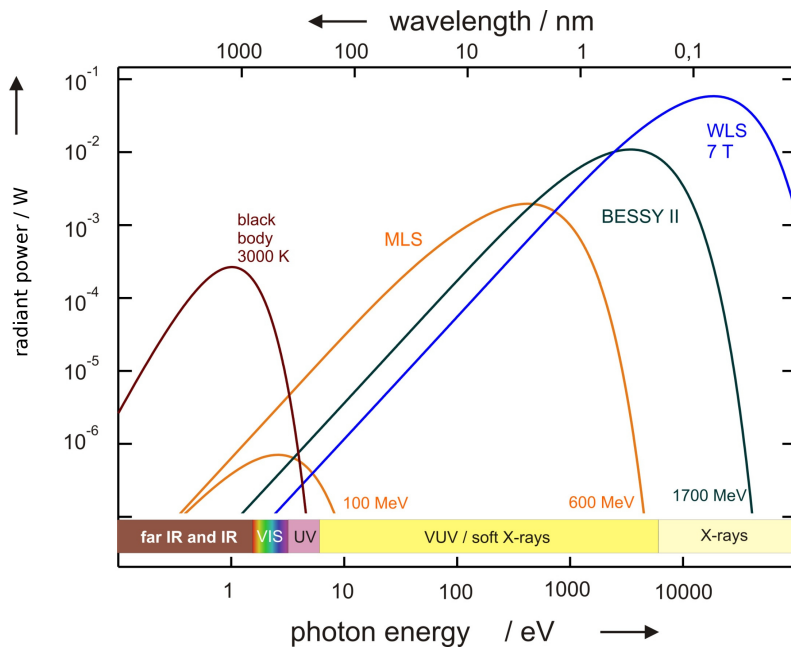
The radiation emitted by a relativistic charged particle, usually electrons, accelerated to a circular orbit through an external magnetic field is called synchrotron radiation. This radiation is polarized and emitted tangentially to the circular movement of the charged particle in forward direction. In the history of synchrotron radiation, sources have evolved from parasitic use of particle accelerators to the extend of building electron storage rings dedicated for the sole purpose of generating this radiation [57]. Its most prominent features are the high brilliance, that is the number of photons per second per unit particle beam cross section and per unit solid angle within 0.1% bandwidth at a specific wavelength, and its huge spectral range of emission. Depending on the energy of the relativistic particles forced on a circular orbit, in modern electron storage rings typically in the order of one to several GeV, the emission covers the range from the terahertz into the hard X-ray regime. The Physikalisch-Technische Bundesanstalt (PTB) operates two laboratories at the dedicated sources BESSY II and the metrology light source (MLS) [16]. The two third-generation synchrotron radiation sources provide maximum electron energies of 1.7 GeV (electron storage ring for synchrotron radiation (BESSY II)) and 0.6 GeV (MLS), respectively. Theoretical emission spectra for a single dipole magnet (*bending magnet*) are shown in Fig. 2.1 in comparison to black body radiation.

A very important theoretical aspect of synchrotron radiation, apart from the high brilliance and large spectrum, is the fact that the emission can be calculated exactly from first principles of classical electrodynamics and special relativity. The theory for synchrotron radiation was developed by Schwinger [66] and we shall review its most important aspects here. Given all the fundamental and experimental parameters are known, the total emitted radiant power per relativistic particle can be calculated exactly

EXPERIMENTAL SETUP AND SAMPLE SYSTEMS

Figure 2.1 | Theoretical synchrotron radiation radiant power spectra for the MLS and BESSY II in comparison to black body radiation^b. The curves show the radiant power of emission for bending magnets at both electron storage ring facilities for different electron energies. The curve marked WLS shows the radiant power from the 7 Tesla wavelength shifter insertion device installed at BESSY II.

^b Image taken from Beckhoff et al. [7]



as

$$P = \frac{1}{4\pi\epsilon_0} \frac{2}{3} \frac{e^2 c}{R^2} \left(\frac{E}{m_0 c^2} \right)^4, \quad (2.1)$$

where e is the elementary charge, c is the speed of light in vacuum, E is the particles energy, m_0 is the rest mass of the particle and R is the radius of the circular trajectory imposed by the magnetic field. The radiant power is thus inversely proportional to the fourth power of the particles rest mass, which explains the usage of light electrons in comparison with significantly heavier protons in synchrotron radiation sources. The dependence on the electron energy is visible in another characteristic value for the emitted radiant power, visible as a shift to higher photon energies (smaller wavelengths) in Fig. 2.1, known as the critical energy or critical wavelength [66], respectively,

$$E_C = \frac{3hc}{4\pi R} \left(\frac{E}{m_0 c^2} \right)^3. \quad (2.2)$$

It marks the point in the spectrum, where the integrated radiant power for all values above and below the critical energy are equal [5]. This formula quantifies the shift towards higher energies due to the increase of the electron energy comparing the MLS and BESSY II emission spectra. Apart from the spectral distribution, the emitted radiation is linearly polarized with an electric field vector oscillating parallel to the plane of the circular orbit. This property, however, is only strictly valid for the emission inside this plane. For radiation above or below, a vertical polarization component (parallel to the surface normal of the orbital plane) exists. The energy W emitted by a single electron on a circular orbit per unit solid angle $d\Omega$ and per unit angular frequency interval $d\omega$ is described by

$$\frac{d^2W}{d\Omega d\omega} = \frac{e^2 R^2}{36\pi^3 \epsilon_0 \gamma^4} \omega^2 (1 + (\gamma\Psi)^2) \left(K_{2/3}^2(\zeta) + \frac{(\gamma\Psi)^2}{1 + (\gamma\Psi)^2} K_{1/3}^2(\zeta) \right), \quad (2.3)$$

where $\gamma = E/m_0 c^2$ and Ψ is the angle between the orbital plane and the observation direction outside of that plane [66]. The argument of the modified Bessel funktions of

second kind $K_x(\zeta)$ is defined as

$$\zeta = \frac{R\omega}{3c\gamma^3} (1 + (\gamma\Psi)^2)^{\frac{3}{2}}. \quad (2.4)$$

The ability to calculate the exact emission and polarization properties of synchrotron radiation based on Eq. (2.3) with a given electron current and acceptance angle have another very valuable side effect for the field of metrology. It enables the use of synchrotron radiation as a primary standard for electromagnetic radiation within the available spectral range, which is in fact exploited by the PTB [76] to provide absolute radiometry.

The dedicated synchrotron radiation facilities, such as BESSY II and the MLS provide additional possibilities of generating synchrotron radiation beyond a simple bending magnet through different insertion devices. Fig. 2.2 gives a schematic overview over the storage ring BESSY II. At each of the marked dipole magnets, synchrotron radiation is produced according the theory presented above. The radiation is transmitted through outlet systems towards a large number of beamlines, which monochromatize and focus the radiation for experimental applications. Undulators or wigglers are inserted in the

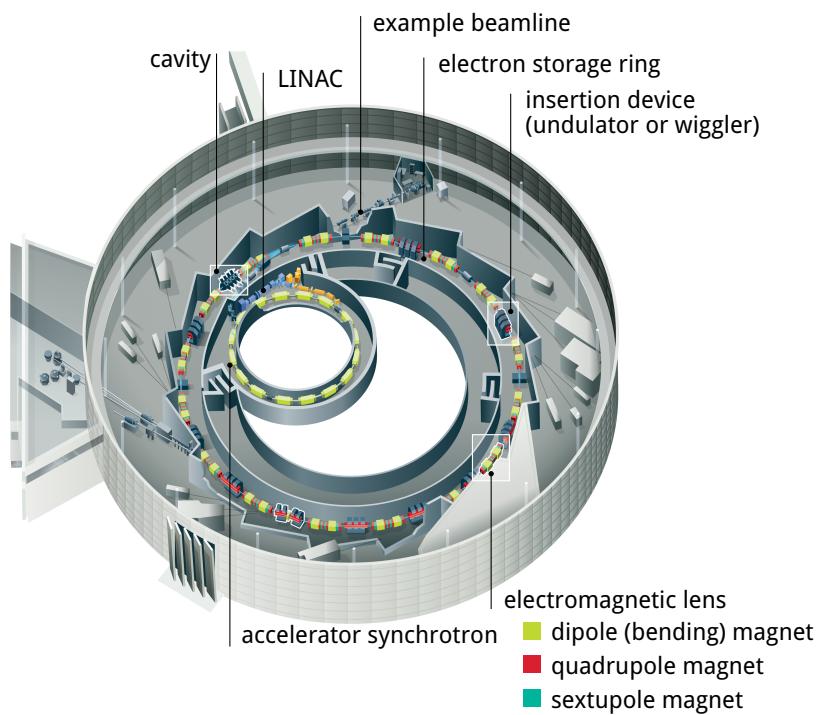


Figure 2.2 | Schematic overview of the electron storage ring facility BESSY II^a. The synchrotron accelerates the electrons coming from the linear accelerator (LINAC), which are then injected in the electron storage ring with their full desired energy. Electromagnetic lenses focus and stabilize the beam, as well as deflecting it onto the circular orbit while emitting synchrotron radiation at each dipole (bending) magnet. Cavities reaccelerate the electrons in the storage ring to compensate the energy loss due to the radiation emission.

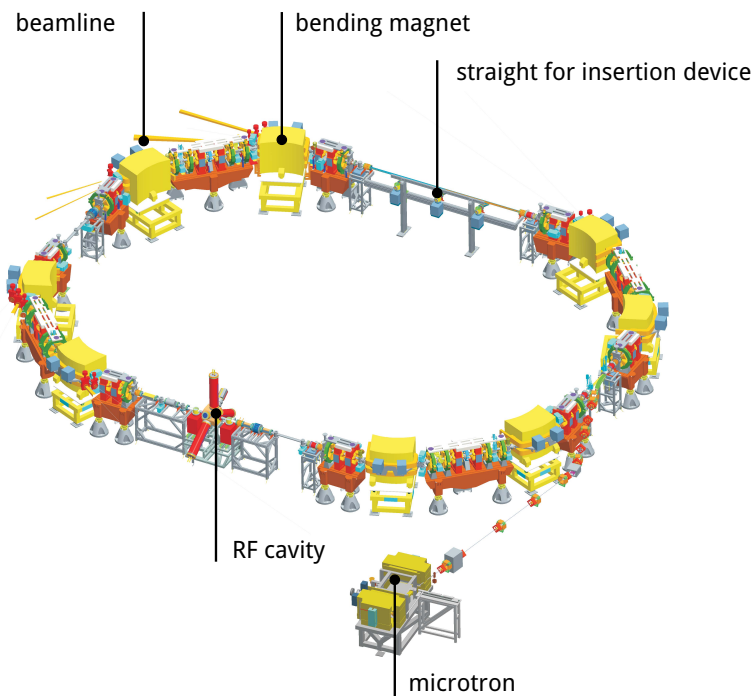
^a Original image by Helmholtz-Zentrum Berlin (HZB), Ela Strickert, source: <https://www.helmholtz-berlin.de/mediathek/bildarchiv/>

straight sections of the BESSY II storage ring with a large number of periodically arranged magnets with alternating polarization forcing the electrons on a sinusoidal beam path. The goal of these insertion devices is to shift the critical energy of the storage ring towards

EXPERIMENTAL SETUP AND SAMPLE SYSTEMS

higher energies (wigglers) or to dramatically increase the brilliance within a significantly smaller spectral range compared to bending magnets (undulators). The different effect of the undulators and wigglers on the generated spectrum is determined by the magnetic field strength B_0 and the distance between two identical periodic arrangements of the magnets of alternating polarization λ_0 . The deflection parameter quantifies this relation through $K \propto B_0 \lambda_0$. Undulators typically have deflection parameters $K < 1$ while in case of wigglers $K \gg 1$ [57]. Technically, the magnetic field strength can be varied by changing the distance (“gap”) between the magnets vertically. By changing the vertical alignment of the magnetic field direction with respect to the beam path, it is even possible to affect the polarization properties of the emitted radiation to obtain circularly or elliptically polarized radiation.

Figure 2.3 | Schematic overview of the electron storage ring facility MLS



The most advanced light source available today, also known as fourth generation source, is following the concept of a free-electron laser (FEL) as first invented by Madey [52]. In that case radiation is produced by a typically single very long undulator inside a linear accelerator instead of a comparatively short straight section of a storage ring. The concept was first demonstrated by Deacon et al. [24]. FEL sources produce highly coherent radiation in the x-ray regime through the principle of self-amplified spontaneous emission (SASE) [14, 25]. Here, the emitted radiation inside the long undulator has a feedback effect on the electron bunch travelling along the beam path. The result is a microbunching of the electron cloud through the electric field of the emitted radiation connected with a (random) wavelength within a certain spectral range defined by the undulator properties. The microbunching causes amplification of that wavelength, which causes an emission spectrum showing several spikes of amplified wavelengths with a noisy background until a saturation level is reached [56].

2.2 The Instrumentation for the EUV Spectral Range

2.2.1 The EUV Beamlines at BESSYII and MLS

The radiation generated in bending magnets or in insertion devices in synchrotron radiation sources typically requires monochromatization and focussing through a series of optical elements depending on the experimental requirements or designated use cases. In addition, radiation in the EUV spectral range is absorbed quickly during propagation under atmospheric conditions. It is thus necessary to maintain a high vacuum from the source points to the experiment and the detector. The two PTB beamlines for the EUV spectral range at the two storage rings BESSY II and MLS operate on the broad spectrum emitted by bending magnets at each facility. The experiments conducted in the framework of this thesis were performed at both beamlines, exploiting the different radiant power in the required spectral range of the respective experiments. The two beamlines share many technical and design aspects. Thus, the description here will introduce most of these aspects with respect to the SX700 beamline at BESSY II. The differences of the EUVR at the MLS will be given below.

The Soft X-ray Beamline SX700

The soft x-ray beamline (SX700) at BESSY II provides a monochromatic beam in the spectral range from 0.7 nm to 24.8 nm wavelength (corresponding to photon energy range from 50 eV to 1800 eV) [7]. The total radiation power and the corresponding relative bandwidth at that beamline are shown in Fig. 2.4. The beam size at the entrance aperture to the reflectometer (experimental end station) is variable through the setting of the exit slits. In the standard setting is approximately 1 mm by 1 mm [65] and can be reduced to 0.1 mm vertical extent (grating dispersion direction) and 0.5 mm horizontal extent.

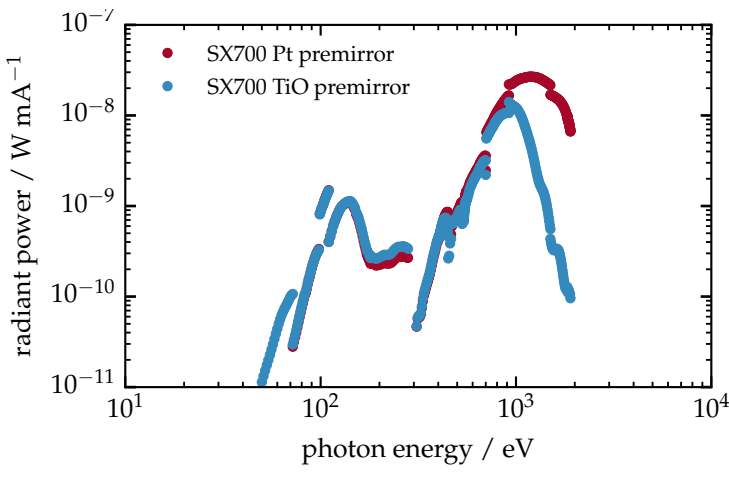


Figure 2.4 | Radiant power of the SX700 beamline at BESSY II in W per mA storage ring ring current. The two curves differ by the coating on the premirror in the beamline. The TiO coating provides the ability to achieve energies down to 50 eV, while the Pt coating ensures high radiant power in the high energy range up to 1800 eV.

The monochromatization of the radiation is achieved by a plane grating monochromator with a blazed line grating with 1200 lines per millimeter mounted with its rotational axis within the plane of the storage ring and illuminated perpendicular to the grating lines, yielding the dispersive direction being perpendicular to the storage ring plane. The schematic layout of the beamline is illustrated in Fig. 2.5 including the plane grating position of the monochromator, the focussing mirrors and slit positions. The selection of the desired wavelength at the position of the experimental chamber is done by a

EXPERIMENTAL SETUP AND SAMPLE SYSTEMS

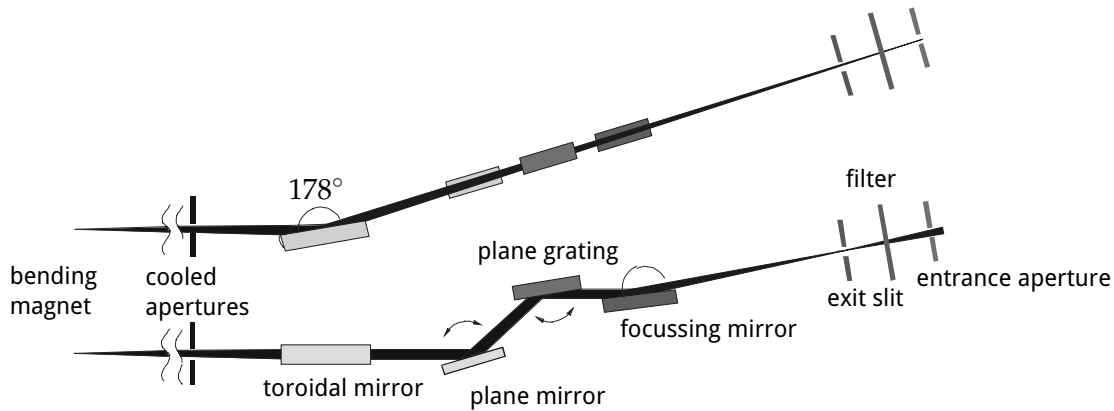


Figure 2.5 | Schematic setup of the SX700 beamline at BESSY II in top view (upper part) and side view (lower part)^a.

^a Original image taken from Scholze et al. [65]

horizontal slit at the exit slit. The achievable relative bandwidth depends on the size of this slit as well as on the selected wavelength. It varies between values of 0.5×10^{-3} and 2.5×10^{-3} relative bandwidth. As mentioned above, the monochromator grating disperses the incoming broad band radiation into the vertical direction with respect to the storage ring plane. The blaze of the grating ensures high grating efficiency of about X% in the first diffraction order, but the selected vertical part of the dispersed radiation still contains parts of higher diffraction orders. This leads to a diminished spectral purity, which reduces the energy resolution. For the purpose of suppression of these higher grating orders, thin metal films in transmission geometry acting as filters are installed close to the entrance aperture to the experimental station suppressing radiation energetically above the respective absorption edges of the material.

The SX700 beamline only has one focussing mirror per horizontal and vertical direction, which differs in position in the beamline and produces different focal points for the two directions. The focussing in horizontal direction (grating dispersion direction) is done through the toroidal mirror (cf. Fig. 2.5), which also serves as a collector mirror for both axis and parallizes the beam in vertical direction. The focal point is located in the exit slit to ensure high energy resolution. The vertical focussing is done by an additional focussing mirror after the monochromator grating with a focal point about 2 m behind the exit slit in propagation direction. Due to the large distance of the two focussing elements to the experimental station, a low divergence of the beam of about $1.6 \text{ mrad} \times 0.4 \text{ mrad}$ is achieved.

Table 2.1 | Beamline parameters of the two EUV beamlines EUVR and sx700 in comparison.

Parameter	SX700	EUVR
Wavelength range	0.7 nm to 24.8 nm	5 nm to 50 nm
Spot size (standard settings)	1 mm × 1 mm	0.1 mm × 0.1 mm to 2 mm × 2 mm
Beam divergence	1.6 mrad × 0.4 mrad	4 mrad × 4 mrad
Linear polarization (horizontal)	98 %	40 % to 98 %

The Extreme Ultraviolet Beamline EUVR

The general layout and operation principle of the EUVR beamline is identical to that of the SX700 beamline described in the previous paragraph with some differences in the focussing, which are described in the following. Due to the lower electron energy in the MLS storage ring, the spectrum of both beamlines differs with a spectral range shifted to longer wavelengths in the EUVR beamline with respect to the SX700 beamline. The wavelength range covered by the EUVR beamline is between 5 nm to 50 nm (corresponding to photon energies from approximately 25 eV to 248 eV). In contrast to the SX700 beamline, the foci for horizontal and vertical direction are both at the position of the exit slit with an additional refocussing mirror behind that slit. This increases the divergence of the beam to approximately 4 mrad in both directions, but together with the shifted bending magnet spectrum of the MLS allows higher photon flux through the larger aperture of the torodial mirror. The main properties of both beamlines and their differences are given in Table 2.1. The optics of both beamlines in comparison are shown in Fig. 2.6.

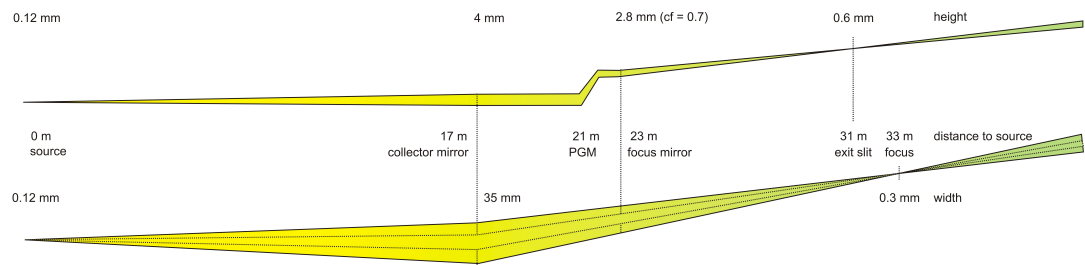
2.2.2 The Experimental Endstations at the EUVR and SX700 Beamlines

All experiments in the EUV spectral range within the framework of this thesis were conducted at the beamlines EUVR and SX700. Each of the beamlines is equipped with an experimental end station containing the detectors, mounts for charge coupled device (CCD) cameras and a goniometer to adjust the angle of the sample holder with respect to the beam. Due to the high absorption of the EUV radiation in air, both chambers need to be kept under high vacuum conditions, typically below the limit of 3×10^{-6} mbar.

The end stations differ in the size and weight of samples, which can be mounted on the sample holder. The large reflectometer at the EUVR beamline was designed with heavy and large samples in mind, whereas the ellipso-scatterometer at the SX700 beamline covers a larger angular range for both the detector and the sample holder. In the following the two different setups with their primary features are summarized.

EXPERIMENTAL SETUP AND SAMPLE SYSTEMS

a) SX700 beamline



b) EUVR beamline

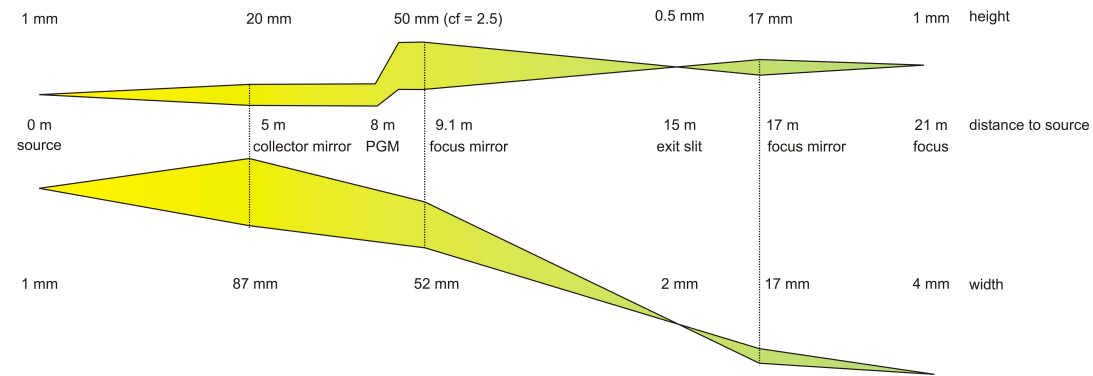


Figure 2.6 | Schematic optics of the SX700 and EUVR beamlines. The SX700 beamline has a small beam divergence due to the single focussing in both horizontal and vertical direction. The focal point positions differ by approximately 2 m. The EUVR beamline offers significantly higher photon flux due to the larger collector mirror aperture in conjunction with the bending magnet spectrum at the MLS. The beam spot sizes are variable and can be significantly smaller in comparison to the SX700 beamline at the position of the experiment due to refocussing.

The large reflectometer at the EUVR beamline

The large reflectometer serving as the end station at the EUVR beamline was designed for reflectometry and scatterometry measurements for samples with a weight of up to 50 kg and a maximum diameter of 550 mm in mind[77]. The available axis of movement and rotation are shown in Fig. 2.7. The sample holder plate allows for linear movement in all three orthogonal directions as well as angular rotations in three axis. The latter allows to measure samples, e.g. samples with an anisotropy, with radiation impinging from all directions, if the sample is mounted in the center position of the sample holder. The rotation around the Θ -axis covers the range from -7° to 90° relative to the incoming beam. Thus, enabling reflectometry and scatterometry normal incidence to grazing incidence angles together with the detector arm rotation around the 2Θ -axis from 0° to 180° . The distance of the detector to the sample is variable through the *Det-R* axis from a minimum value of 125 mm to 550 mm.

The detector mount is equipped with up to X diodes, which can be rotated to face either the sample or the incoming beam. The diodes used within the framework of this thesis are $4.5 \text{ mm} \times 4.5 \text{ mm}$ and, optionally $10 \text{ mm} \times 10 \text{ mm}$, GaAsP photodiodes. The detector holder can be moved along the Θ and 2Θ rotational axes, which allows to take measurements in the *out-of-plane** direction in s-polarization.

* The out-of-plane scattering direction refers to radiation scattered outside of the scattering plane spanned by the surface normal of the sample and the impinging beam direction.

The Instrumentation for the EUV Spectral Range

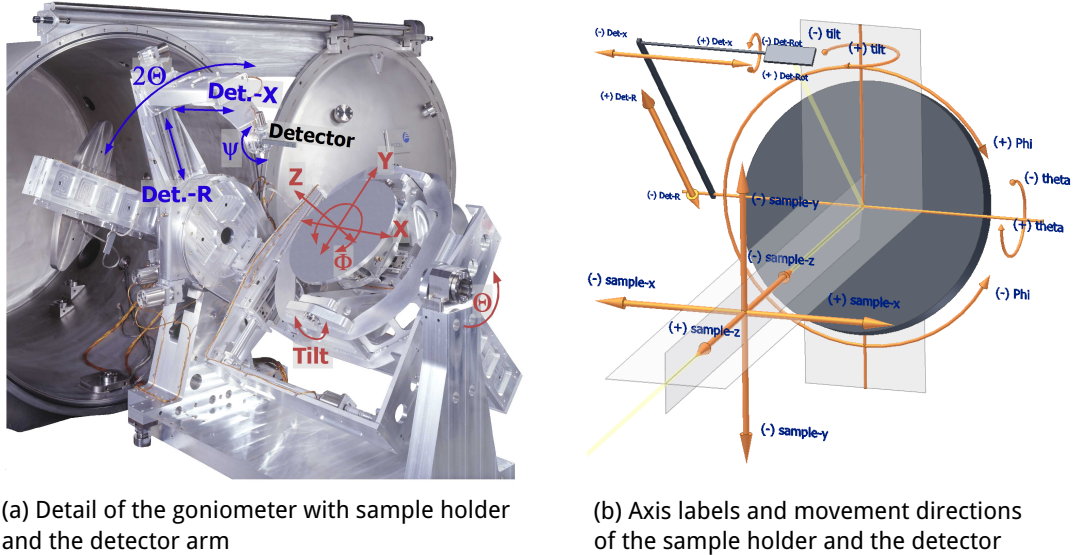


Figure 2.7 | The BigRef.

The Ellipso-scatterometer at the SX700 beamline

The ellipso-scatterometer is a reflectometer similar to the large reflectometer providing the end station for the SX700 beamline. Its capabilities differ from the large reflectometer by a wider reachable angular range for both the detector movement as well as the sample movement. The angular and linear movements and axes are shown in Fig. 2.8 together with a photograph of the goniometer and detector arm. In contrast to the large end

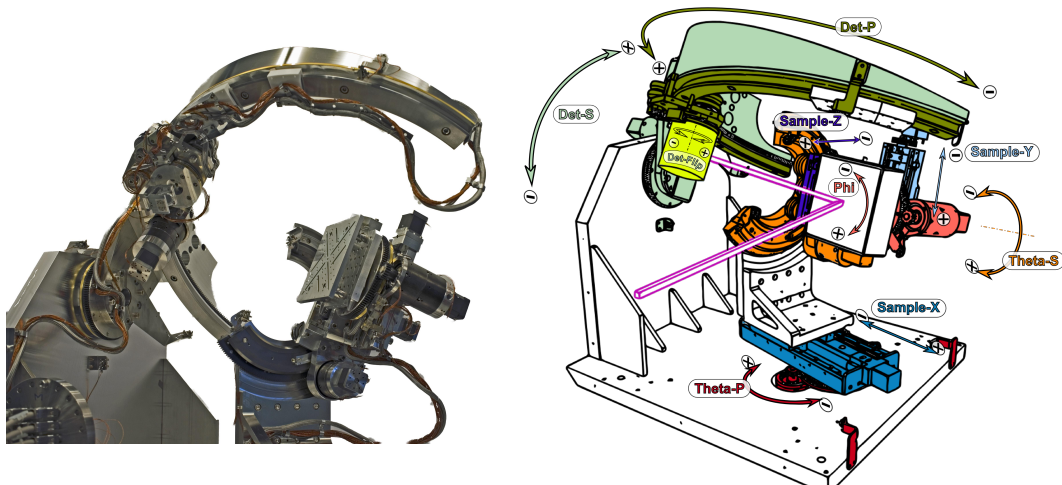


Figure 2.8 | The EUV ellipso-scatterometer.

station at the EUVR beamline, it can hold samples with a size of approximately 13.5 mm × 13.5 mm and a maximum of 5 kg in weight. However, the rotational movement of both

double check number

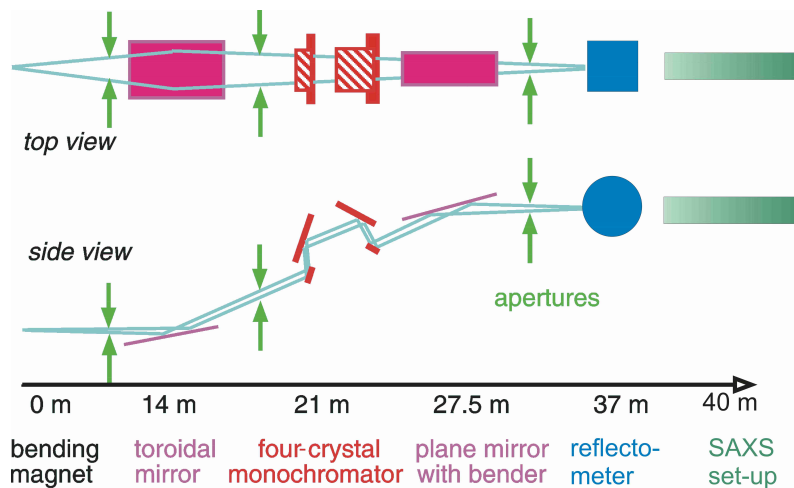
EXPERIMENTAL SETUP AND SAMPLE SYSTEMS

the detector and the sample holder allow for a larger angular range. In consequence, measurements in s-polarization and well as p-polarization can be conducted on the same sample. With the capability to mount a polarization analyzer at the detector holder, polarization resolved measurements are thus possible [71].

2.3 Grazing-incidence X-ray Fluorescence at the FCM Beamline

The grazing incidence X-ray fluorescence (GIXRF) measurements of the Cr/Sc sample systems were performed at the four crystal monochromator (FCM) bending magnet beamline [45] in the BESSY II laboratory. The necessary photon energies to excite the K-edge x-ray fluorescence of chromium and scandium, are well above the spectral range of the EUVR and SX700 beamlines in the order of several keV. The general setup and design of the FCM beamline is very similar to that of the SX700 beamline, with the exception of the four crystal monochromator, which replaces the plane grating monochromator in the x-ray spectral range. It offers tunable photon energies from 1.75 keV to 10.0 keV. A high energy resolution of $E/\Delta E = 10^4$ is attained by the convolution of four exchangeable crystal Bragg reflections. The monochromator can be equipped with two monochromator crystals. For the high energy range above approximately 3.5 keV to 10.0 keV silicon is used. In the lower energy range between 1.75 keV and 3.5 keV higher radiant power is available through the usage of a InSb crystal. A schematic overview of the FCM beamline can be found in Fig. 2.9.

Figure 2.9 | FCM beamline scheme.



The end station used for the GIXRF experiments is a specialized chamber for GIXRF, total reflection x-ray fluorescence (TXRF) and XRR [51] depicted in Fig. 2.10. It is equipped with a detector arm and a sample goniometer allowing to measure grazing incidence angles of 0° to 60° . The detector arm holds a diode allowing XRR measurements. Perpendicular to the beam direction, an energy dispersive silicon drift detector (SSD) is mounted close to the sample surface. It allows to detect fluorescence radiation emitted from the sample energetically resolved. The samples can be rotated with respect to the storage ring plane in order to allow a variable polarization impinging on the surface.

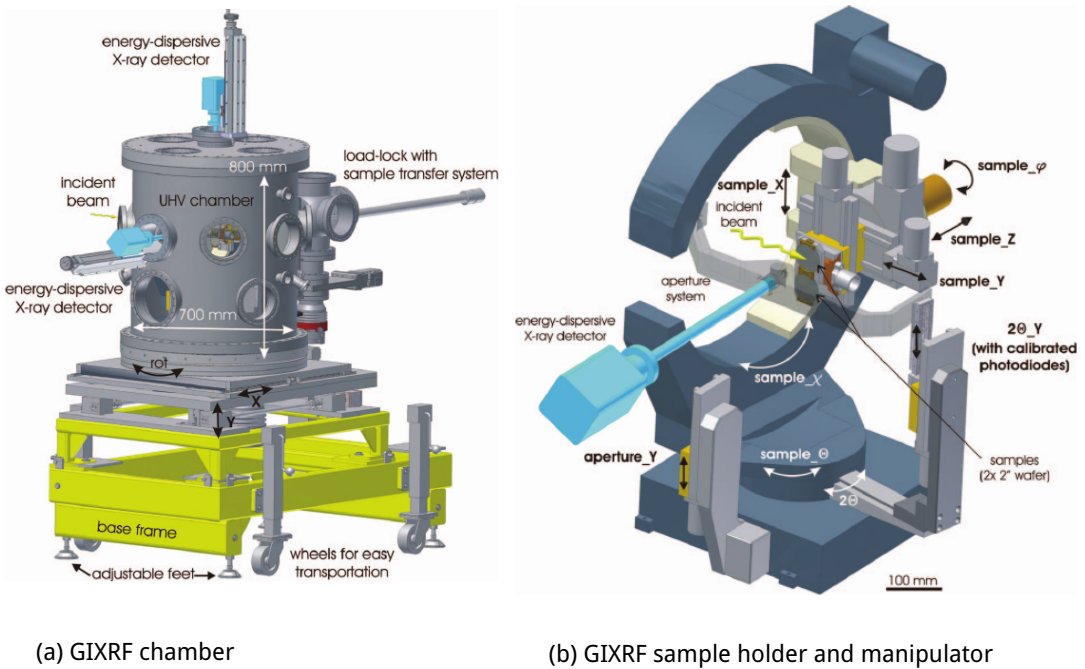


Figure 2.10 | The GIXRF chamber.

2.4 Sample systems

The samples studied in the framework of this thesis are designed to work as near-normal incidence mirrors for the EUV spectral range. The underlying principle of an artificial one dimensional Bragg crystal requires the deposition of thin layered systems with high periodicity and stability. The experiments presented here were conducted on two sets of sample types as prototypes of mirrors for two different spectral ranges. The theoretical description of the principle of multilayer mirrors in Sec. 1.3 of Ch. 1, optical contrast, i.e. a large as possible difference in the real part of the refractive index n , is required to achieve large reflectivities, while on the other hand maintaining a low absorption.

This thesis investigates systems designed to reflect radiation in two spectral ranges, the *water window* with wavelengths from 2.2 nm to 4.4 nm and the range from 12.4 nm to 14.0 nm with a wide range of applications, e.g. for the next-generation lithography. The choice of the chemical species for the multilayer systems, apart from trivial properties such as non-toxicity and solidity, is largely influenced by the electronic structure of the respective materials, since large changes in the refractive index, i.e. large optical contrast with respect to a second material, can be expected close to that resonances. The demand for low absorption also requires species, where the absorption edges are energetically higher or far lower than the desired spectral range of operation. For a well defined interface it is also necessary that the two materials are mostly inert and do not react with one another. The latter would potentially lead to inevitable intermixing and thus a loss of a sharply defined interface.

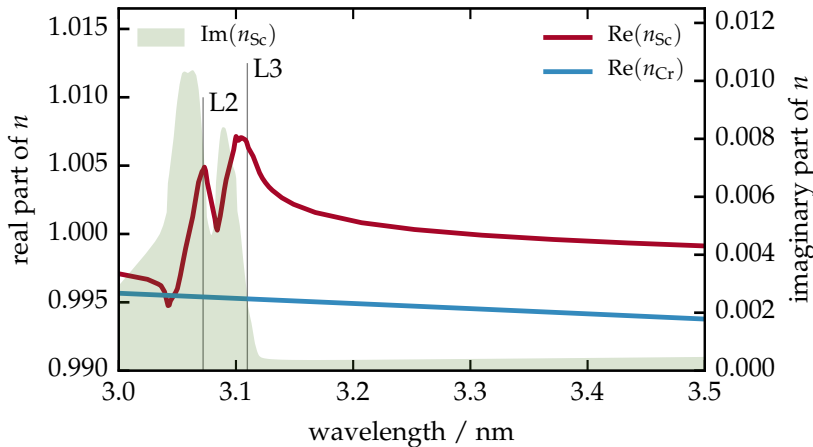
2.4.1 Choice of the Chemical Species and Multilayer Design

tion spacer material
and optically active
material

Cr/Sc multilayer system

In case of the water window spectral range, we investigated samples designed for a peak reflectance at a wavelength closely above 3.14 nm, where the L₃ edge of scandium (Sc) is found. Fig. 2.11 shows the refractive index of Sc and the second material chromium (Cr) in the water window spectral range. The periodic multilayer of the systems investigated

Figure 2.11 | Refractive indices of Cr and Sc with the water window spectral range. The marked absorption edges are the L₂ and L₃ edge of Sc. The imaginary part of the refractive index accounts for the absorption and is shown for Sc. Above the L₃ edge is the highest contrast for the two materials providing the highest potential reflectivity in a periodic multilayer arrangement.



here, were therefore binary alternating layers of Cr and Sc. The required nominal period thickness D , i.e. the thickness each periodically repeated layer stack, for the design goal of a peak reflectivity at $\lambda = 3.14$ nm is $D = 1.573$ nm with a layer thickness ratio of $\Gamma = 0.5$ of both materials. To protect the Sc layers from oxidation, an additional capping layer Cr of approximately $d_{\text{cap}} = 3$ nm was added as the surface layer. The binary layer stack was repeated $N = 400$ times per bilayer.

The Cr/Sc multilayer sample was prepared at the DESY X-ray multilayer laboratory by DC magnetron sputtering. The deposition was performed at 0.133 Pa ultrahigh purity Ar (99.999%) and a power of 200 W for both Sc and Cr sputtering targets. The multilayer is composed of alternating layers of Cr and Sc with periodic replication of the bilayer stack by $N = 400$ times. The substrate is a superpolished Si wafer piece. The sample dimensions measure approximately (20×20) mm². More details can be found elsewhere [62]. The multilayer mirror was designed to reflect radiation in the water window energetically, just below the Sc L edge, close to a 3.1 nm wavelength at an angle of incidence (AOI) of $\alpha_i = 88.5^\circ$.

Mo/Si multilayer systems

The second set of systems under investigation in this thesis is composed out of 50 to 65 bilayers Molymdenum (Mo) and Silicon (Si). Both materials show a very low absorption in the range from 12.4 nm to 14.0 nm, with the Si L₂ edge forming the lower wavelength limit for the usage as a mirror system in this combination. The respective refractive indices are given in Fig. 2.12.

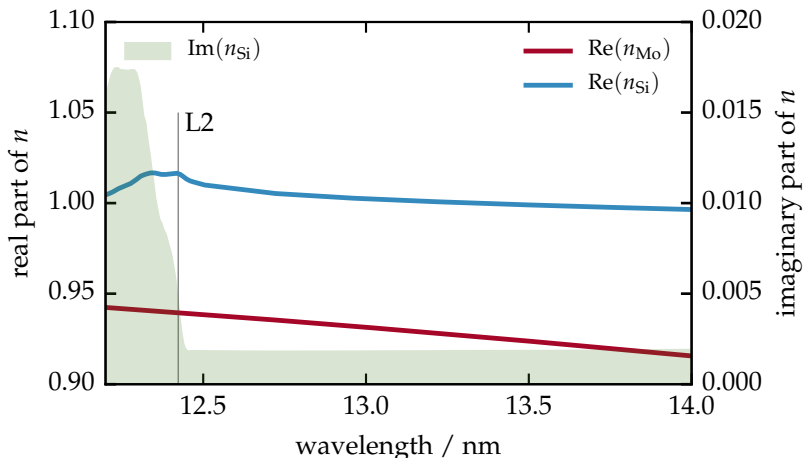


Figure 2.12 | Refractive indices of Mo and Si in the wavelength range from 12.4 nm to 14.0 nm. The L₂ absorption edge of Si marks the lower wavelength limit for the applicability of this material combination in multilayer mirror systems.

Finally, the sample systems can contain additional materials, which serve as barrier layers. The two species used for our samples are Boroncarbide (B_4C) and Carbon (C). Those two materials do not have any absorption edges in the given relevant spectral range and additionally show low contrast to the respective spacer materials Si and Cr. The details of the respective sample layouts are discussed in the respective sections of the following chapters.

2.4.2 Multilayer Deposition by Magnetron Sputtering

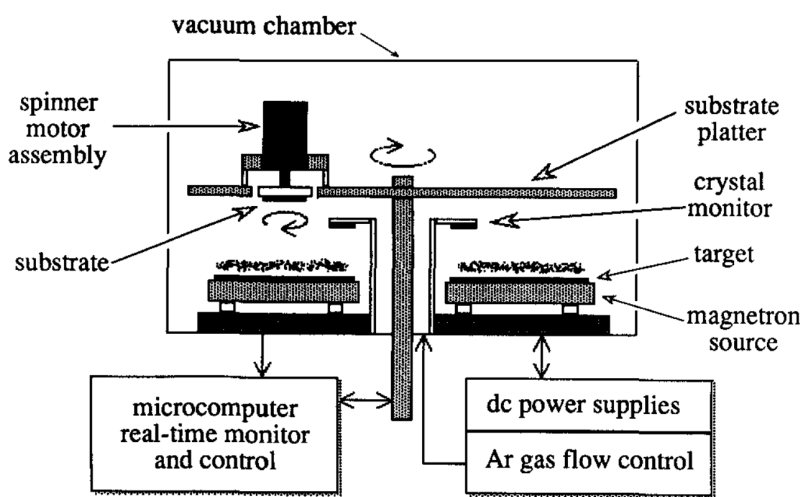
The multilayer samples investigated here were fabricated by the DC magnetron sputtering technique [74] by two different multilayer and optics groups. The Mo/Si multilayer samples were fabricated by Stefan Braun at the Fraunhofer IWS, Dresden, Germany and the Cr/Sc samples are by Saša Bajt from the Optics Group at CFEL, DESY, Hamburg in Germany.

Magnetron sputtering is a physical vapor deposition technique. A vacuum chamber is equipped with a substrate to be coated, in our case silicon, and one or more sputter targets. Depending on the intended design of the multilayer to be deposited, those targets are the respective materials, which later form the individual layers. In the DC magnetron sputtering system, a strong electric field is applied between the substrate and the sputter targets. The vacuum chamber containing those parts is then filled with a sputter gas, typically ultrapure Ar gas (99.999 %), with partial pressures in the range from 10^{-3} mbar to 10^{-2} mbar [74]. The strong electric field ionizes the sputter gas causing the ions to be accelerated towards the sputter targets (cathode) and form a charged plasma. Upon impact in the target, atoms and electrons of the condensed matter phase of the respective material are released and travel towards the substrate. The released atoms condense there, forming bonds and creating a slowly growing layer. The thickness of the layer can be fine tuned through the deposition time. The additionally released electrons, while being accelerated towards the substrate (anode), collide with the sputter gas atoms and

EXPERIMENTAL SETUP AND SAMPLE SYSTEMS

cause further ionization. In order to avoid damage of the forming layer at the substrate, strong magnetic fields are applied to the sputter targets. This confines the movement of the charged particles (the plasma) sputter gas ions and electrons to the region close to the target surface. Thereby, increasing the collision (ionization) probability of electrons and the gas atoms through the helical movement in the magnetic field while keeping those particles away from the substrate. To ensure homogeneous layer deposition, the substrate is kept under permanent rotation. A schematic DC magnetron sputtering system is depicted in Fig. 2.13.

Figure 2.13 | Schematic setup for magnetron sputtering.



For both samples, silicon serves as the substrates for the deposition process. The surfaces are super polished with mechanical polishing methods to reduce any prior surface roughness. The sample size and shape differ for the systems investigated. In case of the Mo/Si mirror samples, wafer pieces of approximately 20 mm × 20 mm (photograph shown in Fig. 2.14) and round substrates with approximately 20 mm in diameter were used. In case of the Cr/Sc systems, wafer pieces of varying size but approximately

Figure 2.14 | Mo/Si multilayer sample.



10 mm × 20 mm served as the substrate.

GENERAL:

- 1.) Du redest immer wieder von "high reflective Mo/Si ML Mirror
for the metal rays 12,9 - 14 nm .."
Das ist Falsch \Rightarrow Das waren Breitband spiegel) high reflective in bei 13,5 nm

3

Characterization of the Multilayer Structure for Different Systems

The multilayer mirror samples we shall investigate here were fabricated using the magnetron sputtering technique briefly discussed in the chapter 2 with nominal layer thicknesses and chemical species, depending on the desired reflection angle and spectral range. Among other parameters of the production process, the achieved layer thickness and sharpness of the interfaces has a direct impact on the performance of these mirrors with respect to their peak reflectance and bandwidth. Although the sputtering process is a well established technique for mirror fabrication, the actual layer thicknesses in the sample may differ from the nominal values and are generally unknown.

Based on the matrix algorithm introduced in chapter 1, the electromagnetic fields inside and outside an arbitrary layer system can be calculated. Most importantly, this allows to calculate the expected specular reflectance curves across angular or spectral ranges for a given layer model. The comparison of these calculated curves to measured data thus allows to obtain information about the actual layer properties in a given sample.

However, the detected reflectance values in a specular reflection experiment are merely intensities of reflected radiation. The information on the phase of the electromagnetic wave can not be obtained in this way and is lost. It is thus not possible to directly reconstruct the layout of the sample with the measured reflection curve. This is known as the inverse problem of scatterometry. Reconstructing the layer properties is therefore an attempt of solving this inverse problem by accumulating prior knowledge about the sample, such as the nominal design goals during the fabrication process, into a model of that system. Starting from this model, the theoretically calculated curve is compared to the measured reflectance and optimized iteratively.

This method is not limited to the optimization of the model with respect to the reflectance of the mirror samples in their designated EUV spectral range. In order to add complementary information for refining the solution of the inverse problem, additional methods can be applied. In this chapter, depending on the sample system, we analyze several experimental methods. Apart from the aforementioned reflectance in the EUV spectral range, we apply resonant EUV reflectance across absorption edges, XRR

"with different sensitivities" oder so ..

morphology

individual

A

Ohne die Probe am zerstören

zusammenziehen
Der Satz ist relativ
würde ich mit dem
2. Satz

versimilär

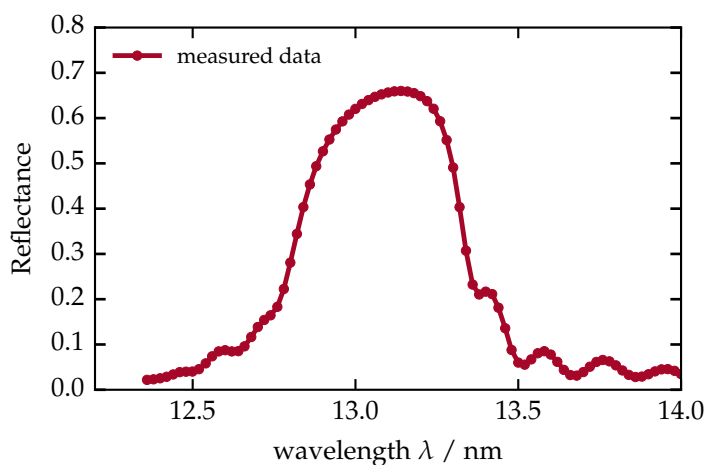
with high photon energy and finally XRF. The latter does rely on the measurement of fluorescence radiation and thus requires the calculation of the field intensities inside the layer stack at the position of a specific chemical species for its analysis as described in section 1.5 of chapter 1.

3.1 Reconstruction Based on Specular EUV reflectance

In this section we demonstrate the reconstruction of a multilayer system designed as near-normal incidence mirror for the wavelength range between 12.4 nm and 14.0 nm based solely on experimental data of EUV reflectivity. The mirror was designed to achieve a peak in the reflectance at a wavelength of $\lambda = 13.5$ nm for an angle of incidence of $\alpha_i = 6^\circ$. That combination is of relevance for optical setups in the next generation lithography ~~setups~~ for the semiconductor industry, for which this sample served as a prototype. The multilayer coating was deposited on a polished silicon substrate. The sample contains a periodic layer stack of molybdenum (Mo) and silicon (Si). Due to the problem of intermixing and resulting loss of interface definition, additional barrier layers of boroncarbide (B_4C) and carbon (C) were included at the Mo to Si and Si to Mo interfaces, respectively. We shall therefore refer to this sample with the layer sequence within one period from bottom to top as Mo/ B_4C /Si/C. The periodicity of that system is $N = 65$, while the 65th (capping) layer period does not possess a carbon layer but terminates with the silicon layer. A detailed schematic figure of the layer layout can be found in the description of the corresponding theoretical model in Fig. 3.2 below.

The sample was measured with respect to its reflectivity across the spectral range mentioned above at an angle of incidence of $\alpha_i = 15^\circ$ from the surface normal. The measurement was conducted at the EUVR beamline at the MLS. The reflectivity was evaluated by first measuring the direct beam in the reflectometer with the diode detector. Then, the reflected radiation at a detector angle of 30° was measured in reference to the direct beam signal. To ensure the stability of the result, the direct beam was measured again afterwards and compared to the data of the first measurement. The normalized results are shown in Fig. 3.1. The measurement uncertainty in with this experimental method is within 1 % of the peak reflectance value. Consequently, the error margin is within the line thickness of the data presentation in Fig. 3.1.

Figure 3.1 | Spectrally resolved reflectance data of the Mo/ B_4C /Si/C multilayer sample. The irradiation was conducted under a fixed angle of incidence $\alpha_i = 15.0^\circ$. The measurement uncertainty is within the line thickness of the plot.



The reflectivity curve shows a broad peak attaining its maximum value at a wavelength of approximately 13.1 nm, which is lower than the design peak reflectance of 13.5 nm.

with magnetron sputtering?

photo

That is due to the different angle of incidence used in the experiment. Apart from the main peak, side fringes are visible. They originate due to a superposition of waves being reflected at the top surface and the substrate interface. They are thus directly related to the total thickness of the multilayer coating and well known as *Kiessig fringes* [44]. Based on the data obtained through this spectrally resolved reflectivity experiment, we shall attempt to reconstruct the unknown layer layout in the following sections. The nominal fabrication parameters serve as an anchor point for the analysis to construct a reasonable model for the reconstruction.

The reconstruction of a given model based on the evaluation of EUV (or XRR) reflectivity data is a well established method for the characterization of multilayer systems widely used today [4, 17, 49]. In most cases a model is constructed and optimized applying gradient methods such as the Levenberg-Marquardt method [48, 53]. Those optimization algorithms typically operate with a set of start parameters within the parameter space and iteratively improve the overlap of the prediction from the theoretical calculation and the experimental data. This is done by calculating the gradient of a minimization functional, usually termed χ^2 , in all directions in the parameter space and changing the parameters accordingly in direction of smaller χ^2 values. This approach has the major disadvantage that the end result is strongly dependent on the choice of starting values and may not represent a global minimum of χ^2 but only a local optimum. While estimations of the quality of the fit results within the (local) optimum are possible, no estimation can be given globally for the given model. For those reasons, this characterization strategy has only limited applicability and alternative approaches are required.

In contrast to those gradient methods, statistical optimization algorithms exist. They share the aim of minimizing a optimization functional χ^2 with the gradient approaches, but operate on the whole parameter space with predefined limits instead. In the following we shall apply those statistical optimization routines to obtain the reconstruction of the Mo/B₄C/Si/C sample and elaborate their application to the characterization of multilayer systems in detail.

Ich denke die Erklärung ist zu weit

A

heuristic

3.1.1 Multilayer Model and Particle Swarm Optimization

For the purpose of reconstructing the layer layout of the Mo/B₄C/Si/C sample, a parameterized model is needed entering the theoretical calculations to obtain the reflectivity curve according to the matrix algorithm. The model is largely based on prior knowledge available from the fabrication process. For the multilayer sample investigated here, the nominal layer design is known and a schematic representation is shown in Fig. 3.2. As introduced above, the multilayer coating consists of a periodic arrangement of four layers replicated 64 times. With the top period being different from the others through the missing carbon interdiffusion layer on the top surface. Since the sample was exposed to ambient conditions, a passivation of the top silicon surface through oxidation has to be taken into account through a silicondioxide layer. The parameterization of that model is given by the thicknesses of each layer within one period as well as for the capping silicondioxide layer. Each of the deposited layers may vary in density with respect to the bulk density of that material [17], which also needs to be reflected in the model. Finally, the Nevot-Croce factor σ accounting for roughness and interdiffusion at the interfaces as introduced in chapter 1 is also included. The required optical constants, i.e. the indices of refraction, of the respective materials in the relevant spectral range are taken from tabulated values by Henke et al. [39] and used for the theoretical calculations

CHARACTERIZATION OF THE MULTILAYER STRUCTURE FOR DIFFERENT SYSTEMS

Figure 3.2 | Model of the multilayer stack including the substrate and the capping layers. The periodic part is enclosed between the dashed lines with four layers in each period repeated $N = 64$ times. The capping period does not include an interdiffusion layer but has a natural SiO_2 layer.

Select the natural oxidation due siO₂ layer

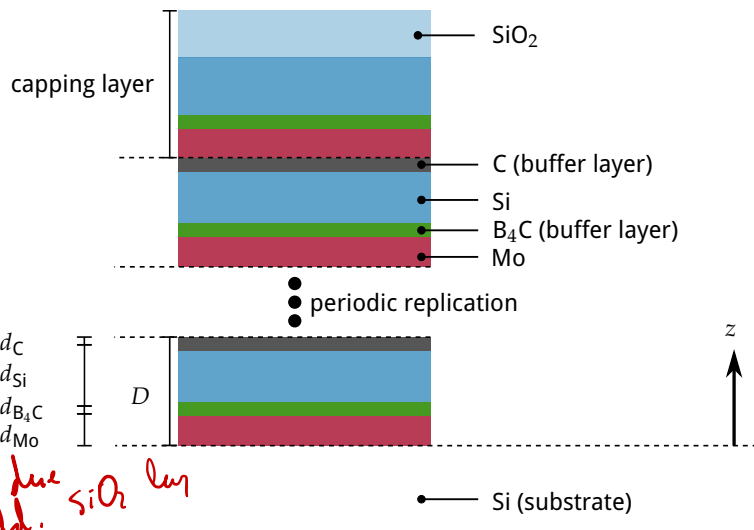


Table 3.1 | Multilayer parametrization and parameter limits

Parameter	Definition	Lower bound	Upper bound
$d_{\text{Mo}} / \text{nm}$	Mo layer thickness	0.0	7.0
$d_{\text{Si}} / \text{nm}$	Si layer thickness	0.0	7.0
d_{C} / nm	C buffer layer thickness	0.0	5.0
$d_{\text{B}_4\text{C}} / \text{nm}$	B_4C buffer layer thickness	0.0	5.0
σ / nm	Nérot-Croce parameter (identical for all interfaces)	0.0	2.0
ρ_{Mo}	Mo density w.r.t. bulk density	0.5	1.0
ρ_{Si}	Si density w.r.t. bulk density	0.5	1.0
ρ_{C}	C density w.r.t. bulk density	0.5	1.0
$\rho_{\text{B}_4\text{C}}$	B_4C density w.r.t. bulk density	0.5	1.0
Capping layer			
$d_{\text{SiO}_2(\text{cap})} / \text{nm}$	SiO ₂ capping layer thickness	0.0	5.0
$\rho_{\text{SiO}_2(\text{cap})}$	$= \rho_{\text{Si}}$ (identical to Si density)		

based on the matrix algorithm. A full list of the model parameters for the multilayer sample can be found in table 3.1 together with physically plausible limits for each of the parameters. Due to the fact that the EUV reflectivity curve shown in Fig. 3.1 shows the first order Bragg peak of the layer system, none of the layers can be thicker than 7 nm, i.e. in the order of half of the wavelength. The barrier layers were designed to attain thicknesses below 1 nm. The densities of the various materials within this model was constrained to values between 50 % and 100 % with respect to their bulk density, while values above the bulk density are physically highly improbable. Due to the high peak reflectance of the multilayer sample in the EUV measurement, the maximum value of the Nevot-Croce factor was limited to be below $\sigma \leq 2 \text{ nm}$. With its upper limit, the measured peak reflectance can not be attained within this model thus not limiting the generality.

würde ich etwas abschwächen

close to the theoretical limit

The minimization functional and particle swarm optimization

As introduced above, the reconstruction of the model for the multilayer is an optimization problem. Based on the measured reflectivity data an optimization functional defines the goodness of the model with respect to the measured data. The quality is asserted based on the method of least squares [9, 30, 47] and the functional is defined as the reduced $\tilde{\chi}^2$

$$\tilde{\chi}^2 = \frac{1}{M - P} \left[\sum_m \frac{(I_m^{\text{model}} - I_m^{\text{meas}})^2}{\tilde{\sigma}_m^2} \right], \quad (3.1)$$

where M is the number of measurement points, P is the number of parameters used in the model, I_m^{model} is the calculated intensity for the corresponding measurement point with index m having the measured intensity I_m^{meas} . The calculated intensity fur the EUV reflectivity curve above I_m^{model} follows directly from the matrix algorithm and the quantity R in Eq. (1.28) in chapter 1. Each point is calculated based on the angle of incidence and wavelength associated with measurement point m . The experimental error for each measurement point is described by $\tilde{\sigma}_m$.

PTB :)

For the minimization of the functional in Eq. (3.1) we apply a global optimization algorithm known as PSO [43]. In contrast to the aforementioned gradient based methods, the particle swarm optimizer operates on the whole parameter space as defined by the upper and lower parameter limits, which are given in table 3.1 for the particular example here, without specific starting parameters influencing the convergence result. We implemented the PSO algorithm based on the draft by Carlisle and Dozier [18]. The basic mechanism of the algorithm is the definition of a swarm of individual particles, which are initialized randomly distributed across the allowed parameter space. Initially, each of those particles calculates the minimization functional at its random position retaining that result. In an iterative process, the global best solution ("social component") found as well as the individual best solution ("cognitive component") of each particle are used to calculate a velocity vector within the parameter space for each particle. Within that iteration each of the particle thus moves to a new position, where the minimization functional is again evaluated and compared the the individual and global best solutions. If a better value is found, the respective retained results are updated with the new value and the next iteration is performed. While following that process the particles eventually converge to the global best solution, which may or may not be the global best optimum of the whole optimization problem. Due to the combination of social and cognitive component, fast convergence into a local optimum can be avoided. The state of full convergence is reached, when either all particles occupy the same place in the parameter space or if stagnation is reached. Due to the statistical nature of the algorithm, convergence can not be guaranteed. Neither is the global best optimum found necessarily the global minimum. The result may be verified by repeated application of the algorithm or simply by reaching a satisfactory solution through comparison of the measured and calculated curves and thus the desired small $\tilde{\chi}^2$ values.

start speed?

weighted

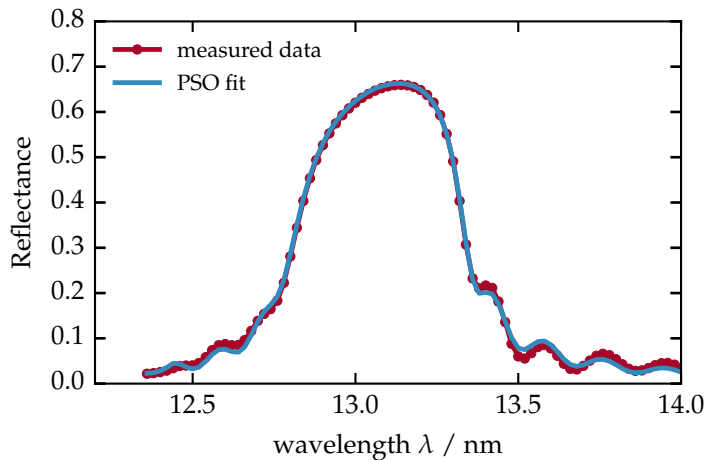
Vorsicht: Konvergenz ist garantiert
→ Du meinst

A

Model reconstruction based on the EUV reflectivity data

We have applied this optimization procedure to the Mo/B₄C/Si/C sample and the measured EUV reflectivity curve. The fit result is shown together with the measured data in Fig. 3.3. The parameter results are listed in table 3.2. The solution does indeed provide

Figure 3.3 | Theoretical reflectance curve based on the optimal model parameters obtained from the particle swarm optimization.



a very good agreement with the measured data. However, by repeated evaluation of the PSO procedure, significantly different results for the optimal parameter set with comparable agreement were found. Clearly, this is no desirable situation, since no definite answer of the actual thicknesses found in the sample can be made. To complete the characterization additional methods of model verification are thus required. We shall therefore discuss an additional approach to the optimization problem in the following section on how the model validity and the information content of the measured data can be asserted based on the example of the PSO results obtained here.

Table 3.2 | Results for the optimized parameters based on the PSO of the EUV reflectivity for the Mo/B₄C/Si/C sample.

Parameter	Definition	PSO result
$d_{\text{SiO}_2(\text{cap})}$ / nm	SiO ₂ capping layer thickness	3.194
d_{Mo} / nm	Mo layer thickness	2.460
d_{Si} / nm	Si layer thickness	2.421
d_{C} / nm	C buffer layer thickness	0.811
$d_{\text{B}_4\text{C}}$ / nm	B ₄ C buffer layer thickness	1.308
σ / nm	Névot-Croce parameter	0.322
ρ_{Mo}	Mo density w.r.t. bulk density	0.989
ρ_{Si}	Si density w.r.t. bulk density	0.883
ρ_{C}	C density w.r.t. bulk density	0.833
$\rho_{\text{B}_4\text{C}}$	B ₄ C density w.r.t. bulk density	0.909

same X? ↗

3.1.2 The Problem of Model Uniqueness and Maximum Likelihood Estimation

With the ambiguous reconstruction result of the previous section, the demand for a verification of the model with respect to the measured data becomes apparent. To clarify the problem of uniqueness of the solution, it is instructive to investigate the influence of the individual model parameters on the theoretical reflectivity curve. In Fig. 3.4 we varied a subset of the parameters starting from the PSO solution from Sec. 3.1.1. In each of the subfigures, one parameter or a quotient of parameters is varied while all others are kept fixed. By comparison of Fig. 3.4a, 3.4b, 3.4c and 3.4e it becomes clear

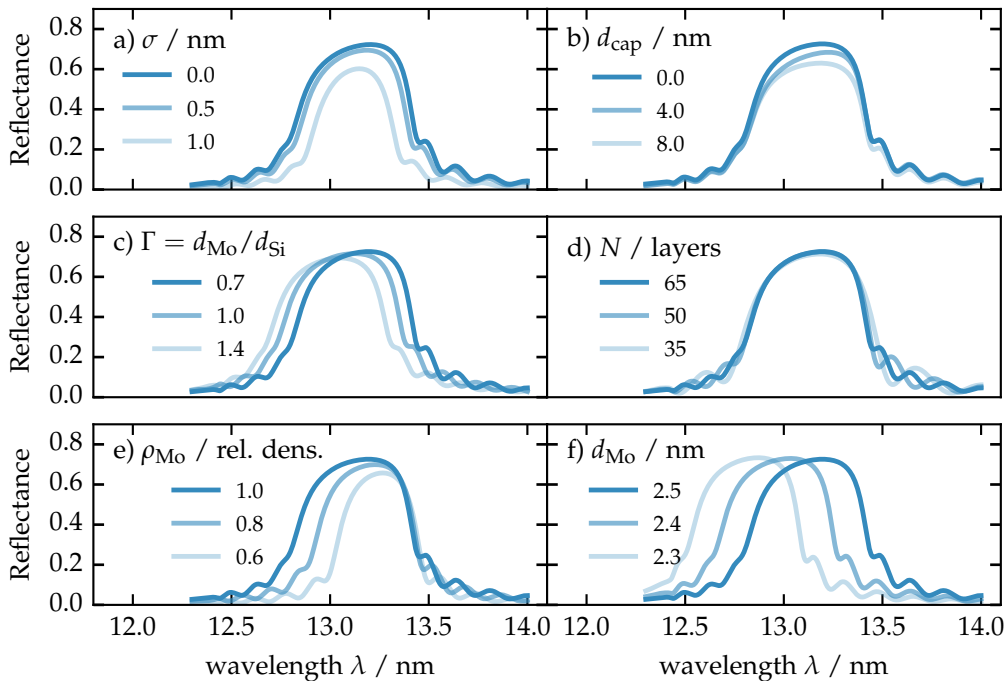


Figure 3.4 | Parameter influence. ;)

that a reduction of the peak reflectivity can originate in either a large roughness and interdiffusion parameter σ or similarly from the thickness of the capping layer, the silicon to molybdenum layer thickness ratio of the molybdenum density. A reconstruction based on a single EUV reflectivity therefore intrinsically produces a highly ambiguous result with strong parameter correlations. The available data, a single EUV reflectivity curve in this case, does not allow for a unique set of parameters of the model minimizing the χ^2 functional. In reality multiple solutions with equal values for $\tilde{\chi}^2$ exist. Clearly, this raises the question of how accurately a reconstruction may be achieved here and requires to determine the value of $\tilde{\chi}^2$ in vicinity of the PSO solution or possibly the whole parameter space.

Maximum likelihood

We approach this problem of evaluating $\tilde{\chi}^2$ across the parameter space by numerically sampling the functional based on a MCMC method [33]. An application of this technique to the design process of multilayer mirrors has been demonstrated by Hobson and Baldwin [40]. In our case, the match of model and experimental result is evaluated based on a non-centered χ^2 distribution assuming independent measurements. We further assume that any measured point is distributed around the actual reflectivity curve following a Gaussian distribution, i.e. we assume Gaussian errors for the experiment. The corresponding probability density function for a measurement result matching with the actual reflectivity curve, which is assumed to be obtainable exactly through the theoretical calculation, is then of Gaussian form [1]. Thus, the likelihood that the measured values match with the theoretical curve under the assumption that the model is correct is proportional to

$$L(E|M(\vec{x})) \propto \exp(-\tilde{\chi}^2(\vec{x})/2), \quad (3.2)$$

where E denotes the experiment, i.e. the measured data and $M(\vec{x})$ represents the model given through parameter set \vec{x} , e.g. the parameters of the model in table 3.1. In our case however, we seek to evaluate the likelihood $L(M(\vec{x})|E)$ that the model $M(\vec{x})$ with a given set of parameters \vec{x} is valid assuming the experiment E yields the correct curve (the so called “posterior distribution”). Those two quantities are linked through the Bayesian theorem [6, 55] stating

$$L(M(\vec{x})|E) \propto L(E|M(\vec{x}))L(M(\vec{x})), \quad (3.3)$$

where $L(M(\vec{x}))$ denotes the likelihood for the model to be valid for a specific set of parameters \vec{x} (the so called “prior distribution”). The prior distribution does contain any prior knowledge about the model and allowed parameters. For the example of the model parameters in table 3.1, the prior distribution is $L(M(\vec{x})) \rightarrow -\infty$ for any parameter set outside the listed boundaries and $L(M(\vec{x})) = 1$ everywhere else. In addition, we limit the maximum total period thickness, i.e. the sum of all layers in one period to only allow the appearance of the first Bragg peak within the measured spectral range through the same condition. Combining Eq. (3.2) and Eq. (3.3) then yields the likelihood functional

$$L(\vec{x}) = L(M(\vec{x})|E) \propto \exp(-\tilde{\chi}^2(\vec{x})/2)L(M(\vec{x})). \quad (3.4)$$

Solving the optimization problem posed in the previous section within this context is then, equivalently to the minimization of $\tilde{\chi}^2$, the maximization of the likelihood $L(\vec{x})$. The MCMC method poses a statistical approach on evaluating (mapping) the likelihood across the parameter space within the previously defined limits as in the PSO approach. It thus yields an alternative method on solving the optimization problem by extracting the maximum likelihood from the final result. However, in addition to the maximum value, the likelihood distribution in parameter space is obtained allowing to extract confidence intervals for each of the parameters [19]. Thereby, the aforementioned ambiguity of solutions can be quantified within the defined model and the available experimental data. The confidence intervals are defined as the one- or two-sigma standard deviations of the respective distributions for each parameter.

Confidence intervals for the Mo/B₄C/Si/C sample

We have applied an existing implementation of the MCMC algorithm by Foreman-Mackey et al. [29] to the EUV measurement of the Mo/B₄C/Si/C sample in Fig. 3.1 with the model in Fig. 3.2. The likelihood, as defined in Eq. (3.4) with the χ^2 functional from Eq. (3.1) is sampled in a high-dimensional space depending on the number of parameters in the model. We therefore need to project the distribution for each parameter by marginalizing over all other parameters. Alternatively, two-parameter correlations can be visualized by projecting on a two-dimensional area, again marginalizing across all other parameters. The projection for the Si and Mo layer thicknesses are shown in Fig. 3.5b and 3.5c. In both cases, a well defined distribution is obtained. In the two-dimensional projection in Fig. 3.5a, no correlations are apparent and a two-dimensional Gaussian-like shape results.

In all cases, the one-sigma standard deviations for Gaussian distributions are shown

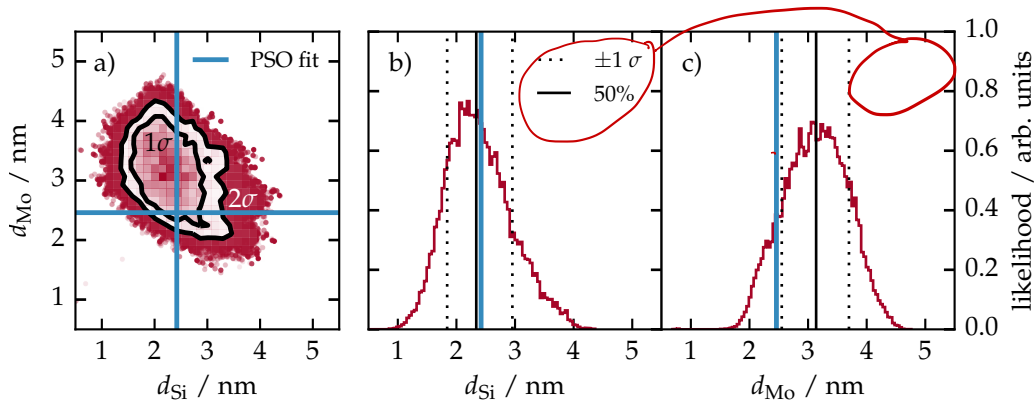


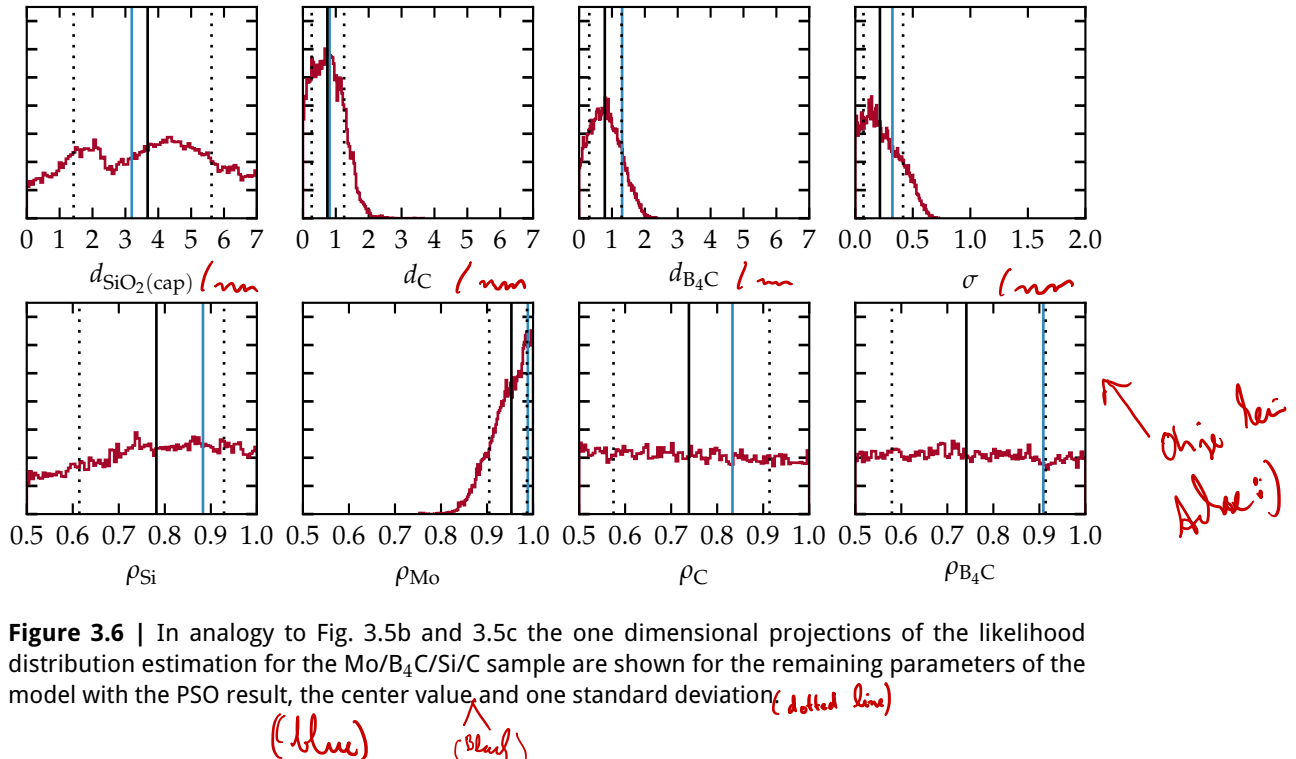
Figure 3.5 | Results of the maximum likelihood estimation obtained via the MCMC procedure. a) Two dimensional projection of the likelihood distribution for the parameter pair d_{Si} and d_{Mo} . The projection was obtained by marginalizing over all other parameters of the model. The black contours indicate the areas for one and two standard deviations (one and two sigma contours). The blue lines in all three sub-figures indicate the best parameter set found with the PSO method. b) One dimensional projection of the likelihood distribution for the silicon layer thickness d_{Si} . The solid black line marks the center position (50% percentile) of the distribution. The dotted lines are the limits of one standard deviation. c) The one dimensional distribution similarly to b) for the molybdenum layer thickness.

together with the weighted center, i.e. the 50th percentile. The PSO result is also indicated, which is compatible with the one sigma standard deviation, but does not match the center of the likelihood result. The reason for that lies in higher order correlations of the parameters. In Fig. 3.6, all one-dimensional projections of the likelihood distribution are shown for all remaining parameters. Clearly, while a reasonably small confidence interval (again, one standard deviation for all distributions) can be found for the thickness of the carbon and boroncarbide layers, the off-center value for the silicon thickness of the PSO result in Fig. 3.5c is compensated by a larger than center value for the boroncarbide layer in Fig. 3.6. Thus, the thicknesses are correlated and are no independent model parameters. Nevertheless, confidence intervals can be obtained within the given model and the given prior (the boundaries listed in table 3.1) and are listed accordingly in table 3.3 for one and two standard deviations. Within the allowed boundaries, some parameters remain entirely undefined with equal likelihood for any parameter value, such as the SiO₂ capping layer thickness, the silicon, carbon and boroncarbide relative densities. Their corresponding total confidence intervals thus cover almost exactly 68.2% (one standard deviation) and 95.4% (two standard deviations) of the allowed respective

11

? A

CHARACTERIZATION OF THE MULTILAYER STRUCTURE FOR DIFFERENT SYSTEMS



parameter range. Hence, with respect to the model defined and the measured EUV reflectivity curve, no reliable value for those sample properties can be reconstructed.

Table 3.3 | MCMC results obtained by the analysis of the EUV reflectivity for the Mo/B₄C/Si/C sample. The center values (50% percentile) together with confidence intervals (c.i.) of one and two standard deviations are shown.

Parameter	PSO result	center value with 1 σ c.i.	center value with 2 σ c.i.
$d_{\text{SiO}_2(\text{cap})}$ / nm	3.194	3.677(-2.252/+1.944)	3.677(-3.407/+3.108)
d_{Mo} / nm	2.460	3.137(-0.587/+0.560)	3.137(-1.054/+1.016)
d_{Si} / nm	2.421	2.338(-0.497/+0.616)	2.338(-0.916/+1.294)
d_{C} / nm	0.811	0.744(-0.477/+0.510)	0.744(-0.696/+0.971)
$d_{\text{B}_4\text{C}}$ / nm	1.308	0.782(-0.471/+0.511)	0.782(-0.722/+0.973)
σ / nm	0.322	0.214(-0.143/+0.201)	0.214(-0.204/+0.347)
ρ_{Mo}	0.989	0.953(-0.048/+0.034)	0.953(-0.094/+0.045)
ρ_{Si}	0.883	0.782(-0.167/+0.147)	0.782(-0.264/+0.208)
ρ_{C}	0.833	0.739(-0.164/+0.175)	0.739(-0.228/+0.249)
$\rho_{\text{B}_4\text{C}}$	0.909	0.741(-0.162/+0.172)	0.741(-0.230/+0.247)

It should be noted, that although the aforementioned density values can not be determined based on the available data, they remain possibly highly correlated parameters. A valid optimization result can therefore only be obtained by either applying the PSO routine or by iterative application of the MCMC procedure, fixing single parameters according to their maximum likelihood value in the model and obtaining the resulting likelihood distributions for the remaining parameters according to that restricted model.

The results listed in table 3.3 serve as the model parameters for the analysis of diffuse scattering from the Mo/B₄C/Si/C sample in chapter ?? below.

3.2 Molybdenum Thickness Variation in Mo/Si/C Multilayers

In the following we shall apply and extend the reconstruction procedure discussed in the above section to the problem of multilayer sample systems deposited with varying molybdenum layer thicknesses. For the engineering of a near-normal incidence mirror, the ratio of molybdenum layer thickness to total period thickness has a clear impact on the reflectivity curve as seen in Fig. 3.4c. Studies have shown, that an optimal value for high reflectivity is achieved by depositing 40% molybdenum layer thickness d_{Mo} with respect to the total period thickness D [4, 17]. During the deposition process, the layer of molybdenum grows in thickness and at a certain threshold, crystallites may begin to form [4, 78] inside the layer. Those may affect the interface morphology of the layer system at the boundaries to the molybdenum layer and possibly at further interfaces through correlation effects. This potentially increases the roughness and thus the loss of specularly reflected radiation. For the deeper understanding of those effects, we shall reconstruct the layer structure and determine the molybdenum layer thickness in each sample in comparison to the nominal values for the magnetron sputtering deposition.

3.2.1 Sample systems and experimental procedure

As a specific prototype for high-reflectance multilayer mirrors for the spectral range between 12.4 nm and 14.0 nm serve two sets of several samples of Mo/Si/C multilayer systems with C interdiffusion barriers with thicknesses of nominally below 0.5 nm at the Mo on Si interfaces (a detailed figure of the model for those samples is given below in Fig. 3.9 of the following sections). As mentioned above, the samples under investigation here were fabricated with increasing relative Mo thickness while keeping the nominal period thickness $D \approx 7$ nm constant. In this study, we investigate two sets of samples. In the first set, the magnetron sputtered layers were deposited one after another for each sample. In the second set, during deposition, an additional polishing process was used once during sputtering each period to counteract the possible roughening due to the crystallization. The nominal values of the molybdenum layers in the two sample sets are listed in table 3.4.

nominal d_{Mo} / nm (unpolished samples)	nominal d_{Mo} / nm (polished samples)
1.70	1.70
1.85	1.85
2.00	2.00
2.15	2.15
2.30	2.30
2.45	2.45
2.60	2.60
2.75	2.75
2.90	2.90
-	3.05

Table 3.4 | List of nominal molybdenum layer thicknesses in the two sample sets. Both sets were fabricated with a equidistant increase in thickness from 1.70 nm to 3.05 nm with 9 unpolished and 10 polished samples.

Fout?

Spectrally resolved EUV reflectivity curves at an angle of incidence from the surface

CHARACTERIZATION OF THE MULTILAYER STRUCTURE FOR DIFFERENT SYSTEMS

normal of $\alpha_i = 15^\circ$ and in the wavelength range from 12.4 nm to 14.0 nm have been measured for all samples at the EUVR beamline at the MLS. The data obtained is shown in Fig. 3.7 sorted by the nominal molybdenum layer thickness. The reflectivity curves in

Figure 3.7 | a) Reflectivity curves for the unpolished samples across the wavelength at a fixed angle of incidence of $\alpha_i = 15^\circ$ from the surface normal. The nine samples differ by the nominal Mo layer thickness indicated at the bottom axis. b) Reflectivity curves of the ten polished samples measured under the same conditions as for the first sample set.

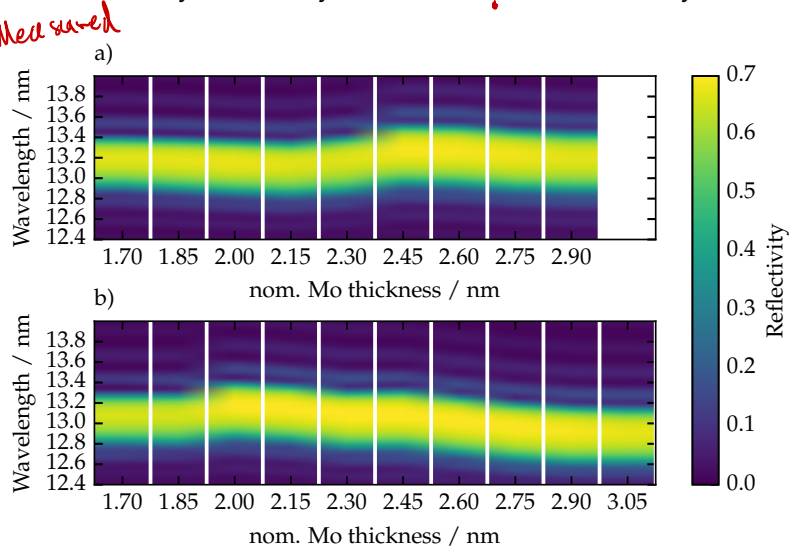


Fig. 3.7a and Fig. 3.7b have the characteristic curve shape of periodic EUV multilayer mirrors with a main broad maximum and side fringes, very similar to the mirror sample discussed in Sec. 3.1 above. In direct comparison of the measured reflectivity data, shifts of the peak center position are clearly visible. As illustrated in Fig. 3.4 above, several properties of a multilayer stack, e.g. molybdenum content and period thickness, contribute to such a difference. Clear differences in the peak reflectance value can also be observed in the two subfigures, with strong increases at $d_{\text{Mo}}^{\text{nom}} = 2.45 \text{ nm}$ for the unpolished set and at $d_{\text{Mo}}^{\text{nom}} = 2.00 \text{ nm}$ for the polished set. In all samples the only nominal difference, i.e. the only parameter changed during the deposition process, is the relative molybdenum thickness. The increase in reflectance and peak broadening are therefore indicators for an abrupt change in the multilayer properties.

For the purpose of obtaining additional information about the samples, in addition to the EUV reflectivity curves above, all samples were measured after deposition using a lab-based Cu-K α hard x-ray diffractometer at the Fraunhofer IWS Dresden, Germany. The XRR data is shown in Fig. 3.8 for the set of unpolished and polished samples in direct comparison. The position of the Bragg peaks and their respective intensity contain additional information on the layer stack thicknesses and its interface properties. In both cases, shifts of the peak positions similar to those observed in the EUV curves become apparent. Especially the higher orders towards larger grazing incidence angles show distinct differences. In addition, in direct comparison of the XRR curves for the respective sample with $d_{\text{Mo}}^{\text{nom}} = 3.05 \text{ nm}$ from the unpolished and polished sets (on the top of Fig. 3.8a and Fig. 3.8b), a higher intensity for higher-order Bragg peaks above grazing angles of incidence of $\alpha_i^{\text{GI}} > 7^\circ$ can be observed for the polished sample. This hints towards an improved interface definition and sharpness due to the polishing process and consequently a lower roughness or interdiffusion. *EUV and XRR data*

In the following section we shall analyze the data discussed here to reconstruct a model of the samples using the MCMC approach introduced in Sec. 3.1 in order to verify the observations made here.

and intensity

Der Sprung im zentralen Bereich?

|| are?

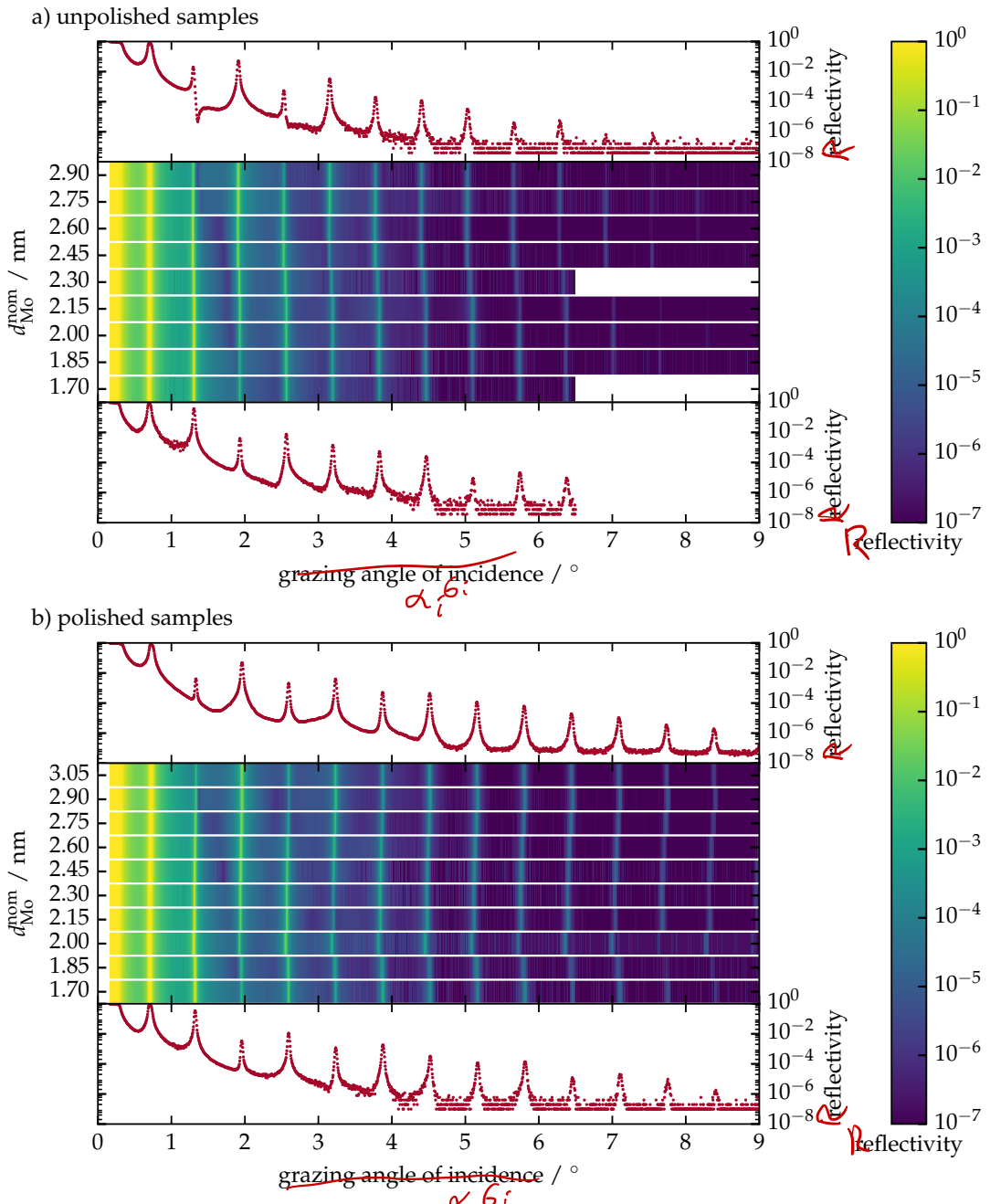


Figure 3.8 | XRR data for all unpolished and polished samples shown in dependence on the nominal molybdenum layer thickness d_{Mo}^{nom} . In each of the subfigures a) and b) the XRR measurements for the sample with smallest and largest d_{Mo}^{nom} are shown on the bottom and the top of the subfigure, respectively. In between, the XRR curves are illustrated in as a color map plot.

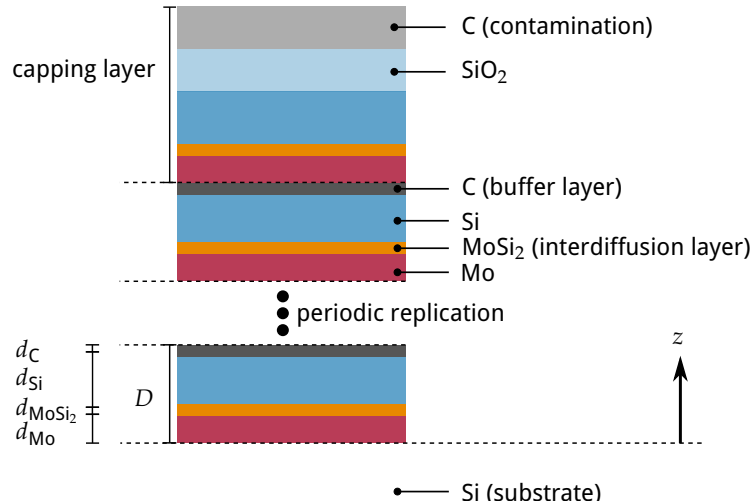
and $\alpha_i^{C_i}$ (at $Cu-K_\alpha$) ? shown

3.2.2 Combined Analysis of X-ray and EUV reflectance

To obtain the actual layer thicknesses in the samples, we analyzed the data of the EUV reflectivity and XRR experiments and reconstructed these parameters by modeling and by combined analysis of the measured data. Both reflectivity curves are calculated by introducing a model for the multilayer system and applying the matrix formalism described in detail in the theory part of this thesis, Sec. 1.3. The model defined in the following paragraph is applied to both data sets.

The thicknesses of the Mo layers inside the stack were varied nominally from 1.7 nm to 3.05 nm from sample to sample, where the unpolished sample set lacks the last nominal thickness. The stacking of the different layers in the multilayer consists of the Mo and Si layers, as well as an additional C buffer layer at the Mo on Si interface to prevent interdiffusion. For the Si on Mo interfaces, no buffer layers were included since interdiffusion is usually less in this case [59]. However, for the theoretical description of the sample stack we consider an additional MoSi_2 layer in the model, which is well known to form during the deposition process [4]. The full model used in the reconstruction is illustrated in Fig. 3.9 with the thickness parameters for each layer. To account for any

Figure 3.9 | Model of the multilayer stack including the substrate and the capping layers. The periodic part is enclosed between the dashed lines with four layers in each period repeated 49 times. The capping period does not include an interdiffusion layer but has a natural SiO_2 layer and a carbon-like layer accounting for contamination on the top surface.



contamination on the top sample surface, an additional carbon-like layer as the upper most layer was considered. In addition to the thicknesses of each layer we also allowed for a variation of the layer density between 80% and 100% of the bulk density. The model parameters and their boundaries entering in the optimization procedure are listed in table 3.5. Similar to the $\text{Mo}/\text{B}_4\text{C}/\text{Si}/\text{C}$ in Sec. 3.1, a Nérot-Croce damping factor was assumed to account for specular reflectivity loss due to interface imperfections.

Table 3.5 | Parametrization of the Mo/Si/C multilayer samples with varying molybdenum layer thicknesses.

Parameter	Definition	Lower bound	Upper bound
$d_{\text{Mo}} / \text{nm}$	Mo layer thickness	0.0	4.5
$d_{\text{Si}} / \text{nm}$	Si layer thickness	0.0	7.0
d_{C} / nm	C buffer layer thickness	0.0	0.6
$d_{\text{MoSi}_2} / \text{nm}$	MoSi ₂ interdiffusion layer thickness	0.0	0.6
σ / nm	Nérot-Croce parameter (identical for all interfaces)	0.0	0.5
ρ_{Mo}	Mo density w.r.t. bulk density	0.8	1.0
ρ_{Si}	Si density w.r.t. bulk density	0.8	1.0
ρ_{C}	C density w.r.t. bulk density	0.8	1.0
ρ_{MoSi_2}	MoSi ₂ density w.r.t. bulk density	0.8	1.0
Capping layer			
$d_{\text{C}(\text{cap})} / \text{nm}$	C capping layer thickness	0.0	3.0
$d_{\text{SiO}_2(\text{cap})} / \text{nm}$	SiO ₂ capping layer thickness	0.0	1.5
$\rho_{\text{C}(\text{cap})}$	C density w.r.t. bulk density	0.0	1.0
$\rho_{\text{SiO}_2(\text{cap})}$	= ρ_{Si} (identical to Si density)		

Optimization functional and procedure

The data analysis was conducted similarly to the procedure described in Sec. 3.1. However, for the samples studied here, data from two separate experiments was measured with the goal to improve the reconstruction of the model. Due to the increased amount of data through the additional XRR measurements, a definition for a combined χ^2 functional is required to allow an analysis based on both data sets. The two data sets, i.e. the EUV and XRR reflectivity curves have significantly different number of ~~points~~ data points, which are not entirely ~~independend~~ independent of each other. In case of the XRR curve increasing the number of data points, e.g. by reducing the angular step size by half does not lead to better statistics due to systematic errors. Defining a χ^2 functional as the total sum of all measured data point residuals, i.e. both the EUV data and the XRR data would therefore create an unwanted weighting due to the large amount of XRR data points in comparison to far fewer EUV data points. To avoid this effect, we define the combined χ^2 functional as the sum of the reduced $\tilde{\chi}^2$ functionals. The $\tilde{\chi}^2$ is equivalently defined to Eq. (3.1) through,

$$\tilde{\chi}^2 = \frac{1}{M - P} \left[\sum_m \frac{(I_m^{\text{model}} - I_m^{\text{meas}})^2}{\tilde{\sigma}_m^2} \right], \quad (3.5)$$

for each of the datasets separately. The reduced $\tilde{\chi}^2$ can be interpreted as the average of the squared residuals of model prediction and experiment. Thereby, each experiment is reduced to a single comparable quantity. By the definition of

$$\chi^2 = \tilde{\chi}_{\text{EUV}}^2 + \tilde{\chi}_{\text{XRR}}^2, \quad (3.6)$$

we are therefore enabled to obtain confidence intervals for the parameters of the model, which represent a conservative (upper limit) estimation for the combined analysis of both

CHARACTERIZATION OF THE MULTILAYER STRUCTURE FOR DIFFERENT SYSTEMS

experiments, similarly to the procedure for a single EUV curve as described in Sec. 3.1 above. The combined χ^2 functional enters the likelihood through Eq. 3.4.

The solution to the inverse problem of reconstructing the optimal model parameters is conducted by minimizing the χ^2 functional (or equivalently maximizing the likelihood). To minimize the functional with respect to the best choice of parameters, we apply the MCMC method as described above for the Mo/B₄C/Si/C sample system. We do not start with a PSO optimization, since the sample system is numerically simpler due to the decreased amount of layers and interfaces. The MCMC method itself yields an optimization result, although slower in convergence, as mentioned in the discussion of the procedure above in Sec. 3.1.2. As a starting point, again a random set of parameters is generated with respect to predefined boundaries listed in table 3.5. The limits are chosen in reference to prior knowledge and physical plausibility. Confidence intervals for each value within the underlying model are estimated from the likelihood distribution resulting from the MCMC as one standard deviation of the sample distribution in each parameter.

We shall discuss the results of the optimization procedure at the example of the unpolished sample with nominal molybdenum layer thickness of $d_{\text{Mo}}^{\text{nom}} = 3.05 \text{ nm}$. The results of the MCMC maximum likelihood estimation for the other samples were found to show the same properties and the same findings discussed in the following with the only distinction of broader or even improved distributions in some cases. The latter causes the confidence intervals to be different for the respective parameters. The reason for the broader likelihood distribution is clearly a decreased applicability of the model in some cases possibly due to changes through crystallization. Nevertheless, the model still shows sufficiently good agreement with the data.

As a first step, the MCMC procedure was performed within the defined boundaries for all parameters. An unambiguous result was only found with respect to the thickness parameters of Mo, with the smallest confidence intervals in comparison to all other parameters, and Si, as well as for the Nérot-Croce parameter σ , whereas all other parameters show broad likelihood distributions within the predefined boundaries not allowing a unequivocal parameter determination. Therefore, the best model was obtained in a two-step process. First the MCMC optimization was performed including all parameters as mentioned above. Proceeding from this, the value of the Mo thickness with its confidence interval was obtained by marginalizing over all other parameters, yielding the most precise parameter estimation from the procedure. The results for the molybdenum and silicon layer thickness parameters are shown in Fig. 3.10. In comparison

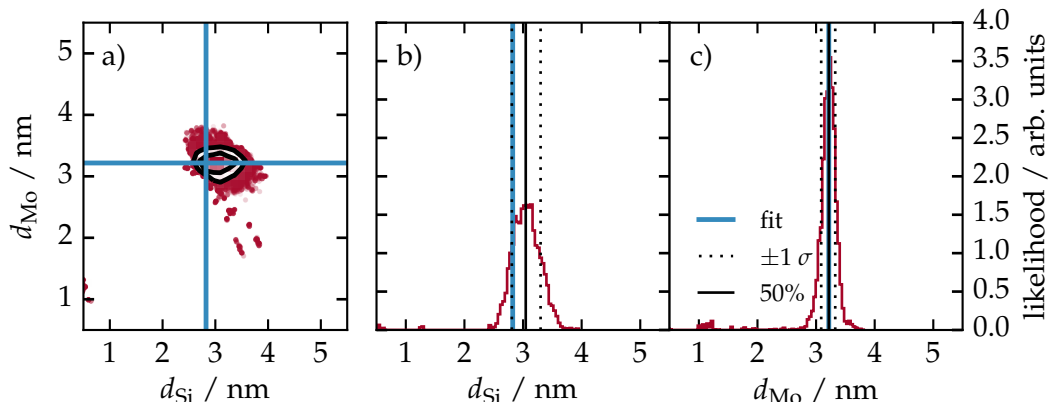


Figure 3.10 | Combined analysis

A

1 ? ✓

to the analysis based on only EUV data for the Mo/B₄C/Si/C in Fig. 3.5, the inclusion of additional XRR measurements lead to significantly smaller confidence intervals and thus higher accuracy of the reconstruction, although the two systems have a limited comparability due their different layer layouts. The method of combining the analysis of two datasets of EUV and XRR measurements has been previously applied by others [80], which have come to the same result of a significantly improved model reconstruction.

In a second step, another MCMC optimization was performed on a reduced parameter set, fixing the determined molybdenum layer thickness to its optimal value, i.e. the 50% percentile of its distribution. Finally, the layer thicknesses of the C barrier layer and the MoSi₂ interdiffusion layer were fixed to their nominal values of $d_C = d_{\text{MoSi}_2} = 0.5 \text{ nm}$. Due to the broad distribution result for the likelihoods of those parameters, this comes without a limitation of the generality for this analysis, since any value is valid within the predefined boundaries. Additionally, this ensures comparability of the models for all samples without constraining the applicability of the model with respect to the data available.

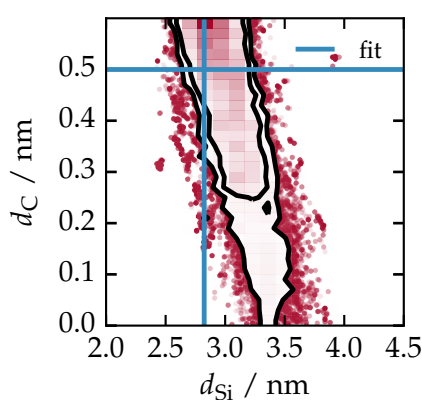


Figure 3.11 | Two-dimensional likelihood distribution indicating the correlation of silicon and carbon layer thickness. The distribution was obtained by marginalizing over all remaining parameters of the model. The blue lines indicate the fit obtained through the two-step MCMC optimization procedure (see main text).

The results of the second MCMC procedure of the resticted model yield the remaining values for the model parameters by obtaining the globally best solution found. The final result is indicated by the blue solid lines in Fig. 3.10. Due to the choice to restict the model to a buffer layer thickness of $d_C = 0.5 \text{ nm}$, we find the optimal solution for the silicon layer thickness at the limit of one standard deviation in Fig. 3.10b. The distributions shown represent the MCMC results of the unrestricted model, where the silicon and carbon layer thicknesses are strongly correlated as shown in Fig. 3.11. By restricting the carbon layer thickness to its nominal value, this correlation is resolved and the corresponding silicon layer thickness is well within the interval of one standard deviation as indicated through the solid black contours in Fig. 3.11.

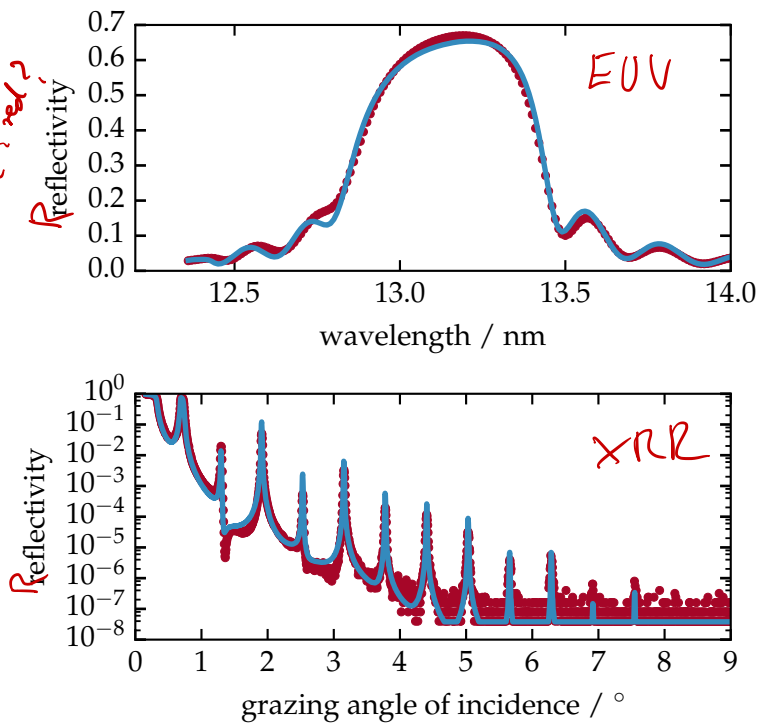
Was wind
herr 1.
EUV →
SiC → D

1st „best fit“ = max likelihood ?

3.2.3 Optimization results

The theoretical reflectivity curves calculated from the optimal model parameters for the unpolished sample with $d_{\text{Mo}}^{\text{nom}} = 3.05 \text{ nm}$ are shown in Fig. 3.12. Overall, a very good agreement of the two experiments with the theoretical curve are obtained. The full list for

Figure 3.12 | Experimental data in comparison with the theoretical curves calculated with the model parameters obtained from the combined analysis of EUV and XRR data. The data shown here was measured on the unpolished sample with nominal molybdenum thickness of $d_{\text{Mo}}^{\text{nom}} = 3.05 \text{ nm}$.



all molybdenum layer thicknesses for all samples and the respective confidence intervals in comparison to their nominal layer thickness are given in table 3.6.

Table 3.6 | List of nominal molybdenum layer thicknesses in the two sample sets. Both sets were fabricated with a equidistant increase in thickness from 1.70 nm to 3.05 nm with 9 unpolished and 10 polished samples.

nom. $d_{\text{Mo}} / \text{nm}$	EUV & XRR (unpolished)	EUV & XRR (polished)
1.70	$1.81(-0.12/+0.24)$	$1.77(-0.22/+0.19)$
1.85	$1.98(-0.15/+0.14)$	$1.91(-0.12/+0.17)$
2.00	$2.08(-0.11/+0.22)$	$2.29(-0.28/+0.13)$
2.15	$2.31(-0.22/+0.21)$	$2.45(-0.43/+0.06)$
2.30	$2.43(-0.09/+0.16)$	$2.60(-0.12/+0.14)$
2.45	$2.68(-0.13/+0.16)$	$2.58(-0.21/+0.15)$
2.60	$2.91(-0.17/+0.12)$	$2.87(-0.22/+0.12)$
2.75	$3.02(-0.15/+0.15)$	$3.03(-0.16/+0.14)$
2.90	$3.22(-0.13/+0.11)$	$3.15(-0.13/+0.13)$
3.05	-	$3.47(-0.19/+0.13)$

The optimal parameters for the molybdenum layer thickness d_{Mo} and the period thickness D found for both sample sets in the two-step MCMC analysis are shown in Fig. 3.13. The confidence intervals shown in Fig. 3.13a are one standard deviation of the likelihood determined for the Mo layer thickness by the first-step MCMC procedure, i.e. for the unrestricted model with the parameter limits as listed in table 3.5. The results show the desired linear increase in molybdenum layer thickness, however at a systematically higher thickness than the nominal values. A possible cause for that

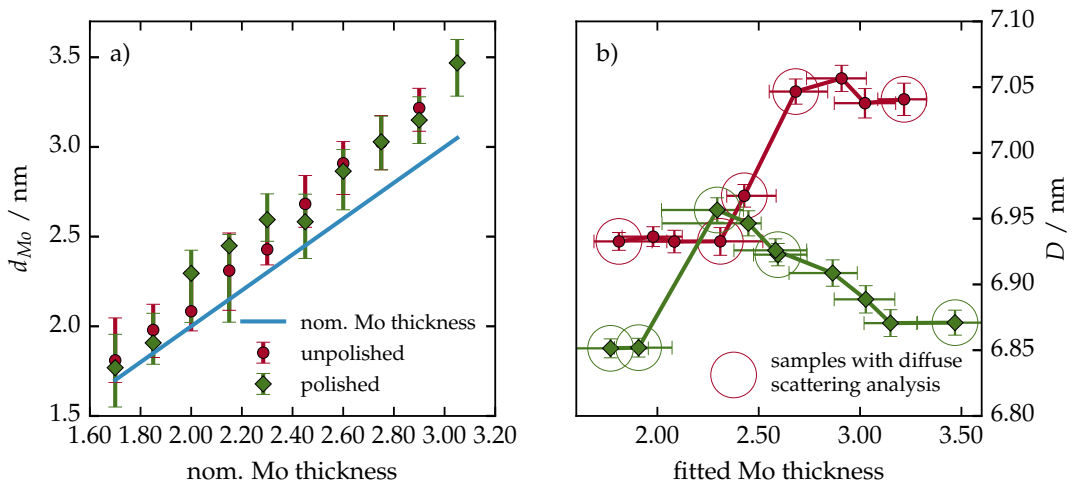


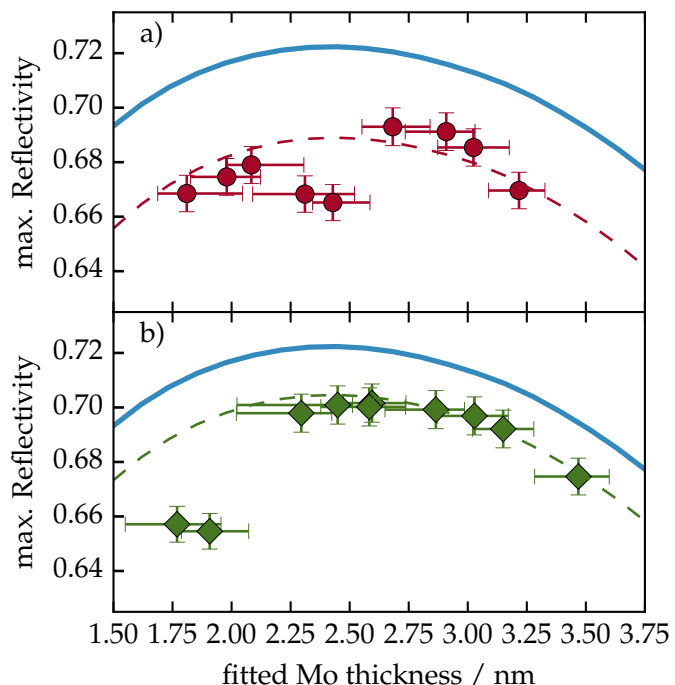
Figure 3.13 | a) Fitted Mo thickness values for both sample sets resulting from the MCMC analysis (see text). The nominal Mo layer thickness is shown in comparison with the obtained thicknesses. b) Fitted total period thickness D for both sample sets. For both sample sets, clear jumps can be observed at approx. $d_{\text{Mo}}^{\text{nom}} = 2.00 \text{ nm}$ and $d_{\text{Mo}}^{\text{nom}} = 2.38 \text{ nm}$, respectively, which is attributed to the crystallization threshold (see text). The marked (circle) samples were measured and analyzed with respect to the diffuse scattering.

observation, consistent with the model reconstruction results, is the possible interdiffusion of the molybdenum layer with the silicon and carbon during deposition. This would reduce the relative density of the molybdenum layer. The reconstruction results for all samples indeed show systematically reduced density values of $\rho_{\text{Mo}} \approx 90\%$ w.r.t. the Mo bulk density. Thus, the nominal amount of deposited molybdenum leads to higher thicknesses than desired. In Fig. 3.13b the fitted period thicknesses D are shown in dependency of the fitted molybdenum thicknesses.

For both sets, distinct jumps can be observed between $d_{\text{Mo}} \approx 1.9 \text{ nm}$ and $d_{\text{Mo}} \approx 2.3 \text{ nm}$ for the polished samples and between $d_{\text{Mo}} \approx 2.3 \text{ nm}$ and $d_{\text{Mo}} \approx 2.7 \text{ nm}$ for the unpolished set. To better understand this observation, Fig. 3.14 shows the maximum peak reflectance of all EUV measurements also as a function of the reconstructed Mo layer thickness. The identical blue solid line in both subfigures indicates the maximum peak reflectance attainable for a perfect multilayer system with the respective Mo layer thickness without any interdiffusion or roughness. For the calculation a carbon capping layer of $d_{\text{C(cap)}} = 2.0 \text{ nm}$ and a relative density of $\rho_{\text{C(cap)}} = 0.5$ and a silicon dioxide layer of $d_{\text{SiO}_2} = 2.0$ was considered. The dashed curves in both figures show the expected maximum peak reflectance values for the two sample systems calculated by adding the respective roughness/interdiffusion to the model and varying the molybdenum thickness accordingly. In both cases, a significant dip with respect to the expected value can be observed starting at thicknesses of $d_{\text{Mo}} = 2.31(-0.22/+0.21) \text{ nm}$ for the unpolished samples in Fig. 3.14a and at $d_{\text{Mo}} = 1.77(-0.22/+0.19) \text{ nm}$ for the polished samples in Fig. 3.14b. We attribute this significantly diminished peak reflectance to the process of crystallization as the most likely cause. These values are consistent with the increase observed in the period thickness for both cases. However, the jump in the period thickness value with the increasing molybdenum layer thickness is observed one (in case of the unpolished samples) to two data points (in case of the polished samples) after the first dip in peak reflectance. Possibly, the deposition is affected by the crystallization threshold causing the increase in period thickness. The values measured here for the dip in peak

Jarmi
Eisner
Weklin
Lohr

Figure 3.14 | Peak reflectance values for each sample obtained from the EUV measurements for the unpolished sample set (a) and the polished sample set (b). The maximum theoretical reflectance is shown in both subfigures for a perfect (no roughness or interdiffusion) layer system with the same specifications as the samples.



reflectance is in agreement with earlier observation of molybdenum crystallization in literature [4] for the unpolished samples set. The polishing process shifts that threshold to lower thicknesses by approximately 0.2 nm to 0.3 nm.

For a deeper investigation of the interface morphology during the presumed crystallization threshold, EUV diffuse scattering experiments have been conducted for selected samples of the respective set. The selection is marked with open circles in Fig. 3.13. To gain a deeper understanding of the reflectivity dip and the period increase, the samples in vicinity of this feature in the Fig. 3.14 and Fig. 3.13 were investigated in comparison to reference samples above and below the threshold. This analysis is the topic of chapter ?? of this thesis and described and discussed in detail there based on the reconstruction results obtained here.

3.3 Analysis of Cr/Sc Multilayers with Sub-nanometer Layer Thickness

In the previous sections we have characterized multilayer systems specifically designed to reflect radiation in the EUV spectral range from 12.5 nm to 14.0 nm wavelength. There, the three to four layer systems per period with period thicknesses of $D \approx 7$ nm were used to achieve constructive interference at the desired reflection angles. We shall now expand the analysis to a different system. Multilayer mirrors designed to reflect radiation in the spectral range between 2.2 nm and 4.4 nm wavelength, the so called *water window*. Those systems share the basic principle of a one-dimensional Bragg crystal with the Mo/Si multilayer stacks from the previous sections, but differ in the selection of materials. The intrinsic relationship between spectral range and period thickness to achieve constructive interference, requires period thicknesses of $D \approx 1.5$ nm for this case and higher period replication.

The system we focus on in the rest of this chapter is composed out of a bilayer stack

Was? Bitte mehr Infos, entweder hier oder Ch. 2

of chromium (Cr) and scandium (Sc). A detailed description of the sample preparation process and the choice of the layer materials can be found in Ch. 2, Sec. 2.4.1. The sample is optimized to reflect radiation of $\lambda = 3.14 \text{ nm}$ at an angle of incidence of $\alpha_i = 1.5^\circ$. Its periodicity is $N = 400$ bilayer periods, where the last period has a larger Cr capping layer thickness. The model of the sample is shown in Fig. 3.15. The small period thickness

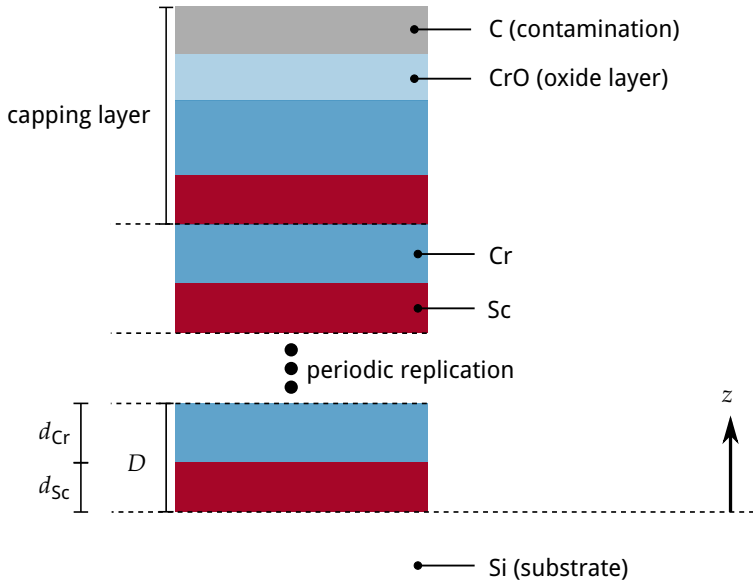


Figure 3.15 | Model of the multilayer stack including the substrate and the capping layers. The periodic part is enclosed between the dashed lines with four layers in each period repeated $N = 64$ times. The capping period does not include an interdiffusion layer but has a natural SiO_2 layer.

of only $D \approx 1.5 \text{ nm}$ for this type of sample yields individual layer thicknesses in the sub-nanometer regime, for a bilayer period with approximately equal individual layer thicknesses. This is a significant difference to the Mo/Si systems treated in the beginning of this chapter, where the molybdenum and silicon layers were well above $> 1.7 \text{ nm}$, even in the smallest case existed. The buffer and interdiffusion layers, which nominally have thicknesses in the same order of magnitude as expected for the Cr/Sc system, could not be characterized based on the methods employed above. We shall therefore first compare the results obtained with an approach similar to the methods in the previous sections to establish a limit to the applicability of discrete layer models.

3.3.1 Reconstruction with a discrete layer model approach

In analogy to Sec. 3.2, we seek to reconstruct the individual layer thicknesses based on experimental data. For this we construct a discrete layer model as illustrated in Fig. 3.15 in analogy to the procedure applied for the Mo/Si multilayer systems. The parameters of this discrete layer model are listed in table 3.7 together with the upper and lower bound for the particle swarm optimization procedure.

The reflectivity of the sample in the water window spectral range from 3.12 nm to 3.16 nm was measured at the SX700 beamline at BESSY II. The angle of incidence was $\alpha_i = 1.5^\circ$ (corresponding to a grazing angle of incidence of $\alpha_i^{\text{GI}} = 88.5^\circ$), which corresponds to the design goal for this mirror prototype. In addition, similar to the Mo/Si samples, a XRR measurement was conducted in the DESY laboratory using a laboratory-based X-ray diffractometer (X’Pert PRO MRD, Panalytical). The diffractometer is equipped with a high-resolution goniometer and uses $\text{Cu}-\text{K}\alpha$ radiation. The XRR intensities were recorded using a PIXcel counting detector. The dynamic range achieved in the measurements

CHARACTERIZATION OF THE MULTILAYER STRUCTURE FOR DIFFERENT SYSTEMS

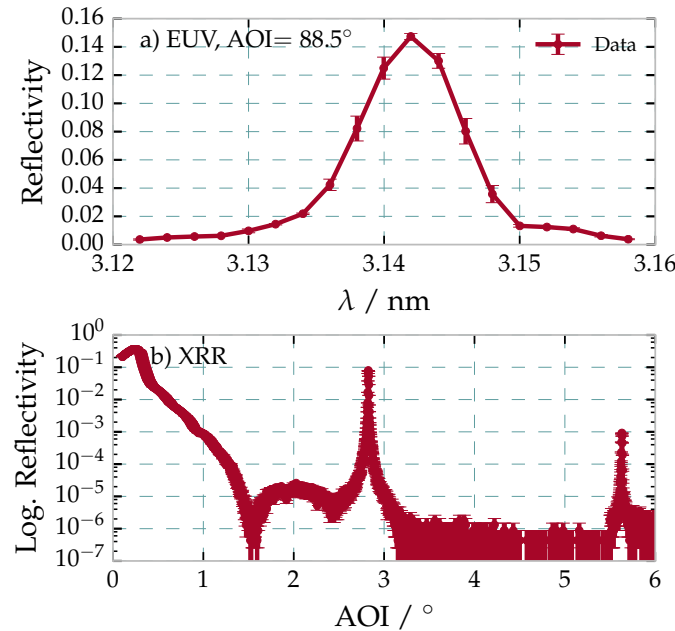
Table 3.7 | Parametrization of the Cr/Sc binary multilayer model.

Parameter	Definition	Lower bound	Upper bound
$d_{\text{Cr}} / \text{nm}$	Cr layer thickness	0.0	1.5
$d_{\text{Sc}} / \text{nm}$	Sc layer thickness	0.0	1.5
σ / nm	Nérot-Croce parameter (identical for all interfaces)	0.0	0.5
ρ_{Cr}	Cr density w.r.t. bulk density	0.5	1.0
ρ_{Sc}	Sc density w.r.t. bulk density	0.5	1.0
Capping layer			
$d_{\text{C}(\text{cap})} / \text{nm}$	C capping layer thickness	0.0	1.0
$d_{\text{CrO}(\text{cap})} / \text{nm}$	SiO ₂ capping layer thickness	0.0	1.5
$d_{\text{Cr}(\text{cap})} / \text{nm}$	SiO ₂ capping layer thickness	0.0	3.0
$\rho_{\text{C}(\text{cap})}$	C density w.r.t. bulk density	0.0	1.0
$\rho_{\text{CrO}(\text{cap})}$	CrO density w.r.t. bulk density	0.0	1.0
$\rho_{\text{Cr}(\text{cap})}$	Cr (cap) density w.r.t. bulk density	0.5	1.0

extended down to a reflectance of 10^{-6} for grazing angles of incidence of $\alpha_i = 0^\circ$ to $\alpha_i = 3^\circ$.

Both measurement curves are shown together in Fig. 3.16. Due to the short period of

Figure 3.16 | EUV and XRR



the multilayer sample, only two Bragg peaks could be observed in this angular range. All higher order peaks were below the detection threshold of 10^{-6} in reflected intensity. The dominating experimental uncertainty was the inhomogeneity of the sample stack across the sample area. The given uncertainty values for each of the measurement points were estimated, by measuring the peak reflectance on positions marking a cross of 2 mm by 2 mm in the sample center. This data was compared to theoretical expectance value based on a PSO fit of the discrete layer model above for the EUV curve (for details of the optimization results see below). From this a drift of the period thickness D was obtained

and uncertainties were calculated as the difference of two theoretical curves attaining the maximum and minimum D values. Similarly, uncertainties for the XRR curves were calculated by simulating theoretical curves based on the same period drifts.

In comparison, the most remarkable difference with respect to the Mo/Si mirrors is the significantly reduced peak reflectance of the EUV curve in Fig. 3.16a compared to the curves in Fig. 3.1 and Fig. ??c. The maximum value attained is only approximately $R_{\max} \approx 15\%$ while it is up to $R_{\max} \approx 70\%$ for the Mo/Si systems. The reasons for this are the different spectral range and the material properties at the water window wavelengths.

To better illustrate the differences to the Mo/Si systems, we have conducted an analysis based on the discrete layer model of a Cr/Sc multilayer as described above. The particle swarm optimization was done based on the EUV data shown in Fig. 3.16a and the parameters and limits listed in table 3.7. The resulting parameters are listed in table 3.8. The capping layer results were obtained in a combined PSO analysis based on the EUV

Parameter	PSO result
$d_{\text{Cr}} / \text{nm}$	0.8224
$d_{\text{Sc}} / \text{nm}$	0.7510
σ / nm	0.375
ρ_{Cr}	0.876
ρ_{Sc}	0.957
Capping layer	
$d_{\text{C}}(\text{cap}) / \text{nm}$	0.462
$d_{\text{CrO}}(\text{cap}) / \text{nm}$	1.143
$d_{\text{Cr}}(\text{cap}) / \text{nm}$	2.322
$\rho_{\text{C}}(\text{cap})$	0.502
$\rho_{\text{CrO}}(\text{cap})$	0.618
$\rho_{\text{Cr}}(\text{cap})$	0.851

Table 3.8 | PSO fit results for the discrete layer Cr/Sc multilayer model. The bulk multilayer parameters were obtained by exclusively applying the PSO method to the EUV data. The capping layer parameters were deducted from the XRR data excluding the Bragg peaks in a combined analysis.

and XRR data excluding the areas of the Bragg peaks. This grazing incidence reflectivity data has a very high sensitivity for the top surface layers, which can not be deducted from an EUV curve alone as demonstrated in Sec. 3.1.

The theoretical curve obtained from the PSO procedure is shown in Fig. 3.18 in direct comparison with the theoretically achievable maximum reflectivity curve. The latter was obtained by calculating the resulting reflectivity based on the parameter results in table 3.8, but without any roughness or interdiffusion, i.e. by requiring $\sigma \equiv 0.0$. The Sc to Cr ratio was found to be $\Gamma_{\text{Sc}} = d_{\text{Sc}}/d_{\text{Cr}} = 0.48$ with a high r.m.s. value of $\sigma = 0.385 \text{ nm}$ for the Nérot-Croce factor. While the EUV reflectance curve shows excellent agreement with the measured data, there is a significant offset to the theoretically achievable maximum reflectance. For the particular model derived above, theoretical reflectance values of $R_{\max} > 50\%$ are possible. This large difference, especially compared to Mo/Si systems which are very close to the theoretically achievable maximum reflectance (cf. Fig. 3.14), hints at strong roughness or intermixing of the two materials. To verify the applicability of the discrete (binary) layer model used here, the calculated curves for both experiments, the EUV and XRR curve, are shown together in Fig. 3.18.

Again, the EUV data is matched excellently, while in the case of the XRR measurement the first Bragg peak is found to be matched by the model also in the hard x-ray regime. However, the second Bragg resonance, clearly visible with a peak reflectance value of

Figure 3.17 | Fitted experimental EUV reflectance curves across the wavelength of the radiation impinging at $\alpha_i = 1.5^\circ$ from normal, based on the binary model. The green curve shows the maximum possible reflectance assuming a perfect multilayer system without roughness or interdiffusion.

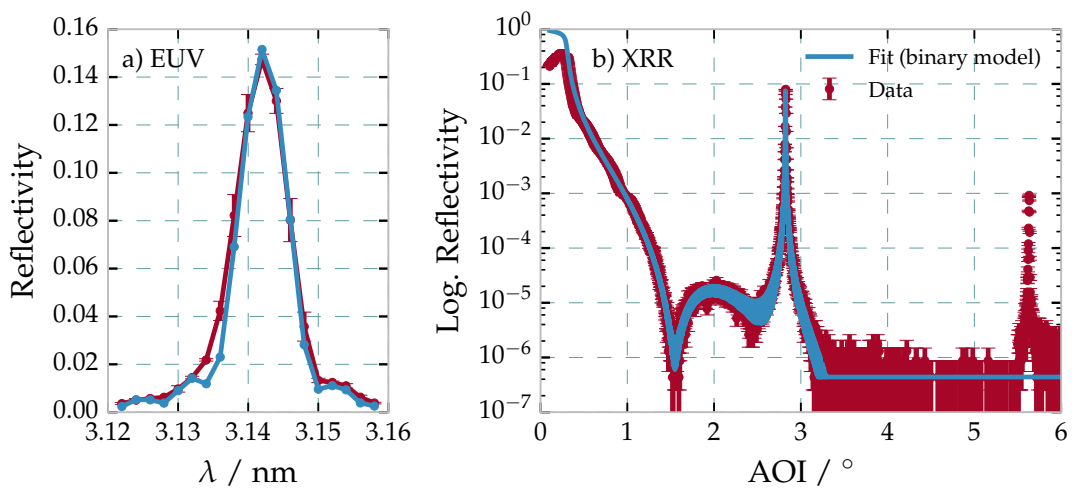
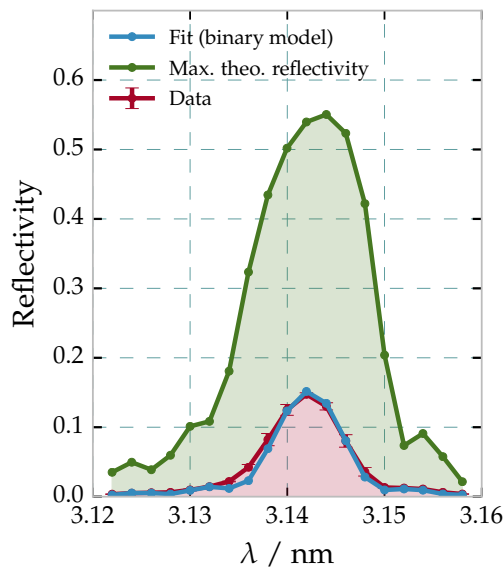


Figure 3.18 | a) Measured EUV reflectivity curve for and near-normal angle of incidence of $\alpha_i = 1.5^\circ$ together with calculated curve of the PSO-based binary model reconstruction. b) Measured and calculated XRR curves for the same sample and model parameters at grazing angles of incidence using radiation at the Cu-K α wavelength. A clear mismatch of the theoretical curve and the measured data can be observed for the second Bragg peak between $\alpha_i^{\text{GI}} = 5.0^\circ$ and $\alpha_i^{\text{GI}} = 6.0^\circ$.

approximately 10^{-3} is not represented by the model at all. A fully combined analysis similarly to the approach in Sec. 3.2 could not yield a consistent result. The r.m.s. value for σ required to reduce the theoretical EUV reflectance down to the measured level could not be brought into agreement with the XRR curves second Bragg peaks appearance. In a strictly binary model like this one with a layer thickness ratio of $\Gamma_{\text{Sc}} \approx 0.5$, the second Bragg peak is additionally suppressed due to symmetry reasons. Thus, there is a clear mismatch of the model reconstruction and the experimental observations, mostly due to the complementary data delivered through the measurement of the second Bragg peak of the XRR curve. This is a strong indicator, that the simple model as defined above does not suffice to describe the physical situation of the sample. Therefore, a more elaborate model is required introducing additional parameters to account for the increased complexity of the samples layer properties compared to the Mo/Si sample systems above.

3.3.2 Extending The Model to Graded Interfaces and Interdiffusion

The physical situation of Cr/Sc multilayer systems with individual layer thicknesses in the sub-nanometer regime is significantly different than in comparably large thicknesses of several nanometers such as in the Mo/Si case of the two preceding sections. It is well known [62], that magnetron sputtered Cr and Sc multilayer systems, similarly to the Mo/Si systems, suffer from imperfect interfaces. The main reason for that is interdiffusion of the two materials into each other. In addition, roughness at the interfaces exists and further diminishes an ideal chemically abrupt transition from one material to the next. Due to the small layer thicknesses required to achieve the first Bragg resonance upon near-normal incidence with radiation of $\lambda = 3.14 \text{ nm}$, roughness and interdiffusion may occur over an interdiffusion zone as large as the total layer thickness itself. The results from the specular EUV and XRR measurements shown above, clearly demonstrate that a binary model with only a Nérot-Croce damping parameter σ due not provide an accurate model for the physical reality. Instead, a more complex model is required. Here, we define a periodic model, repeated in units of one bilayer period, to account for possible interdiffusion gradients and intermixing between the two materials in the stack. The symmetry of two identically thick layers within one period in the simple model above leads to a suppression of the second order Bragg peak. Nevertheless, physically this symmetry effect can be broken by accounting for interdiffusion zones with different thicknesses, depending on whether Cr was deposited on Sc or vice versa. Thereby, the second Bragg peak is no longer suppressed even though both layers have the same thickness if the interdiffusion zones are asymmetric. Physical causality further dictates, that the two layers intermix gradually. The model, which we use to reconstruct the Cr/Sc multilayer sample measured above is illustrated in Fig. 3.19 in direct comparison to the simple model used before. The interdiffusion zones are modeled following a sinusoidal profile, which represents a smooth transition from the refractive index of the Cr layer to the Sc layer and vice versa. The thickness of those zones is given by the parameters s_{Sc} and s_{Cr} . For the calculation of the electromagnetic fields inside the stack, the interface region is sampled with a fixed number of equally spaced points in z -direction, effectively creating a region of thin sublayers with a gradually changing index of refraction (illustrated by the red stepped function in Fig. 3.19). To take into account intermixing extending across the full period, we introduced an intermixing parameter η . The effective indices of refraction of the individual Cr and Sc layers are then given

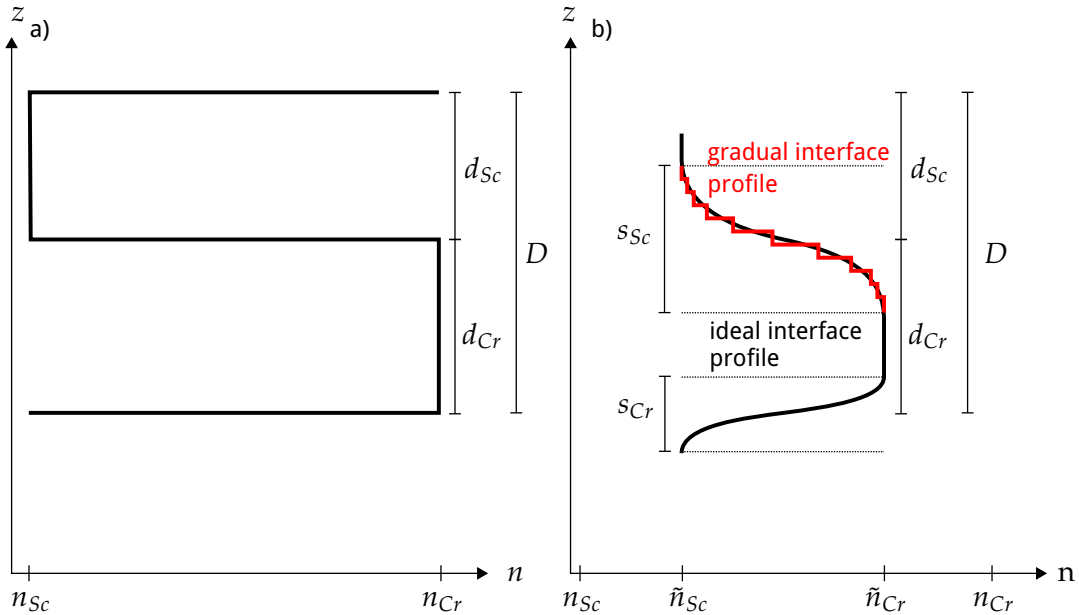


Figure 3.19 | a) Binary Cr/Sc multilayer model with total period thickness D and the individual layer thicknesses d_{Sc} and d_{Cr} . b) Model with explicit gradual interfaces following a sinusoidal profile. The ideal interface profile is approximated through discrete sublayers as indicated in red, forming the actual gradual interface profile entering the electric field calculations. The thickness of the interdiffusion zones can differ for the top and bottom interface in each period. Their total thicknesses are given by s_{Sc} and s_{Cr} . The effective index of refraction for both layers is given by \tilde{n}_{Sc} and \tilde{n}_{Cr} , respectively.

through

$$\begin{aligned} \tilde{n}_{Cr} &= (\eta/2)n_{Sc} + (1 - \eta/2)n_{Cr}, \\ \tilde{n}_{Sc} &= (1 - \eta/2)n_{Sc} + (\eta/2)n_{Cr}, \\ \text{for } \eta &\in [0, 1], \end{aligned} \quad (3.7)$$

where n_{Cr} and n_{Sc} are the tabulated values [39] with densities ρ_{Cr} and ρ_{Sc} .

With the definition of the model as outlined above, natural restrictions arise for the parameters. As an example, the interdiffusion zone region can not extend across half of the thickness of the original layers total thickness described by the parameter d_{Cr} or d_{Sc} , respectively. Instead, the intermixing parameter would have to be increased to account for that situation. The model is therefore parameterized according to the list of effective parameters given in table 3.9 together with their allowed ranges for the optimization procedure in analogy to the analysis conducted in the previous sections. The range limits arise either from physical plausibility or are intrinsic properties of the parameter definition. Here, D is the full period thickness, d_{Sc} and d_{Cr} are the nominal layer thicknesses of the Cr and Sc layers as indicated in Fig. 3.19, and ρ_{Sc} and ρ_{Cr} their respective densities with respect to their bulk densities $\tilde{\rho}_{Sc} = 2.989 \text{ g/cm}^3$ and $\tilde{\rho}_{Cr} = 7.19 \text{ g/cm}^3$ [39]. The loss of specular reflectance due to roughness-induced scattering is considered through the Nérot-Croce factor using σ_r identical at each interface. This is necessary to

Table 3.9 | Multilayer parametrization and parameter limits

Parameter	Definition	Lower bound	Upper bound
D / nm	$= d_{\text{Sc}} + d_{\text{Cr}}$	1.5	1.6
Γ_{Sc}	$= d_{\text{Sc}}/D$	0.0	1.0
s_d / nm	$= s_{\text{Sc}} + s_{\text{Cr}}$	0.0	1.6
Γ_s	$= s_{\text{Sc}}/s_d$	0.0	1.0
η	layer intermixing	0.0	1.0
σ_r / nm	r.m.s. roughness	0.0	0.5
ρ_{Sc}	Sc density w.r.t. bulk density	0.5	1.0
ρ_{Cr}	Cr density w.r.t. bulk density	0.5	1.0

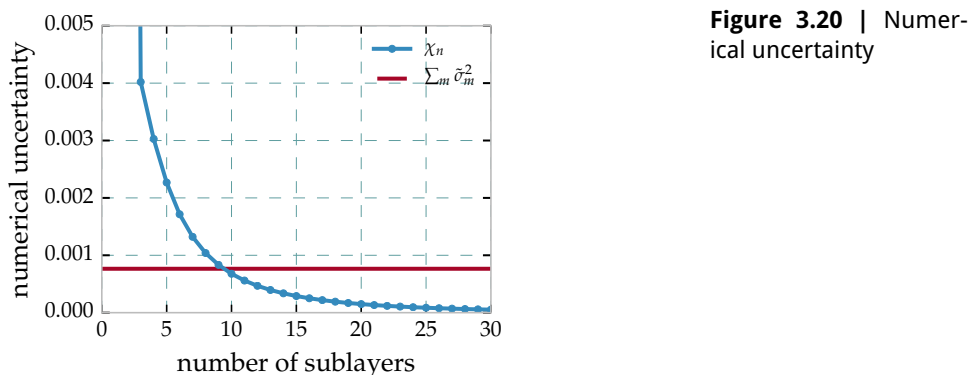
account for diffusely scattered light, which is missing in the measured specularly reflected radiation but can not be attributed to contrast loss due to interdiffusion. The parameter Γ_{Sc} indicates the portion of the Sc layer thickness with respect to the full period thickness D , which together uniquely define the thickness d_{Cr} ; Γ_σ describes the asymmetry of the widths of the interdiffusion zones at the Cr on Sc and Sc on Cr interfaces and is intrinsically limited to the interval $\Gamma_\sigma \in [0, 1]$. Note that s_{Sc} and s_{Cr} are half periods of the sinus functions used to describe the interface profiles. Therefore the condition $s_{\text{Sc}} + s_{\text{Cr}} \leq D$ holds.

The discretization of the smooth interface profile in the interdiffusion zones introduces an additional numerical uncertainty through the number of discretization points n required to reflect the physical situation of a smooth transition. To assert a lower limit for this number, we have evaluated the mean error introduced by coarse sampling. The most accurate experiment of the analysis within this chapter is given by the EUV reflectivity curve, which serves as a reference for this assertion through the sum of the squared uncertainty of each data point in Fig. 3.16a, $\sum_m \tilde{\sigma}_m$.

The numerical error of the model depending on the interface sampling through gradual sublayers was evaluated by comparing the sum of squares

$$\chi_n = \sum_m (I_m^{n=100} - I_m^n)^2 \quad (3.8)$$

of the difference theoretical EUV curves with increasing numbers of gradual interfaces and an “ideal” smooth transition represented by 100 sublayers. The model parameters used for this analysis were obtained through a PSO optimization of the model with respect to the EUV reflectivity curve. As illustrated in Fig. 3.20, the experimental


Figure 3.20 | Numerical uncertainty

CHARACTERIZATION OF THE MULTILAYER STRUCTURE FOR DIFFERENT SYSTEMS

uncertainty dominates at the lower limit of $n = 10$ sublayers for the interface zone. For the analysis in this chapter, and due to reasons of numerical effort required to calculate the electromagnetic field for all measurements discussed here, we use $n = 15$ sublayers for all calculations. At that value, the experimental uncertainty is clearly dominant and only a marginal additional uncertainty is acquired due to insufficient sampling.

As a verification of the applicability of the model to the problem of accurately representing a physical situation that could describe the EUV and XRR data shown in Fig. 3.16 above, we have applied the combined analysis technique for the two data sets described in Sec. 3.2.2 to the improved gradual model. The particle swarm optimization approach applied to obtain a global solution for the model parameters by minimizing the functional defined in Eq. (3.6). The results found for the binary model (cf. Fig. 3.18) and the gradual model are shown in direct comparison with each other in Fig. 3.21. The EUV reflectivity

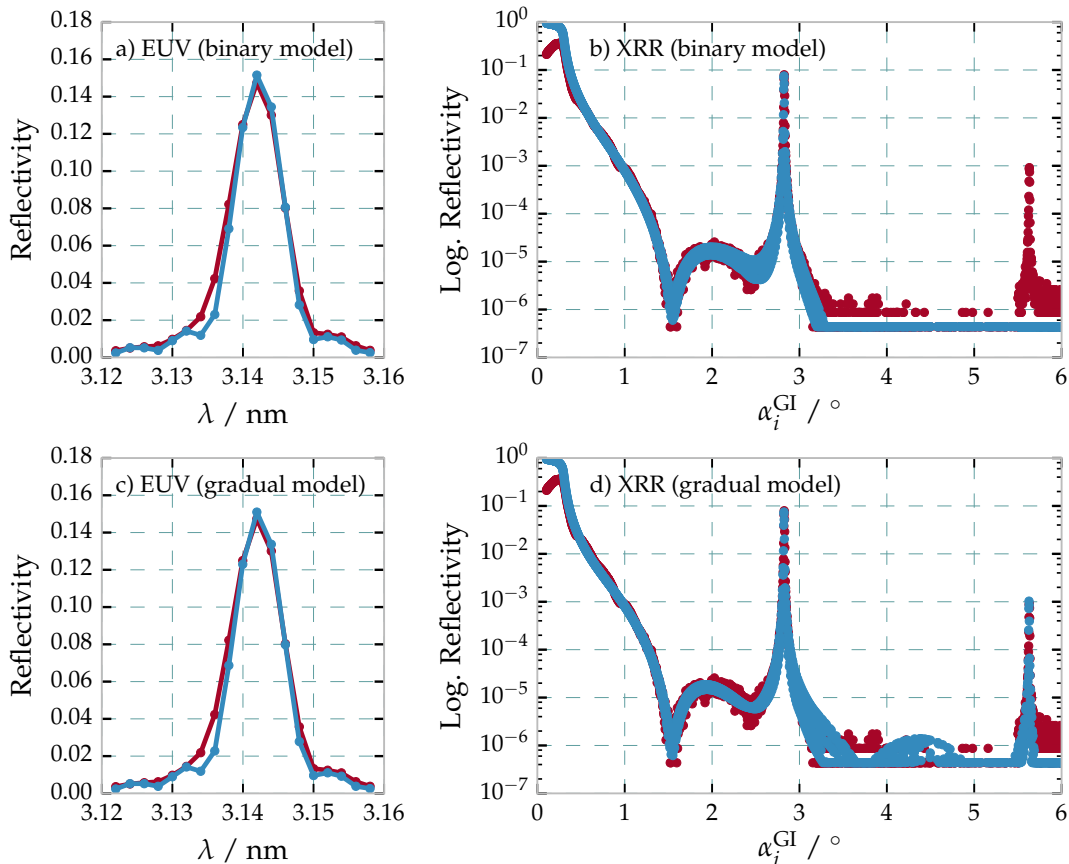


Figure 3.21 | Comparison of the reconstructions of both models for the EUV and XRR data. a) Measured EUV reflectivity curve for and near-normal angle of incidence of $\alpha_i = 1.5^\circ$ together with calculated curve of the PSO-based binary model reconstruction. b) Measured and calculated XRR curves for the same sample and model parameters at grazing angles of incidence using radiation at the Cu-K α wavelength. A clear mismatch of the theoretical curve and the measured data can be observed for the second Bragg peak between $\alpha_i^{\text{GI}} = 5.0^\circ$ and $\alpha_i^{\text{GI}} = 6.0^\circ$. c) Measured EUV reflectivity curve for and near-normal angle of incidence of $\alpha_i = 1.5^\circ$ together with calculated curve of the PSO-based gradual model reconstruction. d) Measured and calculated XRR curves for the same sample and model parameters at grazing angles of incidence using radiation at the Cu-K α wavelength.

curves show visually indistinguishable fits for both, the binary model as already found above and also the gradual model in Fig. 3.21a and Fig. 3.21c. For the binary model, we have seen the distinct mismatch with the second order Bragg peak, which is shown once

again in Fig. 3.21b. For the gradual interface model, we see a significant improvement of the optimized result with perfectly match in both Bragg peaks of the XRR curve in Fig. 3.21d while also maintaining an excellent agreement with the EUV curve.

Based on the example of a combined analysis of EUV and XRR data in this section, the gradual interface model clearly provides a more accurate representation of the physical reality in the sample than the binary approach by offering a reconstruction satisfying both data sets. At the same time, the results show that a verification of the model only becomes possible by adding complementary information. In case of the example above, that information is provided through the appearance of a second Bragg peak in the XRR curve. Thereby, the limiting case of the binary model, which is still possible for the new gradual model, can be excluded with certainty through the comparison shown in Fig. 3.21. The main difference of both models is the local gradual change of the index of refraction, which attributes for the fact that both materials can intermix. More importantly, both materials can intermix differently with respect to the specific interface, i.e. the situation where Cr is deposited on top of Sc or vice versa. A key element of obtaining a reconstruction of that particular model is thus the application of techniques, which can deliver information on the spacial distribution of the materials within one period.

At that point, it should be noted that other distortions of a perfect layer system can be imagined, which are not covered by a strictly periodic model as the one introduced above. Those include drifts of the period thickness D across the stack or other systematic aperiodicities. In that case, however, a broadening of the peak or a distortion of the peaks symmetry, most prominently in the EUV curve, would be observed, which is not the case. Although situations may occur, where the aperiodicities could lead to effects compensated by tuning the parameters of the gradual interface model, this assumption would assume a more complex situation than the simple assumption of periodicity and is thus implausible.

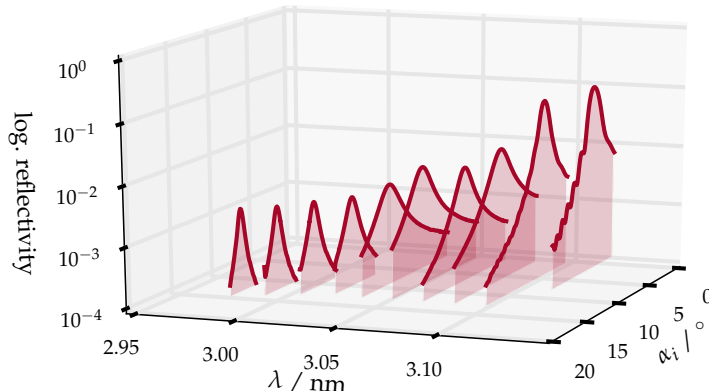
3.3.3 Addition of Complementary Experimental Methods

Due to the increased complexity of the model, the question arises how accurately any parameter of the model can be determined and whether correlations exist and can be resolved (cf. Fig. 3.11 as an example for correlated model parameters in case of Mo/Si multilayer systems) based on the available data and whether further analytical measurements can improve the result as this was clearly the result for the EUV and XRR experiments shown above. For the particular case of the gradual interface model for periodic multilayer systems with sub-nanometer layer thicknesses, in total four experiments were conducted with the goal to find a unequivocal reconstruction including low enough confidence intervals.

Resonant EUV Reflectivity

As seen for the four layer system discussed in Sec. 3.1, confidence intervals for the individual layer thicknesses in the range below 1 nm could not be obtained by exclusively analyzing the EUV curve. Similarly, the combined analysis of EUV and XRR experiments in Sec. 3.2.2 did improve the result but still shows fairly large confidence intervals concerning the small total layer thickness in the Cr/Sc systems. For the particular system discussed here with possibly strong interdiffusion, a technique is required that yields the total amount of Sc and equivalently Cr within a single period. For that purpose, resonant reflectivity experiments in the EUV spectral range are promising. The knowledge of the optical constants are a necessary requirement for deducting quantitative information from that kind of experiment. In case of Sc, those were measured precisely for the Sc L₃ and L₂ absorption edges at approximately $\lambda_{\text{Sc-L}} \approx 3.1 \text{ nm}$ and below by Aquila et al. [3]. The real and imaginary parts obtained from that experiments are shown together with the respective optical constants of Cr in Fig. 2.11 of Sec. 2.4.1 in Ch. 2. To exploit the information contained in the optical constants of Sc, angular resolved reflectivity curves across the first Bragg peak were recorded at several wavelengths across the Sc L-edge. As the Cr dispersion is changing only marginally and smoothly across that wavelength range, any change of contrast and absorption can be attributed to the Sc in the multilayer. The corresponding measurements are shown in Fig. 3.22. Each reflectivity curve was

Figure 3.22 | REUV



recorded within the interval from $\alpha_i = 2.5^\circ$ to $\alpha_i = 19.0^\circ$, depending on the selected wavelength. The wavelength range was chosen between $\lambda = 2.986 \text{ nm}$ and $\lambda = 3.128 \text{ nm}$ including the Sc L₂ and L₃ edges. The resulting data is analyzed in analogy to the EUV reflectivity curves in Sec. 3.3.2 by applying the matrix algorithm on basis of the gradual layer model and the optical constants by Aquila et al. [3]. The experimental uncertainties taken into account for the resonant extreme ultraviolet reflectivity (REUV) experiment were estimated on basis of the multilayer inhomogeneity deducted as described for the EUV experiment in Sec. 3.3.1. The details of the reconstruction based on this dataset are shown below in this section.

Grazing Incidence X-ray Fluorescence

In addition to the reconstruction of the Sc content via the REUV experiment, spacial resolved measurements are necessary to deduct the interface profile in the gradual layer model. As discussed in Sec. 3.3.2, asymmetric interface regions provide a possibility to observe a second Bragg peak in the XRR measurement, even though both layers in the period have equal nominal thickness. To obtain information on that spacial distribution of both materials within a period, XRF experiments exploiting the formation of a standing wave when scanning across the first Bragg peak were performed. The details of the method and how spacial sensitivity can be obtained are described in detail in Ch. 1, Sec. 1.5.

The sample was measured exciting the Sc and Cr K-lines, which show the highest fluorescence yield for the core shell transitions. The K-edges for both materials are at energies of $E_{\text{Sc-K}} = 4492 \text{ eV}$ and $E_{\text{Cr-K}} = 5989 \text{ eV}$ [28]. The experiment was therefore conducted at the FCM beamline in grazing incidence geometry at photon energies of $E_{\text{ph}} = 5500 \text{ eV}$ and $E_{\text{ph}} = 6250 \text{ eV}$, well above the respective edges as described in Ch. 2, Sec. 2.3. Depending on which energy was used, the Bragg peak is found at grazing angles of incidence of $\alpha_i^{\text{GI}} \approx 4.12^\circ$ and $\alpha_i^{\text{GI}} \approx 3.62^\circ$, respectively. The measured relative fluorescence yield in the vicinity of the first Bragg peak is shown in Fig. 3.23 for both photon energies and materials. Since the photon energy of $E_{\text{ph}} = 5500 \text{ eV}$ is below the

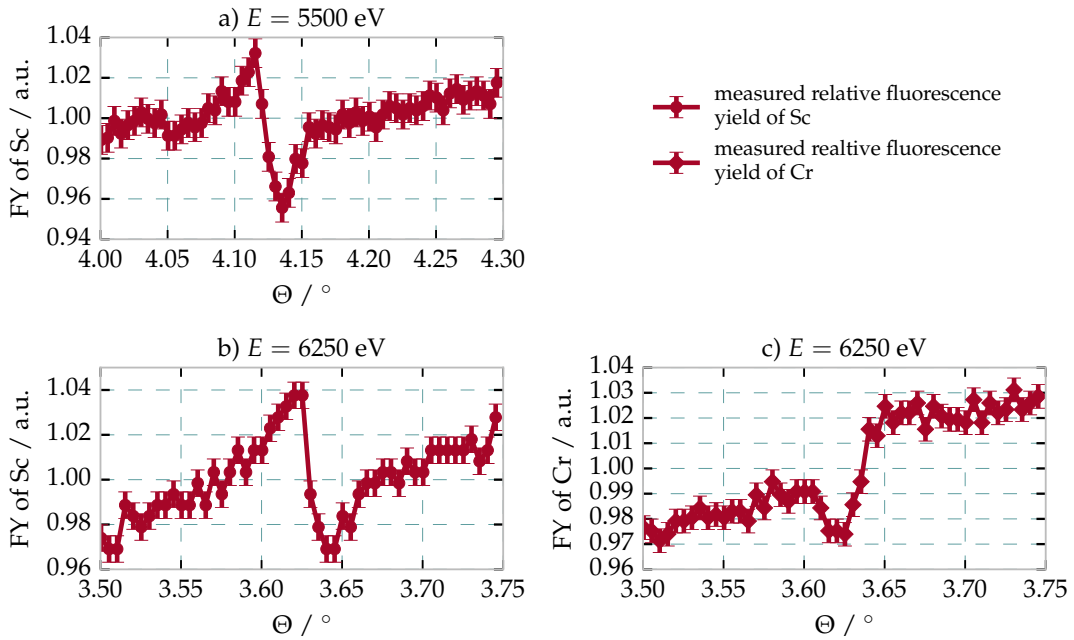


Figure 3.23 | XRF

K-edge of Cr, only data for the Sc K-fluorescence exists. In the second case, fluorescence from both materials was detected. The measurement uncertainties were estimated from the distribution of the data for regions away from the Bragg resonance.

The fluorescence curves for Cr and Sc show distinctly different behavior, of the expected s-curve-shape (cf. Fig. 1.7). For the analysis, the result at photon energies of $E_{\text{ph}} = 5500 \text{ eV}$ (Fig. 3.23a) was not taken into account, as the information is redundant to the result at $E_{\text{ph}} = 6250 \text{ eV}$ (Fig. 3.23b). As mentioned above, the theoretical description on how the relative fluorescence is calculated based on the gradual model is elaborated on in detail

in Ch. 2, Sec. 2.3.

3.3.4 Reconstruction and Maximum Likelihood Evaluation

With the two additional measurements described above, the total of four data sets (EUV, XRR, REUV and XRF) are available for the Cr/Sc multilayer sample to reconstruct the parameters of the gradual interface model. The full dataset is compiled in Fig. 3.24.

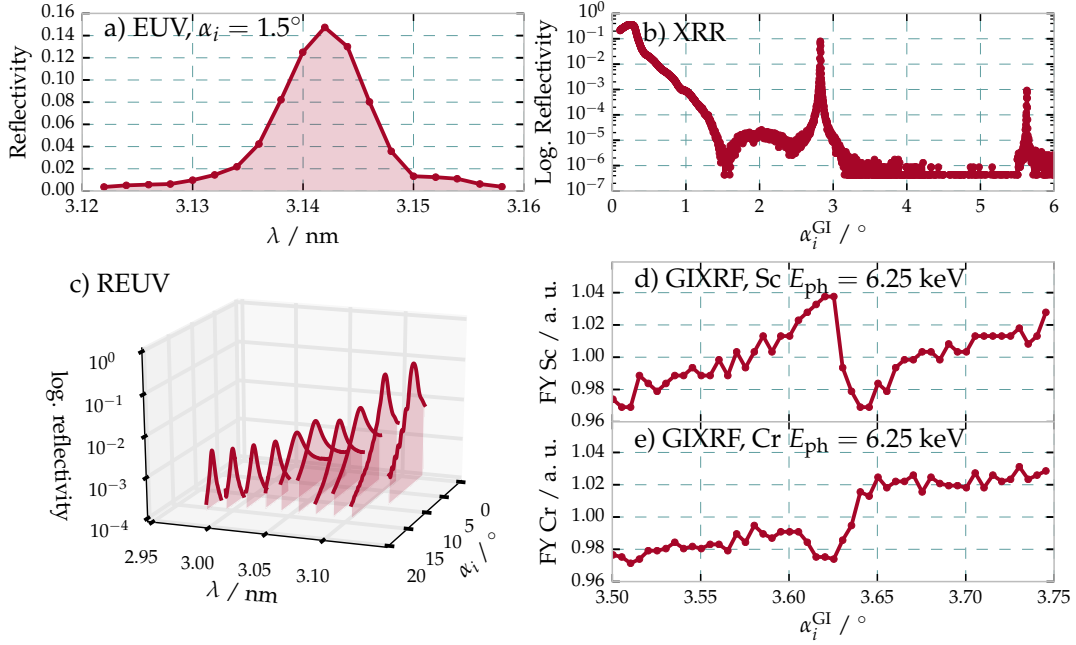


Figure 3.24 | All relevant data

As in the combined analysis conducted for the Mo/Si/C systems in Sec. 3.2.2, we define the minimization functional for the combined analysis of all the datasets as

$$\chi^2 = \tilde{\chi}_{\text{EUV}}^2 + \tilde{\chi}_{\text{XRR}}^2 + \tilde{\chi}_{\text{REUV}}^2 + \tilde{\chi}_{\text{GIXRF(Sc)}}^2 + \tilde{\chi}_{\text{GIXRF(Cr)}}^2, \quad (3.9)$$

where each of the reduced functionals is defined as

$$\tilde{\chi}^2 = \frac{1}{m-p} \left[\sum_m \frac{(I_m^{\text{model}} - I_m^{\text{meas}})^2}{\tilde{\sigma}_m^2} \right], \quad (3.10)$$

with m being the number of measurement points in each experiment and p the number of parameters for the model. Statistical and systematic uncertainties for each data point are included in $\tilde{\sigma}_m$. The definition of Eq. (3.9) ensures that all experiments are weighted equally considering their respective uncertainties. This functional corresponds to the combined χ^2 functional defined in (3.6), augmented by the additional measurements conducted here.

Firstly, similar as for the other two sample systems treated in this chapter, the parameters of the model, here the gradual interface model with the parameters and their limits listed in table 3.9, were first obtained using the PSO method to find a solution reproducing the experimental results. Secondly, following the maximum likelihood approach employing the MCMC method as detailed in Sec. 3.1.2, starting from this the uniqueness and confidence intervals for each parameter were obtained.

Parameter	Combined
D / nm	1.5737
Γ_{Sc}	0.48
s_d / nm	1.34
Γ_σ	0.16
η	0.56
σ_r / nm	0.11
ρ_{Sc}	0.94
ρ_{Cr}	0.98

Table 3.10 | Optimized model parameters obtained by PSO analysis

Through the minimization of the combined χ^2 functional in Eq. (3.9) via the PSO method, the best model parameters were obtained and are listed in table 3.10. The resulting theoretical curves are shown in comparison with the data from Fig. 3.24 including the respective uncertainties in Fig. 3.25. The data and the best model show

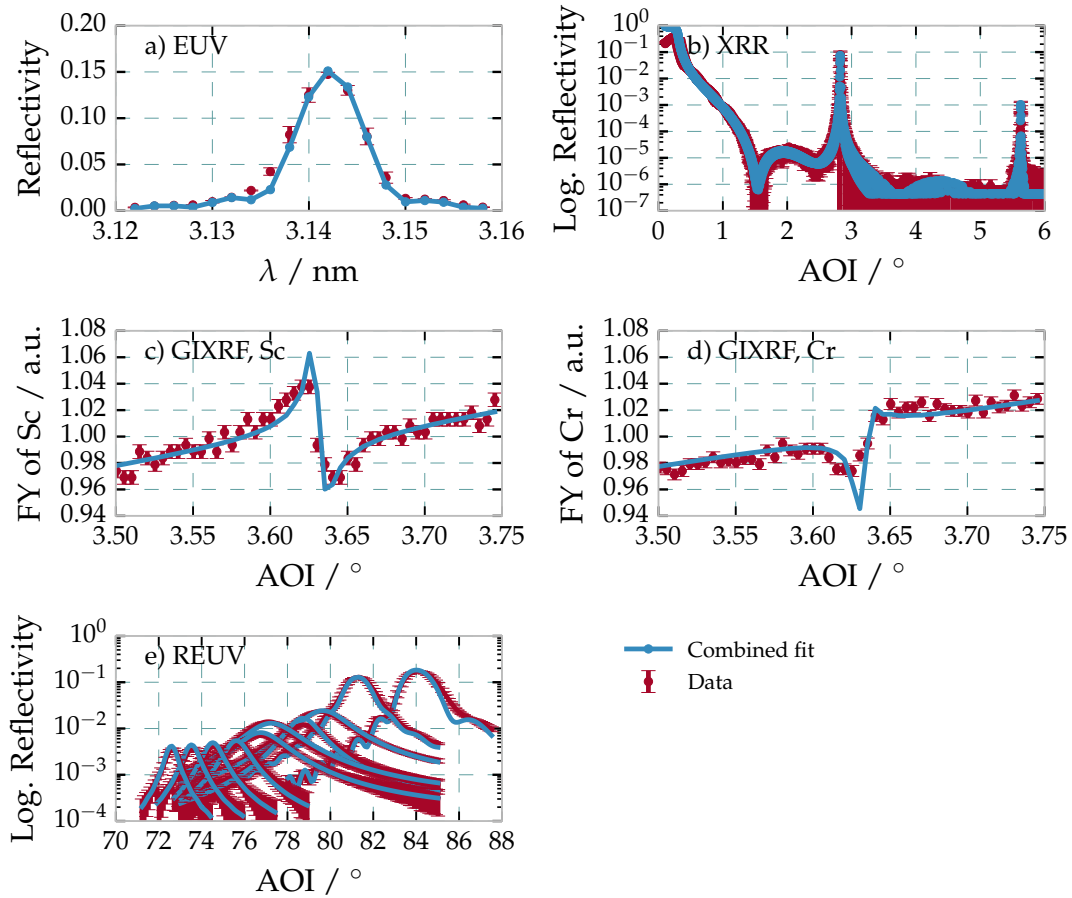


Figure 3.25 | Measured and calculated reflectance and intensity curves for the optimized parameters with the combined analysis of all experiments as listed in Table ??.

excellent agreement indicating that the gradual interface model as defined above indeed provides a very good representation of physical reality with respect to the experiments conducted here.

Table 3.11 | Optimized model parameters with confidence intervals derived from MCMC validation for each individual experiment and the combined analysis

Parameter	Combined	EUV	XRR	REUV	GIXRF
D / nm	$1.5737^{+0.0008}_{-0.0010}$	$1.5749^{+0.0014}_{-0.0022}$	$1.5726^{+0.0035}_{-0.0042}$	$1.5728^{+0.0016}_{-0.0019}$	$1.5741^{+0.0021}_{-0.0024}$
Γ_{Sc}	$0.48^{+0.04}_{-0.04}$	$0.35^{+0.14}_{-0.11}$	$0.42^{+0.35}_{-0.26}$	$0.52^{+0.09}_{-0.07}$	$0.49^{+0.09}_{-0.10}$
s_d / nm	$1.34^{+0.18}_{-0.26}$	$0.72^{+0.67}_{-0.66}$	$0.60^{+0.78}_{-0.57}$	$0.89^{+0.59}_{-0.83}$	$1.27^{+0.24}_{-0.38}$
Γ_σ	$0.16^{+0.51}_{-0.16}$	$0.29^{+0.64}_{-0.28}$	$0.40^{+0.57}_{-0.39}$	$0.33^{+0.61}_{-0.32}$	$0.39^{+0.57}_{-0.37}$
η	$0.56^{+0.06}_{-0.16}$	$0.44^{+0.16}_{-0.30}$	$0.38^{+0.33}_{-0.36}$	$0.52^{+0.14}_{-0.37}$	$0.37^{+0.25}_{-0.34}$
σ_r / nm	$0.11^{+0.11}_{-0.10}$	$0.17^{+0.12}_{-0.15}$	$0.13^{+0.14}_{-0.12}$	$0.17^{+0.16}_{-0.16}$	$0.27^{+0.20}_{-0.25}$
ρ_{Sc}	$0.94^{+0.05}_{-0.12}$	$0.84^{+0.15}_{-0.32}$	$0.78^{+0.21}_{-0.27}$	$0.94^{+0.06}_{-0.14}$	$0.83^{+0.17}_{-0.30}$
ρ_{Cr}	$0.98^{+0.02}_{-0.08}$	$0.96^{+0.04}_{-0.13}$	$0.83^{+0.16}_{-0.27}$	$0.90^{+0.09}_{-0.21}$	$0.86^{+0.14}_{-0.28}$

Confidence Intervals an Evaluation of the Experimental Methods

In order to assess the information content within each of the experimental methods, the PSO and MCMC analysis was conducted for each experiment individually and for the combination of all experiments. In the case of the XRR measurements, only the first and second Bragg peaks were considered for the combined analysis. The region in between mainly reflects the top surface layers, i.e. capping layers, and potential surface contamination layers, which were analyzed separately based exclusively on the XRR data. The results were added as fixed surface layers to the model for all theoretical calculations of all experiments (cf. model illustration in Fig. 3.15). The analysis of the XRF experiment was conducted based on the fluorescence data at an excitation photon energy of 6250 eV for the Sc-K and Cr-K lines by spectral deconvolution using detector response functions.

Consequently, in addition to fitting the data with a particle swarm optimizer, each result was verified based on the MCMC method described above to evaluate the confidence intervals for each parameter. The two step process, i.e. the PSO fitting procedure followed by the MCMC sampling, was conducted for each standalone experiment as well as for the combined optimization problem stated in Eq. (??). The results are compiled in Table 3.11. The confidence intervals were calculated by evaluating the probability distribution as a result of the MCMC procedure for each parameter around its PSO fit results. The confidence intervals given here represent percentiles of the number of samples found in the interval defined by the upper and lower bounds used for the PSO procedure for each parameter. In the case of a centered Gaussian distribution, percentiles of 2.3% and 97.8% of the integrated number of samples forming the distribution, mark the interval of four times the standard deviation, i.e. $\pm 2\sigma$ in statistical terms. Due to potential asymmetries in the actual distributions found by the MCMC method, explicit upper and lower bounds of the confidence intervals are given in Table 3.11 based on these percentiles. The best model value is based on the PSO fit result and is refined by the MCMC sampling by calculating the mean value, i.e. the 50% percentile, of the distribution of samples following the MCMC procedure. The best model is thus the result of a two-step optimization routine starting with a PSO analysis and sampling based on the resulting values to evaluate the distribution according to Eq. (??). The confidence intervals of each experimental method differ significantly depending on the parameter. To better demonstrate the different

Analysis of Cr/Sc Multilayers with Sub-nanometer Layer Thickness

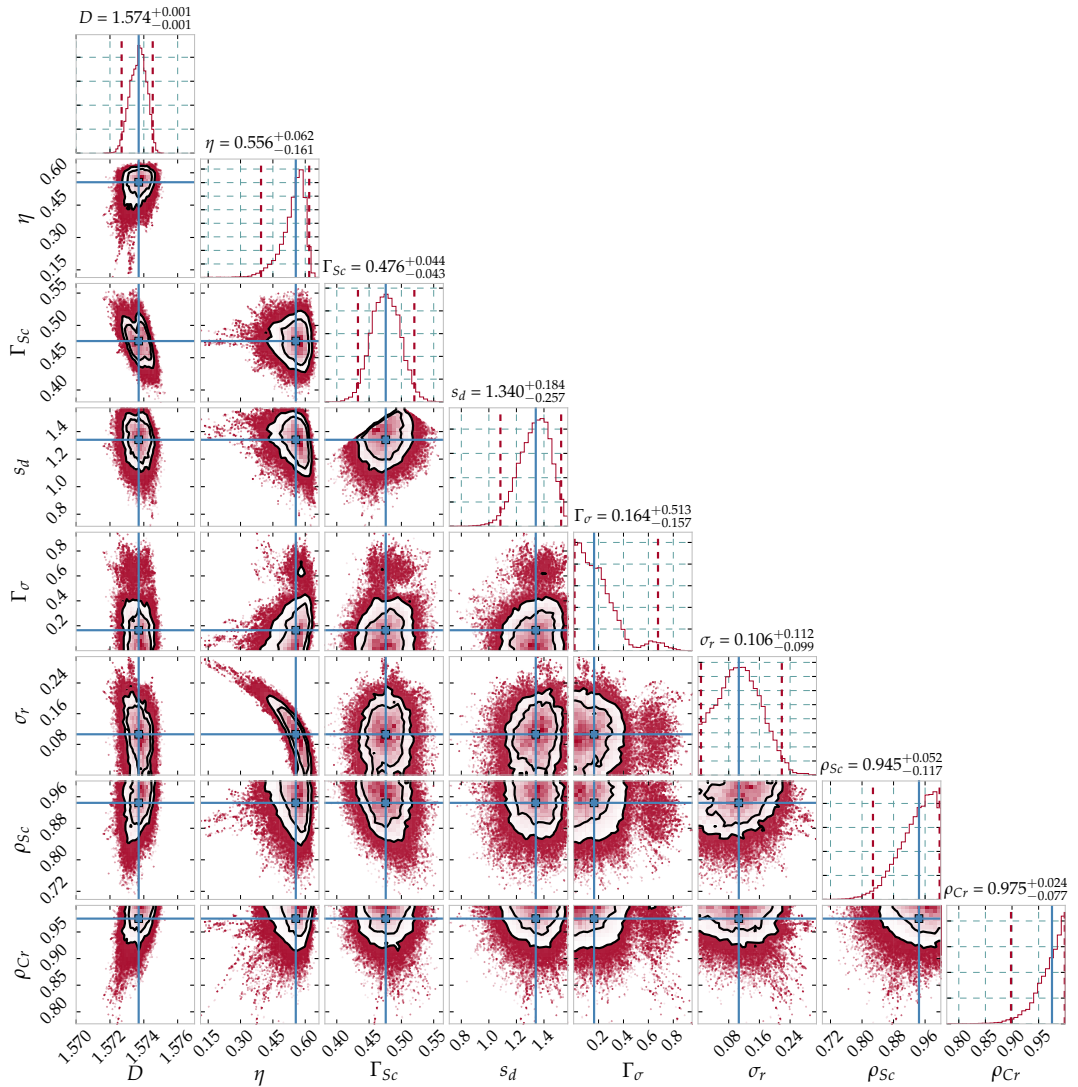
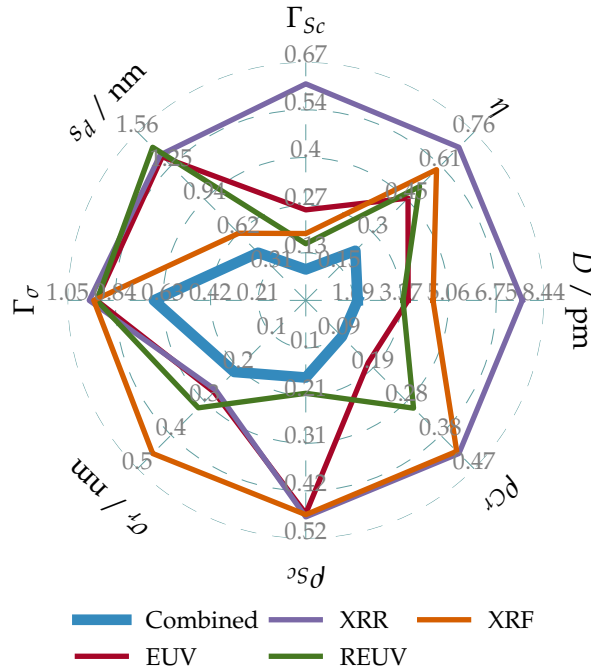


Figure 3.26 | Cornerplot

CHARACTERIZATION OF THE MULTILAYER STRUCTURE FOR DIFFERENT SYSTEMS

sensitivities for the model parameters depending on the experimental method, we have illustrated each confidence interval in Fig. 3.27. It is worth noting that the confidence

Figure 3.27 | Visual representation of the total confidence intervals for each of the parameters with respect to each of the individual experiments as well as the combined analysis.



interval for the combined analysis is significantly smaller compared to the individual experiments. This is especially true for the parameter Γ_σ describing the asymmetry of the interdiffusion layers. Within each of the individual experiments this parameter has a large uncertainty, whereas the combined analysis delivers a significant result of a clearly asymmetric interdiffusion layer thickness.

The best fit result based on the two-step optimization procedure of the combined data set of all experiments is shown in Fig. ?? together with the experimental data. The theoretical calculations based on the above model and the experimental data show good agreement. Nevertheless, differences can be observed. The reason lies in the fact that the model is potentially still too ideal. Small variations during the deposition process, for example, could lead to imperfections, which are not described in a strictly periodic model. However, including these by explicitly breaking the periodicity would again lead to an ill-defined model with a vastly increased number of parameters and is thus not practical. Another reason is the deviation in the homogeneity of the sample, e.g. a varying period across the sample, which cause mismatches if the measurement position varies slightly between the different experimental setups. The latter effects were considered in the uncertainties of the individual measurements by measuring the EUV reflectivity at positions ± 2 mm from the center position and fitting the model. The result was a $\Delta D = 2$ pm shift in the period over 4 mm across the sample.

The resulting depth dependence of the index of refraction is shown in Fig. 3.28 together with the initial binary model for comparison. The most remarkable result of the combined

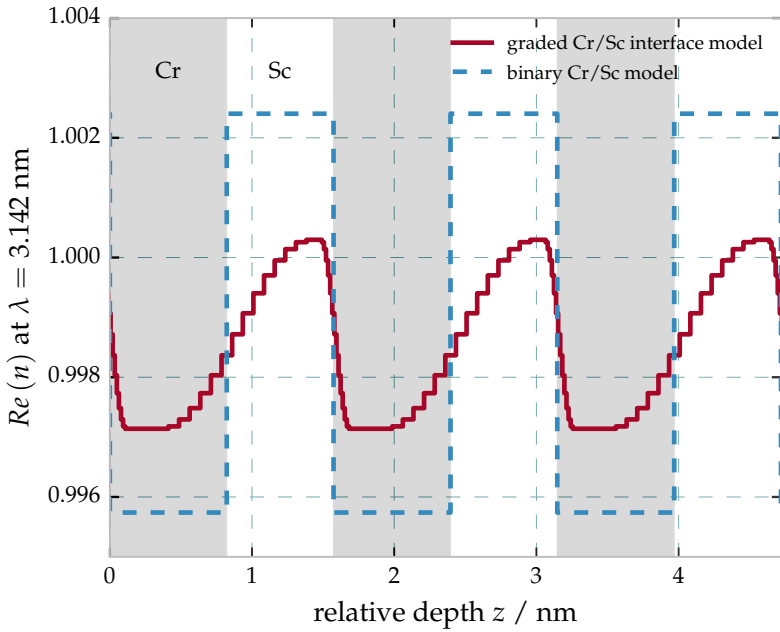
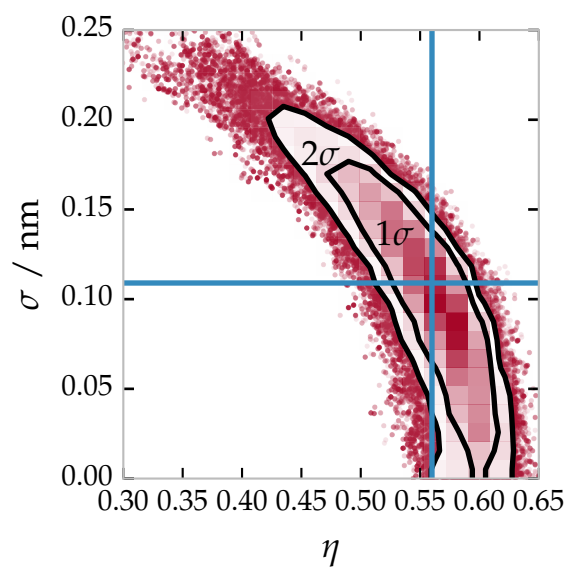


Figure 3.28 | Real part of the index of refraction n based on the results of the optimized parameters listed in Table 3.11 for the combined analysis for a selected wavelength. The gradual interface model is shown in direct comparison to the binary model optimized for the EUV reflectance curve over three full periods. The resulting strong asymmetry in the width of the interface regions is clearly visible (see text). The gray and white shaded areas indicate the Cr and Sc layers, respectively, for the binary model.

analysis is the strong asymmetry of the interdiffusion layers. This can only be shown by the combination of all analytical experiments conducted here, as can be seen from the confidence intervals in Fig. 3.27 as well as the values in Table 3.11. A possible explanation for this asymmetry is the deposition process through magnetron sputtering. The elements Cr and Sc have different mass and thus different momentum when deposited onto each other. A similar effect is known from the deposition of Mo/Si multilayer systems, where the heavier Mo shows higher penetration into the Si layer than vice versa [59]. In the case of Cr/Sc multilayers, the Cr is heavier and thus has higher momentum leading to a broader interdiffusion layer. The validation using the MCMC procedure also yields possible correlations between single parameters of the model. [35]

Figure 3.29 | CrSc eta rho correlation



References

- [1] M. Abramowitz and I. A. Stegun: *Handbook of Mathematical Functions: With Formulas, Graphs, and Mathematical Tables*. en. Courier Corporation, 1964.
- [2] J. Als-Nielsen and D. McMorrow: 'X-rays and their interaction with matter'. en. In: *Elements of Modern X-ray Physics*. John Wiley & Sons, Inc., 2011, pp. 1–28.
- [3] A. L. Aquila, F. Salmassi, E. M. Gullikson, F. Eriksson and J. Birch: 'Measurements of the optical constants of scandium in the 50–1300eV range'. In: vol. 5538. 2004, pp. 64–71. DOI: 10.1117/12.563615.
- [4] S. Bajt, D. G. Stearns and P. A. Kearney: 'Investigation of the amorphous-to-crystalline transition in Mo/Si multilayers'. In: *Journal of Applied Physics* **90**.2 (2001), pp. 1017–1025. DOI: <http://dx.doi.org/10.1063/1.1381559>.
- [5] A. Balerna and S. Mobilio: 'Introduction to Synchrotron Radiation'. en. In: *Synchrotron Radiation*. Ed. by S. Mobilio, F. Boscherini and C. Meneghini. DOI: 10.1007/978-3-642-55315-8_1. Springer Berlin Heidelberg, 2015, pp. 3–28.
- [6] M. Bayes and M. Price: 'An Essay towards Solving a Problem in the Doctrine of Chances. By the Late Rev. Mr. Bayes, F. R. S. Communicated by Mr. Price, in a Letter to John Canton, A. M. F. R. S.' en. In: *Philosophical Transactions* **53** (1763), pp. 370–418. DOI: 10.1098/rstl.1763.0053.
- [7] B. Beckhoff, A. Gottwald, R. Klein, M. Krumrey, R. Müller, M. Richter, F. Scholze, R. Thornagel and G. Ulm: 'A quarter-century of metrology using synchrotron radiation by PTB in Berlin'. In: *physica status solidi (b)* **246**.7 (2009), pp. 1415–1434. DOI: 10.1002/pssb.200945162.
- [8] F. d. Bergevin: 'The Interaction of X-Rays (and Neutrons) with Matter'. en. In: *X-ray and Neutron Reflectivity*. Ed. by J. Daillant and A. Gibaud. Lecture Notes in Physics 770. DOI: 10.1007/978-3-540-88588-7_1. Springer Berlin Heidelberg, 2009, pp. 1–57.
- [9] R. T. Birge: 'The Calculation of Errors by the Method of Least Squares'. In: *Physical Review* **40**.2 (1932), pp. 207–227. DOI: 10.1103/PhysRev.40.207.
- [10] D. K. G. d. Boer, A. J. G. Leenaers and W. W. v. d. Hoogenhof: 'Influence of roughness profile on reflectivity and angle-dependent X-ray fluorescence'. In: *J. Phys. III France* **4**.9 (1994), pp. 1559–1564. DOI: 10.1051/jp3:1994222.
- [11] D. K. G. de Boer: 'Glancing-incidence x-ray fluorescence of layered materials'. In: *Physical Review B* **44**.2 (1991), pp. 498–511. DOI: 10.1103/PhysRevB.44.498.
- [12] D. K. G. de Boer: 'X-ray reflection and transmission by rough surfaces'. In: *Phys. Rev. B* **51**.8 (1995), pp. 5297–5305. DOI: 10.1103/PhysRevB.51.5297.

References

- [13] D. K. G. de Boer: 'X-ray scattering and x-ray fluorescence from materials with rough interfaces'. In: *Phys. Rev. B* **53**.10 (1996), pp. 6048–6064. DOI: 10.1103/PhysRevB.53.6048.
- [14] R. Bonifacio, C. Pellegrini and L. M. Narducci: 'Collective instabilities and high-gain regime in a free electron laser'. In: *Optics Communications* **50**.6 (1984), pp. 373–378. DOI: 10.1016/0030-4018(84)90105-6.
- [15] M. Born and E. Wolf: *Principles of Optics*. 3rd ed. Cambridge University Press, 1965.
- [16] G. Brandt, J. Eden, R. Fliegauf, A. Gottwald, A. Hoehl, R. Klein, R. Müller, M. Richter, F. Scholze, R. Thornagel, G. Ulm, K. Bürkmann, J. Rahn and G. Wüstefeld: 'The Metrology Light Source – The new dedicated electron storage ring of PTB'. In: *Nuclear Instruments and Methods in Physics Research Section B: Beam Interactions with Materials and Atoms* **258**.2 (2007), pp. 445–452. DOI: 10.1016/j.nimb.2007.02.076.
- [17] S. Braun, H. Mai, M. Moss, R. Scholz and A. Leson: 'Mo/Si Multilayers with Different Barrier Layers for Applications as Extreme Ultraviolet Mirrors'. en. In: *Japanese Journal of Applied Physics* **41**.6S (2002), p. 4074. DOI: 10.1143/JJAP.41.4074.
- [18] A. Carlisle and G. Dozier: 'An off-the-shelf PSO'. In: *Proceedings of The Workshop On particle Swarm Optimization, Indianapolis, USA*. 2001.
- [19] D. R. Cox and D. V. Hinkley: *Theoretical Statistics*. en. CRC Press, 1979.
- [20] J. W. Criss and L. S. Birks: 'Calculation methods for fluorescent x-ray spectrometry. Empirical coefficients versus fundamental parameters'. In: *Analytical Chemistry* **40**.7 (1968), pp. 1080–1086. DOI: 10.1021/ac60263a023.
- [21] Croce, P. and Nérot, L.: 'Étude des couches minces et des surfaces par réflexion rasante, spéculaire ou diffuse, de rayons X'. In: *Rev. Phys. Appl. (Paris)* **11**.1 (1976), pp. 113–125. DOI: 10.1051/rphysap:01976001101011300.
- [22] J. Daillant, S. Mora and A. Sentenac: 'Diffuse Scattering'. en. In: *X-ray and Neutron Reflectivity*. Ed. by J. Daillant and A. Gibaud. Lecture Notes in Physics 770. DOI: 10.1007/978-3-540-88588-7_4. Springer Berlin Heidelberg, 2009, pp. 133–182.
- [23] J. Daillant, A. Gibaud, W. Beiglböck, J. Ehlers, K. Hepp, H. A. Weidenmüller, R. Beig, W. Domcke, B.-G. Englert, U. Frisch, P. Hänggi, G. Hasinger, W. Hillebrandt, R. L. Jaffe, W. Janke, H. v. Löhneysen, M. Mangano, J.-M. Raimond, D. Sornette, S. Theisen, W. Weise, J. Zittartz, F. Guinea and D. Vollhardt, eds.: *X-ray and Neutron Reflectivity*. Vol. 770. Lecture Notes in Physics. Berlin, Heidelberg: Springer Berlin Heidelberg, 2009.
- [24] D. A. G. Deacon, L. R. Elias, J. M. J. Madey, G. J. Ramian, H. A. Schwettman and T. I. Smith: 'First Operation of a Free-Electron Laser'. In: *Physical Review Letters* **38**.16 (1977), pp. 892–894. DOI: 10.1103/PhysRevLett.38.892.
- [25] Y. S. Derbenev, A. M. Kondratenko and E. L. Saldin: 'On the possibility of using a free electron laser for polarization of electrons in storage rings'. In: *Nuclear Instruments and Methods in Physics Research* **193**.3 (1982), pp. 415–421. DOI: 10.1016/0029-554X(82)90233-6.
- [26] B. N. Dev, A. K. Das, S. Dev, D. W. Schubert, M. Stamm and G. Materlik: 'Resonance enhancement of x rays in layered materials: Application to surface enrichment in polymer blends'. In: *Physical Review B* **61**.12 (2000), pp. 8462–8468. DOI: 10.1103/PhysRevB.61.8462.

- [27] P. a. M. Dirac: 'A new notation for quantum mechanics'. In: *Mathematical Proceedings of the Cambridge Philosophical Society* **35**.3 (1939), pp. 416–418. doi: 10.1017/S0305004100021162.
- [28] W. T. Elam, B. D. Ravel and J. R. Sieber: 'A new atomic database for X-ray spectroscopic calculations'. In: *Radiation Physics and Chemistry* **63**.2 (2002), pp. 121–128. doi: 10.1016/S0969-806X(01)00227-4.
- [29] D. Foreman-Mackey, D. W. Hogg, D. Lang and J. Goodman: 'emcee: The MCMC Hammer'. In: *Publications of the Astronomical Society of the Pacific* **125**.925 (2013). arXiv: 1202.3665, pp. 306–312. doi: 10.1086/670067.
- [30] C. F. Gauss: *Theoria motus corporum coelestium in sectionibus conicis solem ambientium*. en. 1809.
- [31] S. K. Ghose and B. N. Dev: 'X-ray standing wave and reflectometric characterization of multilayer structures'. In: *Physical Review B* **63**.24 (2001), p. 245409. doi: 10.1103/PhysRevB.63.245409.
- [32] A. Gibaud and G. Vignaud: 'Specular Reflectivity from Smooth and Rough Surfaces'. en. In: *X-ray and Neutron Reflectivity*. Ed. by J. Daillant and A. Gibaud. Lecture Notes in Physics 770. DOI: 10.1007/978-3-540-88588-7_3. Springer Berlin Heidelberg, 2009, pp. 85–131.
- [33] J. Goodman and J. Weare: 'Ensemble samplers with affine invariance'. en. In: *Communications in Applied Mathematics and Computational Science* **5**.1 (2010), pp. 65–80. doi: 10.2140/camcos.2010.5.65.
- [34] E. M. Gullikson and D. G. Stearns: 'Asymmetric extreme ultraviolet scattering from sputter-deposited multilayers'. In: *Phys. Rev. B* **59**.20 (1999), pp. 13273–13277. doi: 10.1103/PhysRevB.59.13273.
- [35] A. Haase, S. Bajt, P. Hönicke, V. Soltwisch and F. Scholze: 'Multiparameter characterization of subnanometre Cr/Sc multilayers based on complementary measurements'. en. In: *Journal of Applied Crystallography* **49**.6 (2016), pp. 2161–2171. doi: 10.1107/S1600576716015776.
- [36] A. Haase, V. Soltwisch, S. Braun, C. Laubis and F. Scholze: 'Interface Morphology of Mo/Si Multilayer Systems with Varying Mo Layer Thickness Studied by EUV Diffuse Scattering'. In: *Optics Express* (2017).
- [37] A. Haase, V. Soltwisch, C. Laubis and F. Scholze: 'Role of dynamic effects in the characterization of multilayers by means of power spectral density'. In: *Appl. Opt.* **53**.14 (2014), pp. 3019–3027. doi: 10.1364/AO.53.003019.
- [38] A. Haase, V. Soltwisch, F. Scholze and S. Braun: 'Characterization of Mo/Si mirror interface roughness for different Mo layer thickness using resonant diffuse EUV scattering'. In: *Proc. SPIE*. Vol. 9628. 2015, pages. doi: 10.1117/12.2191265.
- [39] B. L. Henke, E. M. Gullikson and J. C. Davis: 'X-Ray Interactions: Photoabsorption, Scattering, Transmission, and Reflection at E = 50–30,000 eV, Z = 1–92'. In: *Atomic Data and Nuclear Data Tables* **54**.2 (1993), pp. 181–342. doi: <http://dx.doi.org/10.1006/adnd.1993.1013>.
- [40] M. P. Hobson and J. E. Baldwin: 'Markov-chain Monte Carlo approach to the design of multilayer thin-film optical coatings'. EN. In: *Applied Optics* **43**.13 (2004), pp. 2651–2660. doi: 10.1364/AO.43.002651.

References

- [41] V. Holý and T. Baumbach: 'Nonspecular X-ray reflection from rough multilayers'. In: *Phys. Rev. B* **49**.15 (1994), pp. 10668–10676. DOI: 10.1103/PhysRevB.49.10668.
- [42] V. Holý, J. Kuběna, I. Ohlídal, K. Lischka and W. Plotz: 'X-ray reflection from rough layered systems'. In: *Phys. Rev. B* **47**.23 (1993), pp. 15896–15903. DOI: 10.1103/PhysRevB.47.15896.
- [43] J. Kennedy: 'Particle Swarm Optimization'. en. In: *Encyclopedia of Machine Learning*. Ed. by C. Sammut and G. I. Webb. DOI: 10.1007/978-0-387-30164-8_630. Springer US, 2011, pp. 760–766.
- [44] H. Kiessig: 'Interferenz von Röntgenstrahlen an dünnen Schichten'. In: *Annalen der Physik* **402**.7 (1931), pp. 769–788. DOI: 10.1002/andp.19314020702.
- [45] M. Krumrey: 'Design of a Four-Crystal Monochromator Beamline for Radiometry at BESSY II'. en. In: *Journal of Synchrotron Radiation* **5**.1 (1998), pp. 6–9. DOI: 10.1107/S0909049597011825.
- [46] L. D. Landau and E.M. Lifshitz: *Electrodynamics of Continuous Media*. A Course of Theoretical Physics 8. Oxford, London, New York, Paris: Pergamon Press, 1960.
- [47] A.-M. Legendre: *Nouvelles méthodes pour la détermination des orbites des comètes*. fr. F. Didot, 1805.
- [48] K. Levenberg: 'A method for the solution of certain non-linear problems in least square'. In: *Quarterly of Applied Mathematics* (1944).
- [49] Y. Lim, T. Westerwalbesloh, A. Aschentrup, O. Wehmeyer, G. Haindl, U. Kleineberg and U. Heinzmann: 'Fabrication and characterization of EUV multilayer mirrors optimized for small spectral reflection bandwidth'. In: *Applied Physics A* **72**.1 (2001), pp. 121–124. DOI: 10.1007/s003390000723.
- [50] H. A. Lorentz: 'The theorem of Poynting concerning the energy in the electromagnetic field and two general propositions concerning the propagation of light'. In: *Amsterdammer Akademie der Wetenschappen* **4** (1896), p. 176.
- [51] J. Lubeck, B. Beckhoff, R. Fliegauf, I. Holfelder, P. Hönicke, M. Müller, B. Polakowski, F. Reinhardt and J. Weser: 'A novel instrument for quantitative nanoanalytics involving complementary X-ray methodologies'. In: *Review of Scientific Instruments* **84**.4 (2013), p. 045106. DOI: 10.1063/1.4798299.
- [52] J. M. J. Madey: 'Stimulated Emission of Bremsstrahlung in a Periodic Magnetic Field'. In: *Journal of Applied Physics* **42**.5 (1971), pp. 1906–1913. DOI: 10.1063/1.1660466.
- [53] D. W. Marquardt: 'An algorithm for least-squares estimation of nonlinear parameters'. In: *Journal of the society for Industrial and Applied Mathematics* **11**.2 (1963), pp. 431–441.
- [54] P. Mikulík: 'X-ray reflectivity from planar and structured multilayers'. PhD thesis. Thèse de l'Université Joseph Fourier, 1997.
- [55] J. S. Milton and J. C. Arnold: *Introduction to Probability and Statistics: Principles and Applications for Engineering and the Computing Sciences*. 4th. New York, NY, USA: McGraw-Hill, Inc., 2002.

- [56] S. V. Milton, E. Gluskin, N. D. Arnold, C. Benson, W. Berg, S. G. Biedron, M. Borland, Y.-C. Chae, R. J. Dejus, P. K. D. Hartog et al.: 'Exponential Gain and Saturation of a Self-Amplified Spontaneous Emission Free-Electron Laser'. en. In: *Science* **292**.5524 (2001), pp. 2037–2041. doi: 10.1126/science.1059955.
- [57] I. H. MUNRO and G. V. MARR: 'CHAPTER 1 - SYNCHROTRON RADIATION SOURCES'. In: *Handbook on Synchrotron Radiation*. Handbook on Synchrotron Radiation. Amsterdam: Elsevier, 1987, pp. 1–20.
- [58] Névot, L. and Croce, P.: 'Caractérisation des surfaces par réflexion rasante de rayons X. Application à l'étude du polissage de quelques verres silicates'. In: *Rev. Phys. Appl. (Paris)* **15**.3 (1980), pp. 761–779. doi: 10.1051/rphysap:01980001503076100.
- [59] A. K. Petford-Long, M. B. Stearns, C.-H. Chang, S. R. Nutt, D. G. Stearns, N. M. Ceglio and A. M. Hawryluk: 'High-resolution electron microscopy study of x-ray multilayer structures'. In: *Journal of Applied Physics* **61**.4 (1987), pp. 1422–1428. doi: <http://dx.doi.org/10.1063/1.338122>.
- [60] U. Pietsch, V. Holý and T. Baumbach: *High-Resolution X-Ray Scattering From Thin Films to Lateral Nanostructures*. Springer, 2004.
- [61] M. Prasciolu, A. Haase, F. Scholze, H. N. Chapman and S. Bajt: 'Extended asymmetric-cut multilayer X-ray gratings'. EN. In: *Optics Express* **23**.12 (2015), pp. 15195–15204. doi: 10.1364/OE.23.015195.
- [62] M. Prasciolu, A. F. G. Leontowich, K. R. Beyerlein and S. Bajt: 'Thermal stability studies of short period Sc/Cr and Sc/B₄C/Cr multilayers'. In: *Appl. Opt.* **53**.10 (2014), pp. 2126–2135. doi: 10.1364/AO.53.002126.
- [63] S. D. Rasberry and K. F. J. Heinrich: 'Calibration for interelement effects in x-ray fluorescence analysis'. In: *Analytical Chemistry* **46**.1 (1974), pp. 81–89. doi: 10.1021/ac60337a027.
- [64] R. M. Rousseau: 'Fundamental algorithm between concentration and intensity in XRF analysis 1—theory'. en. In: *X-Ray Spectrometry* **13**.3 (1984), pp. 115–120. doi: 10.1002/xrs.1300130306.
- [65] F. Scholze, B. Beckhoff, G. Brandt, R. Fliegauf, A. Gottwald, R. Klein, B. Meyer, U. D. Schwarz, R. Thornagel, J. Tuemmler, K. Vogel, J. Weser and G. Ulm: 'High-accuracy EUV metrology of PTB using synchrotron radiation'. In: *Proc. SPIE*. Vol. 4344. 2001, pp. 402–413. doi: 10.1117/12.436766.
- [66] J. Schwinger: 'On the Classical Radiation of Accelerated Electrons'. In: *Physical Review* **75**.12 (1949), pp. 1912–1925. doi: 10.1103/PhysRev.75.1912.
- [67] J. Sherman: 'The theoretical derivation of fluorescent X-ray intensities from mixtures'. In: *Spectrochimica Acta* **7** (1955), pp. 283–306. doi: 10.1016/0371-1951(55)80041-0.
- [68] T. Shiraiwa and N. Fujino: 'Theoretical Calculation of Fluorescent X-Ray Intensities in Fluorescent X-Ray Spectrochemical Analysis.' en. In: *Japanese Journal of Applied Physics* **5**.10 (1966), p. 886. doi: 10.1143/JJAP.5.886.
- [69] S. K. Sinha, E. B. Sirota, S. Garoff and H. B. Stanley: 'X-ray and neutron scattering from rough surfaces'. In: *Phys. Rev. B* **38**.4 (1988), pp. 2297–2311. doi: 10.1103/PhysRevB.38.2297.

References

- [70] V. Soltwisch, A. Haase, J. Wernecke, J. Probst, M. Schoengen, S. Burger, M. Krumrey and F. Scholze: 'Correlated diffuse x-ray scattering from periodically nanostructured surfaces'. In: *Physical Review B* **94**.3 (2016), p. 035419. doi: 10.1103/PhysRevB.94.035419.
- [71] V. Soltwisch, A. Fischer, C. Laubis, C. Stadelhoff, F. Scholze and A. Ullrich: 'Polarization resolved measurements with the new EUV ellipsometer of PTB'. In: *Proc. SPIE*. Vol. 9422. 2015, pp. 942213–7. doi: 10.1117/12.2085798.
- [72] E. Spiller, D. Stearns and M. Krumrey: 'Multilayer X-ray mirrors: Interfacial roughness, scattering, and image quality'. In: *Journal of applied physics* **74**.1 (1993), pp. 107–118.
- [73] D. G. Stearns: 'X-ray scattering from interfacial roughness in multilayer structures'. In: *Journal of Applied Physics* **71**.9 (1992), pp. 4286–4298. doi: 10.1063/1.350810.
- [74] D. G. Stearns, R. S. Rosen and S. P. Vernon: 'Fabrication of high-reflectance Mo-Si multilayer mirrors by planar-magnetron sputtering'. en. In: *Journal of Vacuum Science & Technology A: Vacuum, Surfaces, and Films* **9**.5 (1991), pp. 2662–2669. doi: 10.1116/1.577221.
- [75] A. C. Thompson and D. Vaughan, eds.: *X-ray Data Booklet*. Second. Lawrence Berkeley National Laboratory, University of California, 2001.
- [76] R. Thornagel, R. Klein and G. Ulm: 'The electron storage ring BESSY II as a primary source standard from the visible to the the X-ray range'. en. In: *Metrologia* **38**.5 (2001), p. 385. doi: 10.1088/0026-1394/38/5/3.
- [77] J. Tummeler, H. Blume, G. Brandt, J. Eden, B. Meyer, H. Scherr, F. Scholz, F. Scholze and G. Ulm: 'Characterization of the PTB EUV reflectometry facility for large EUVL optical components'. In: *Proc. SPIE* **5037** (2003), pp. 265–273. doi: 10.1117/12.482668.
- [78] J. Verhoeven, L. Chunguang, E. J. Puik, M. J. van der Wiel and T. P. Huijgen: 'Ion beam modification of Mo?Si multilayer systems for X-ray reflection'. In: *Applied Surface Science* **55**.2 (1992), pp. 97–103. doi: 10.1016/0169-4332(92)90099-J.
- [79] B. Vidal and P. Vincent: 'Metallic multilayers for x rays using classical thin-film theory'. en. In: *Applied Optics* **23**.11 (1984), p. 1794. doi: 10.1364/AO.23.001794.
- [80] S. N. Yakunin, I. A. Makhotkin, K. V. Nikolaev, R. W. E. v. d. Kruijs, M. A. Chuev and F. Bijkerk: 'Combined EUV reflectance and X-ray reflectivity data analysis of periodic multilayer structures'. In: *Opt. Express* **22**.17 (2014), pp. 20076–20086. doi: 10.1364/OE.22.020076.

Danksagung

Danke!

Eidesstattliche Versicherung

Hiermit versichere ich an Eides statt, dass ich die vorliegende Arbeit selbstständig verfasst und keine anderen als die in der Dissertation angegebenen Quellen und Hilfsmittel benutzt habe. Alle Ausführungen, die anderen veröffentlichten oder nicht veröffentlichten Schriften wörtlich oder sinngemäß entnommen wurden, habe ich kenntlich gemacht. Die Darstellung des Eigenanteils an bereits publizierten Inhalten in meiner beigefügten Erklärung ist zutreffend.

Es gab keine Zusammenarbeit mit anderen wissenschaftlichen Mitarbeitern, die ein Promotionsverfahren anstreben.

Berlin, den 31. März 2017

Anton Haase

Erklärung

Es wurden bereits Teile der Dissertation veröffentlicht.

Liste der Veröffentlichungen, welche in die Dissertation eingeflossen sind:

- 1) A. Haase, V. Soltwisch, C. Laubis und F. Scholze: „Role of dynamic effects in the characterization of multilayers by means of power spectral density“. In: *Appl. Opt.* **53**.14 (2014), S. 3019–3027. DOI: 10.1364/AO.53.003019
- 2) A. Haase, V. Soltwisch, F. Scholze und S. Braun: „Characterization of Mo/Si mirror interface roughness for different Mo layer thickness using resonant diffuse EUV scattering“. In: *Proc. SPIE*. Bd. 9628. 2015, pages. DOI: 10.1117/12.2191265
- 3) A. Haase, S. Bajt, P. Hönigke, V. Soltwisch und F. Scholze: „Multiparameter characterization of subnanometre Cr/Sc multilayers based on complementary measurements“. en. In: *Journal of Applied Crystallography* **49**.6 (Dez. 2016), S. 2161–2171. DOI: 10.1107/S1600576716015776
- 4) A. Haase, V. Soltwisch, S. Braun, C. Laubis und F. Scholze: „Interface Morphology of Mo/Si Multilayer Systems with Varying Mo Layer Thickness Studied by EUV Diffuse Scattering“. In: *Optics Express* (2017)

Liste der Veröffentlichungen, welche nicht in die Dissertation eingeflossen sind:

- 1) M. Prasciolu, A. Haase, F. Scholze, H. N. Chapman und S. Bajt: „Extended asymmetric-cut multilayer X-ray gratings“. EN. In: *Optics Express* **23**.12 (Juni 2015), S. 15195–15204. DOI: 10.1364/OE.23.015195
- 2) V. Soltwisch, A. Haase, J. Wernecke, J. Probst, M. Schoengen, S. Burger, M. Krumrey und F. Scholze: „Correlated diffuse x-ray scattering from periodically nanostructured surfaces“. In: *Physical Review B* **94**.3 (Juli 2016), S. 035419. DOI: 10.1103/PhysRevB.94.035419

Ich habe an keiner anderen Hochschule oder Fakultät eine Promotionsabsicht eingereicht.

Berlin, den 31. März 2017

Anton Haase

